R-09-19

Groundwater flow modelling of the excavation and operational phases – Forsmark

Urban Svensson, Computer-aided Fluid Engineering AB

Sven Follin, SF GeoLogic AB

July 2010

Svensk Kärnbränslehantering AB
Swedish Nuclear Fuel
and Waste Management Co

Box 250, SE-101 24 Stockholm
Phone +46 8 459 84 00

ISSN 1402-3091
SKB R-09-19

ID 1248214

Updated 2013-08

Groundwater flow modelling of the excavation and operational phases – Forsmark

Urban Svensson, Computer-aided Fluid Engineering AB

Sven Follin, SF GeoLogic AB

July 2010

Keywords: Hydrogeology, Groundwater, Modelling, Excavation, Operation, Grouting, Forsmark, Safety assessment.

Update notice

The original report, dated July 2010, was found to contain both factual and editorial errors which have been corrected in this updated version. The corrected factual errors are presented below.

Updated 2011-10

Location	Original text	Corrected text
Appendix B, under equation B-2	If d/r≈1,	If d/r≈10,

Updated 2013-08

Location	Original text	Corrected text
Page 25, Table 2-3, column 4, row 1	(0.038, 2.55)	(0.038, 2.50)
Page 25, Table 2-3, column 4, row 2	(0.038, 2.75)	(0.038, 2.70)
Page 25, Table 2-3, column 4, row 5	(0.038, 2.42)	(0.038, 2.38)
Page 76, Table 5-2, column 6	Wrong Font	All second values italicized
Page 76, Table 5-2, column 7, 8 and 9	Wrong Font	All values italicized
Page 83		*New reference:* Follin et al. 2005

The updated tables show the correct input values used in the modelling presented in the original version of this report; i.e. all results are identical between the original and the up-dated versions of the report.

Abstract

As a part of the license application for a final repository for spent nuclear fuel at Forsmark, the Swedish Nuclear Fuel and Waste Management Company (SKB) has undertaken a series of groundwater flow modelling studies. These represent time periods with different climate conditions and the simulations carried out contribute to the overall evaluation of the repository design and long-term radiological safety. The modelling study reported here presents calculated inflow rates, drawdown of the groundwater table and upconing of deep saline water for different levels of grouting efficiency during the excavation and operational phases of a final repository at Forsmark. The inflow calculations are accompanied by a sensitivity study, which among other matters handles the impact of parameter heterogeneity, different deposition hole rejection criteria, and the SFR facility (the repository for short-lived radioactive waste located approximately 1 km to the north of the investigated candidate area for a final repository at Forsmark). The report also presents tentative modelling results for the duration of the saturation phase, which starts once the used parts of the repository are being backfilled.

Sammanfattning

I Svensk Kärnbränslehanterings (SKB) ansökan om ett slutförvar för använt kärnbränsle i Forsmark ingår olika grundvattenmodelleringsstudier. Studierna hanterar perioder med olika klimatförhållanden och beräkningsresultaten från simuleringarna bidrar till bedömningsunderlaget inom design och långsiktig säkerhet. Föreliggande rapport presenterar resultaten från en modellering av bygg- och driftskedena av ett slutförvar i Forsmark. Rapporten redovisar beräknade inflöden till olika anläggningsdelar, beräknad avsänkning och beräknad uppträngning av salthaltigt, djupt grundvatten. Beräkningarna har utförts för olika täthetsnivåer av injektering. Inflödesberäkningarna har kompletterats med en känslighetsstudie i syfte att studera inverkan av olika typer av osäkerheter och antaganden, t ex betydelsen av inhomogena hydrauliska egenskaper i spricksystemet, olika kriterier för diskriminering av kapselhål, samtidig drift av SFR (förvaret för kortlivat radioaktivt avfall, som ligger ca 1 km norr om det undersökta kandidatområdet för ett slutförvar i Forsmark). Rapporten redovisar även en preliminär beräkning av varaktigheten av mättnadsskedet som påbörjas i och med att deponeringstunnlarna fylls igen.

Contents

1 Introduction

1.1 Background

The Swedish Nuclear Fuel and Waste Management Company (SKB) has conducted site investigations at two different locations, the Forsmark and Laxemar-Simpevarp areas (Figure 1-1), with the objective of siting a final repository for spent nuclear fuel according to the KBS-3 concept. As a part of the application for a final repository for spent nuclear fuel at Forsmark, information from a series of groundwater flow modelling studies is evaluated to serve as a basis for an assessment of the repository design and long-term radiological safety premises. The present report is one of a series of three groundwater flow modelling studies, which together handle different periods of the entire lifetime of a final repository at Forsmark.

- Groundwater flow modelling of the excavation and operational phases – Forsmark (this report).
- Groundwater flow modelling of periods with temperate climate conditions – Forsmark /Joyce et al. 2010/.
- Groundwater flow modelling of periods with periglacial and glacial climate conditions – Forsmark /Vidstrand et al. 2010/.

A corresponding series of studies exists for the investigated area at Laxemar/Simpevarp. The results from the Laxemar/Simpevarp studies support the site-selection, which is reported as part of the application for Forsmark.

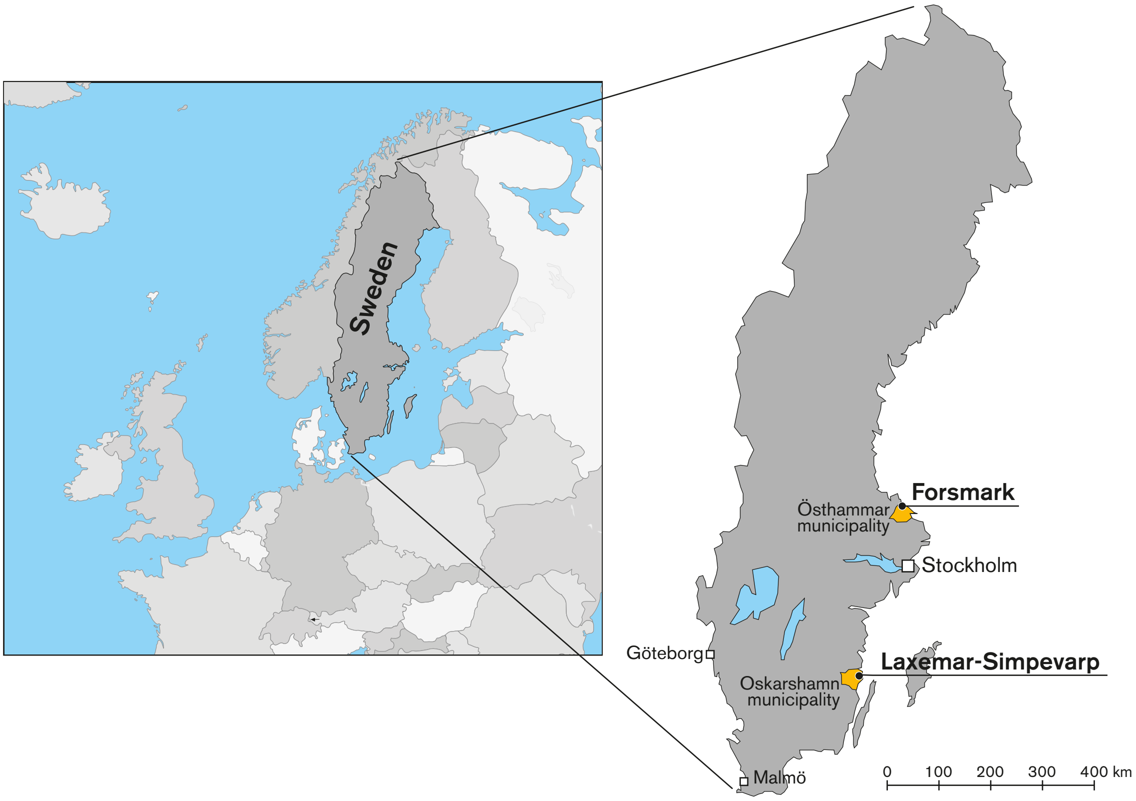

***Figure 1-1.** Map of Sweden showing the location of the Forsmark and Laxemar-Simpevarp sites, located in the municipalities of Östhammar and Oskarshamn, respectively. (Source: Figure 1-1 in /SKB 2008a/.)*

1.2 Scope and objectives

The main objective of the modelling work reported here is to inform about the hydrogeological effects caused by an open final repository for spent nuclear fuel at Forsmark. In particular, the work has studied:

- the magnitude and spatial distribution of the inflow to the open repository,
- the magnitude and spatial distribution of the drawdown of the groundwater table,
- the chemical composition and spatial distribution of the groundwater in proximity of the open repository,
- the role of grouting for the inflow, drawdown and upconing phenomena, and
- the saturation period after the open repository has been closed (backfilled).

The mathematical modelling reported here considers three operation stages, A–C, which are run in sequence, where the first stage, stage A, lasted for 15 years, stage B lasted for 15 years and stage C lasted for 20 years. Hence, the total operational time is 50 years. The role of grouting is looked at by modelling three levels of grouting efficiency, I–III. Finally, some sensitivity tests are run and, among other things, the effect of different criteria for the rejection of deposition holes is evaluated.

The modelling work used version 3.2 of the DarcyTools computational code. It is noted that the current documentation of DarcyTools concerns version 3.4 /Svensson et al. 2010/, but that the differences are insignificant for the applications reported here. Both versions allow the user to apply an unstructured computational grid. An unstructured grid is necessary in order to resolve the complex geometry of a final repository, which consists of a ramp, a few shafts, transport and main tunnels, and many deposition tunnels and close to seven thousands (6,916) deposition holes, see Figure 1-2. The studied repository is located at about –465 m elevation. The repository layout (D2) is adapted to the deterministically modelled deformation zones /SKB 2008b/.

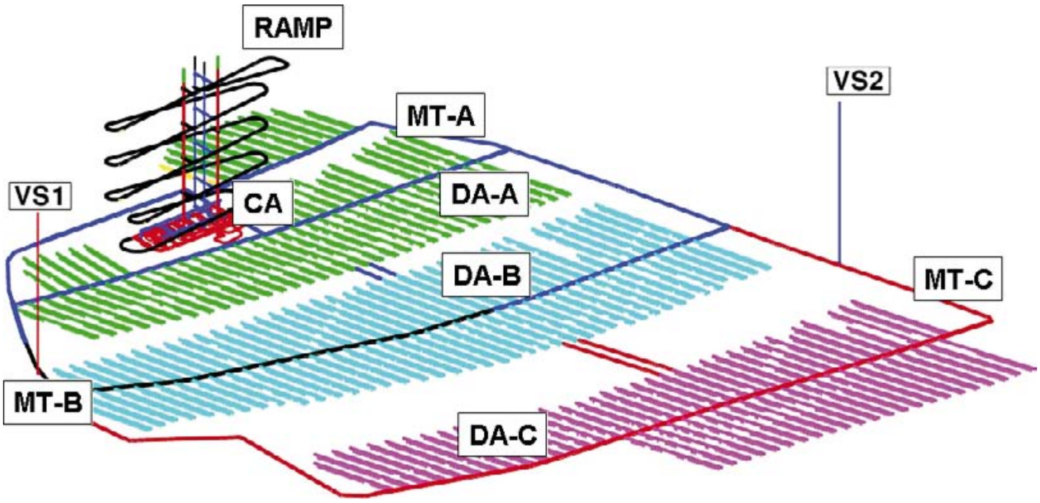

Figure 1-2. Definition of different parts of the studied repository layout (D2) at Forsmark. The mathematical modelling reported here considers three operation stages, A–C, and three possible grouting levels for each stage. The three stages are indicated by green, turquoise and pink colours. DA = deposition area, MT = transport and main tunnel, VS = ventilation shaft, CA = central area. The deposition tunnels are shown as branches to the main tunnels and the canister holes (almost invisible) are drilled from the bottom of the deposition tunnels.

1.3 Limitations

The transport of heat and the transport of radio nuclides from the repository to the ground level are not studied in the work reported here. In addition, all simulations are carried out at quasi steady-state flow conditions implying that storativity effects are considered unimportant for the physics involved during the excavation, operation and saturation periods of a final repository in fractured crystalline rock.

1.4 Setting

The Forsmark area is located in northern Uppland within the municipality of Östhammar, about 120 km north of Stockholm (Figure 1-1 and Figure 1-3). The candidate area for site investigation is located along the shoreline of Öregrundsgrepen. It extends from the Forsmark nuclear power plant and the access road to SFR in the north-west (SFR is an existing repository for short-lived radioactive waste) to Kallrigafjärden in the south-east (Figure 1-3). It is approximately 6 km long and 2 km wide. The north-western part of the candidate area is selected as the target area for the complete site investigation work /SKB 2005b/ (Figure 1-4).

The Forsmark area consists of crystalline bedrock that belongs to the Fennoscandian Shield, one of the ancient continental nuclei on the Earth. The bedrock at Forsmark in the south-western part of this shield formed between 1.89 and 1.85 billion years ago during the Svecokarelian orogeny /SKB 2005a/. It has been affected by both ductile and brittle deformation. The ductile deformation has resulted in large-scale, ductile high-strain belts and more discrete high-strain zones. Tectonic lenses, in which the bedrock is less affected by ductile deformation, are enclosed between the ductile high strain belts. The candidate area is located in the north-westernmost part of one of these tectonic lenses. This lens extends from north-west of the nuclear power plant south-eastwards to the area around Öregrund (Figure 1-5). The brittle deformation has given rise to reactivation of the ductile zones in the colder, brittle regime and the formation of new fracture zones with variable size.

The current ground surface in the Forsmark region forms a part of the sub-Cambrian peneplain in south-eastern Sweden. This peneplain represents a relatively flat topographic surface with a gentle dip towards the east that formed more than 540 million years ago. The candidate area at Forsmark is characterised locally by a low topographic relief and an elevation not far above sea level (Figure 1-6). The most elevated areas to the south-west of the candidate area are located at c 25 m above current sea level (datum RHB 70). The whole area is located below the highest coastline associated with the last glaciation, and large parts of the candidate area emerged from the Baltic Sea only during the last 2,000 years. Both the flat topography and the still ongoing shore level displacement of c 6 mm per year strongly influence the current landscape (Figure 1-6). Sea bottoms are continuously transformed into new terrestrial areas or freshwater lakes, and lakes and wetlands are successively covered by peat.

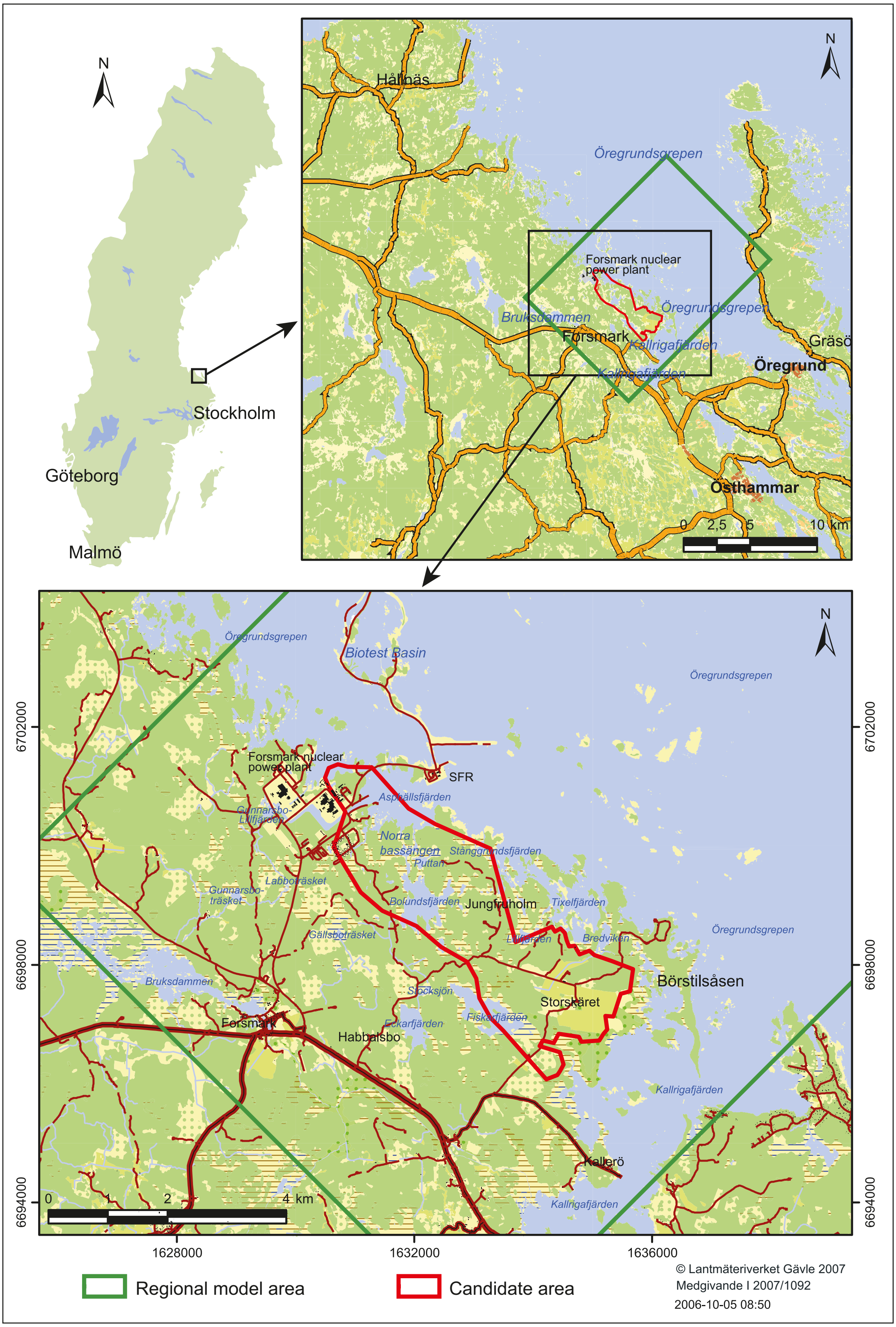

Figure 1-3. *The red polygon shows the size and location of the Forsmark candidate area for site investigation. The green rectangle indicates the size and location of the associated regional model area. (Source: Figure 1-3 in /SKB 2008a/.)*

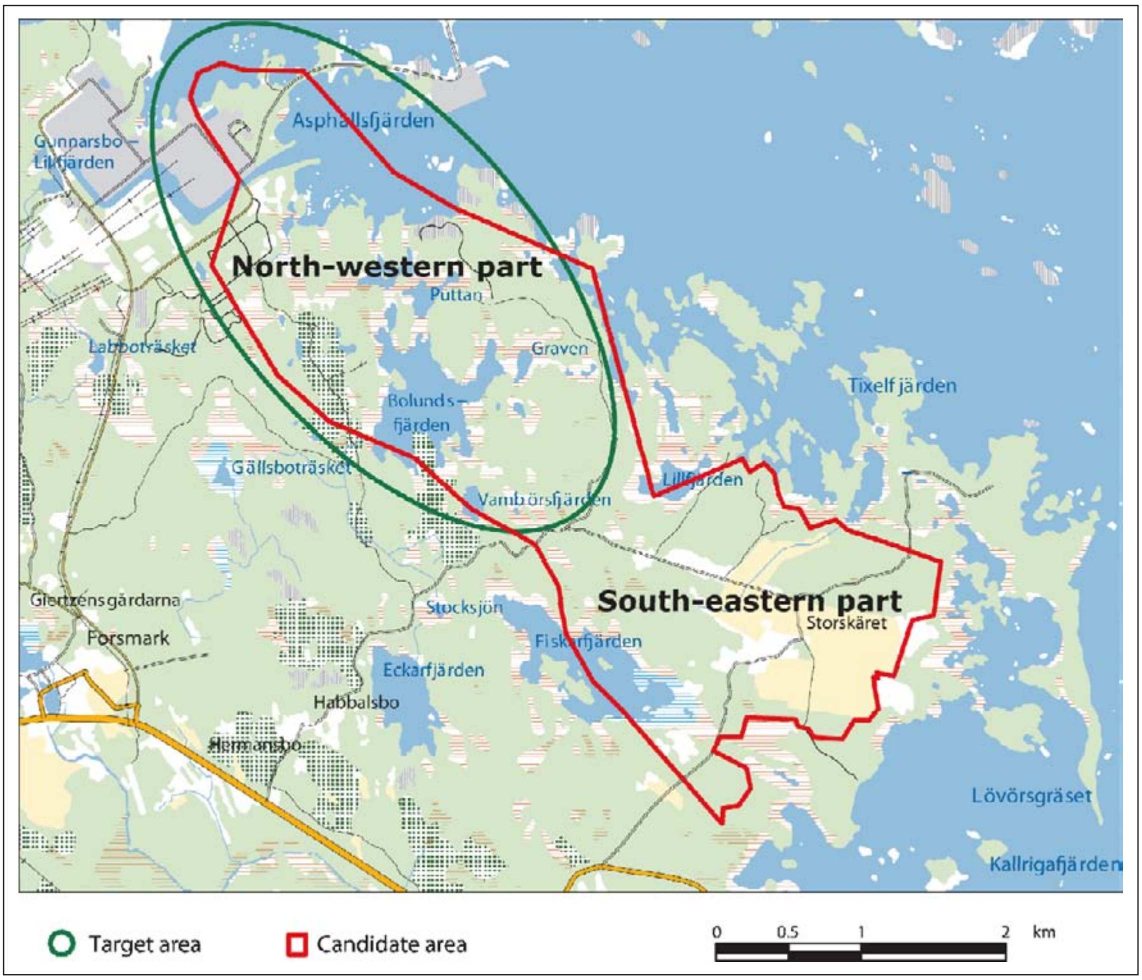

__Figure 1-4.__ The north-western part of the candidate area is selected as the target area for the complete site investigation work. (Modified after Figure 2-15 in /SKB 2005b/.)

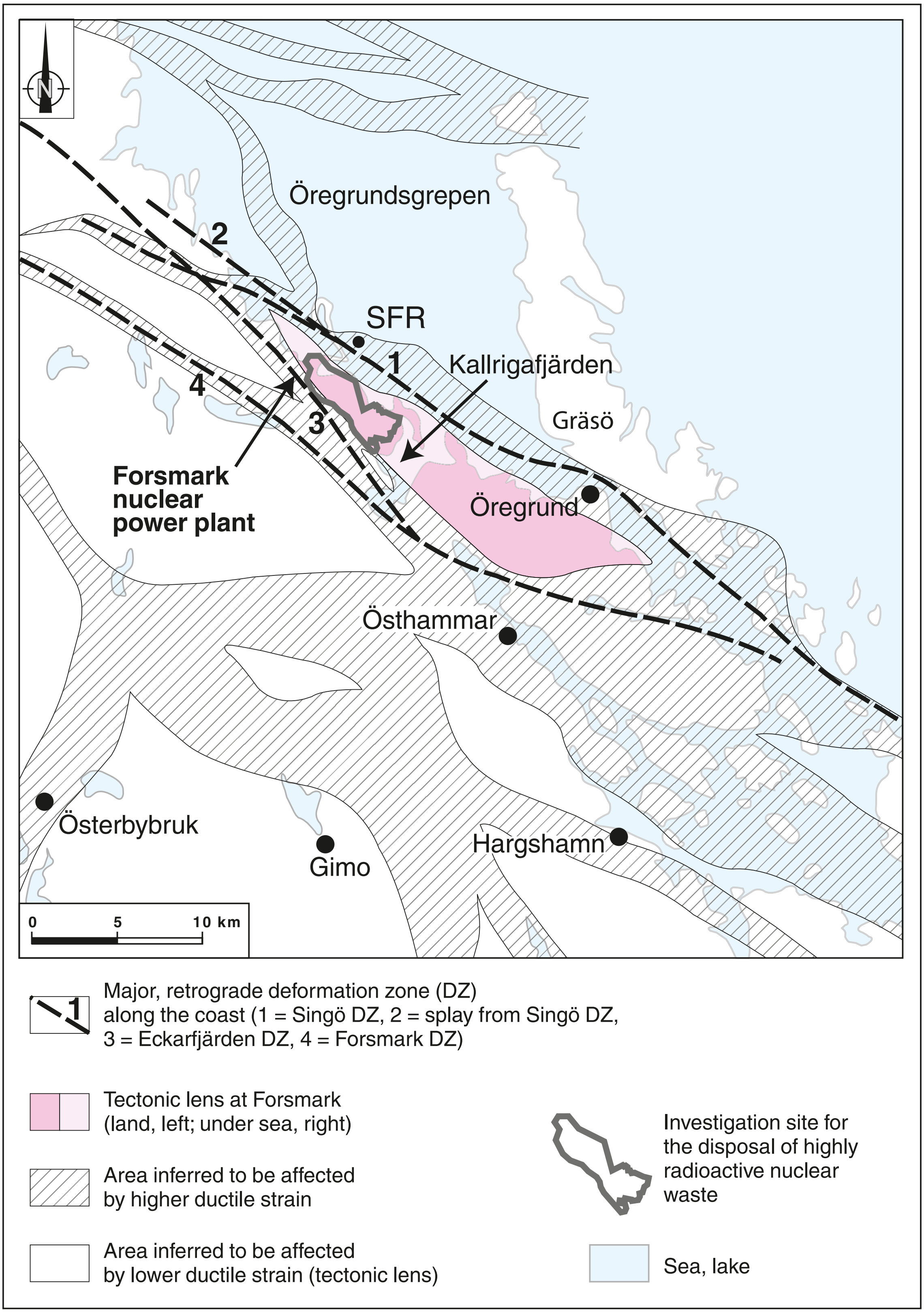

Figure 1-5. *Tectonic lens at Forsmark and areas affected by strong ductile deformation in the area close to Forsmark. (Source: Figure 4-1 in /Stephens et al. 2007/.)*

Figure 1-6. *Photos from Forsmark showing the flat topography and the low-gradient shoreline with recently isolated bays due to land uplift. (Source: Figure 1.7 in /Follin 2008/.)*

1.5 This report

/Selroos and Follin 2010/ present the data and hydraulic properties from the Site Descriptive Modelling (SDM) work as well as the methodology to be used by the three groundwater flow modelling studies that serve as a basis for an assessment of the design and long-term radiological safety of a final repository at Forsmark in the SR-Site project. The conditions that are specific to the flow modelling of the excavation and operational phases of a final repository at Forsmark are summarised in Chapter 4.

In order to better understand the modelling setup and the chosen implementations in DarcyTools, we briefly present in Chapter 2 the hydrogeological model of the Forsmark site, and in Chapter 3 the primary concepts and methodology of the DarcyTools computational code.

The conditions described in Chapter 4 refer to a flow model setup that is referred to as the base case in this report. The geometrical and hydraulic properties of the deformation zones and the fracture domains handled in the base case are identical to those of the hydrogeological base case treated in the groundwater flow modelling of the temperate period /Joyce et al. 2010/. Chapter 4 also presents the model variants handled as a means to address various uncertainties, e.g. parameter heterogeneity and simultaneous operation of two repositories, a final repository and SFR, the repository for short-lived radioactive waste located c 1 km to the north of the investigated candidate area. Chapter 5 presents the results of the flow simulations, and Chapter 6 contains a summary of the work carried out and the conclusions drawn.

The report contains six appendices A-F with the objective to describe and document some key assumptions of the implementations in DarcyTools, or for the sake of traceability, consistency and quality assurance.

- The position of the groundwater table is modelled with a free surface algorithm that can handle both natural conditions and the drawdown due to the inflow to an open repository. The algorithm is described in Appendix A.
- The impact of grouting on the calculated inflow rates, drawdown of the groundwater table and upconing of deep saline water is studied by altering the hydraulic conductivity of the computational grid cells in contact with the modelled repository. Appendix B describes how the grouting routine is applied.
- Appendix C is an excerpt of /Svensson 2010/. It briefly presents the hydration process and the approximate method used here to estimate the time scale of the saturation of the backfilling material.
- The setup and calibration of the sensitivity case dealing with a simultaneous operation of two repositories are explained in Appendix D.
- Appendix E presents a modelling approach where grid cells not intersected permeability by fractures are removed from the computational grid rather than giving them arbitrary low values as in the equivalent continuous porous medium approach.
- For the sake of traceability, consistency and overall quality assurance, Appendix F lists all files with input data, which are imported and used to parameterise the flow models reported here.

2 Hydrogeological model of the Forsmark site

2.1 Supporting documents

Three versions of a site descriptive model are completed for Forsmark prior to the final site descriptive model, SDM-Site /SKB 2008a/. Version 0 established the state of knowledge prior to the start of the site investigation programme. Version 1.1 was essentially a training exercise and is completed during 2004. Version 1.2 is a preliminary site description and concluded the initial site investigation work (ISI) in June 2005. The site descriptive modelling resulting in the final site description, SDM-Site, has involved three modelling stages, 2.1–2.3. The first modelling stage, referred to as stage 2.1, included an updated geological model for Forsmark and aimed to provide a feedback from the modelling working group to the site investigation team to enable completion of the site investigation work. The two background reports reported in stage 2.2 are key to repository engineering, one documenting the hydraulic properties of deformation zones and fracture domains /Follin et al. 2007a/ and one the development of a conceptual flow model and the results of numerical implementation and calibration of the flow model /Follin et al. 2007b/. Since the flow model with its calibrated hydraulic properties is also an essential input to the radiological safety assessment, the main findings of the flow modelling in stage 2.2 are revisited in stage 2.3. /Follin et al. 2008/ addressed the impact of parameter heterogeneity on the flow modelling results as well as the impact of the new field data acquired in data freeze 2.3 on the conceptual model development. Table 2-1 shows the cumulative number of boreholes providing hydraulic information about the bedrock at Forsmark. Table 2-1 also shows the reference numbers of the background reports on bedrock hydrogeology. This information is shown in relation to the three model versions and the three modelling stages carried out in preparation of the SDM-Site report /SKB 2008a/.

2.2 Systems approach in the SDM

Figure 2-1 illustrates schematically the division of the groundwater system into hydraulic domains as used by SKB in the SDM for both Forsmark and Laxemar /Simpevarp. The hydrogeological model consists of three hydraulic domains, HCD, HRD and HSD, where:

- HCD (Hydraulic Conductor Domain) represents deformation zones,
- HRD (Hydraulic Rock mass Domain) represents the less fractured bedrock in between the deformation zones, and
- HSD (Hydraulic Soil Domain) represents the regolith (Quaternary deposits).

Table 2-1. The cumulative number (and percentage) of cored boreholes (KFM) providing geometrical and hydraulic information about the bedrock at Forsmark at the end of each of the three model versions and three model stages carried out for SDM-Site. The underlined report numbers present correlation analyses of geometrical and hydraulic data of the flowing fractures detected with the Posiva Flow Log method. The report numbers typed in italics describe the hydraulic data gathered and the hydrogeological modelling undertaken. The report numbers typed in bold summarise the development of the hydrogeological modelling achieved at each stage. (Modified after Table 1-2 in /Follin 2008/.)

	Initial site investigation (ISI)			**Complete site investigation (CSI)**	
Desk top exercise	**Training exercise**	**Preliminary SDM**	**Feedback and strategy**	**Hydrogeological model**	**Model verification and uncertainty assessment**
Version 0	**Version 1.1**	**Version 1.2**	**Stage 2.1**	**Stage 2.2**	**Stage 2.3**
0 KFM (0%) Σ length: 0 km **R-02-32**	1 KFM (4%) Σ length: 1 km **R-04-15** P-04-77	5 KFM (21%) Σ length: 5 km **R-05-18** *R-05-32* *R-05-60* P-04-77	9 KFM (38%) Σ length: 7 km **R-06-38** *R-07-20* P-06-56	20 KFM (83%) Σ length: 15.9 km **R-07-49** *R-07-48* P-07-127	25 KFM (100%) Σ length: 19.4 km **R-08-95** *R-08-23* P-07-128

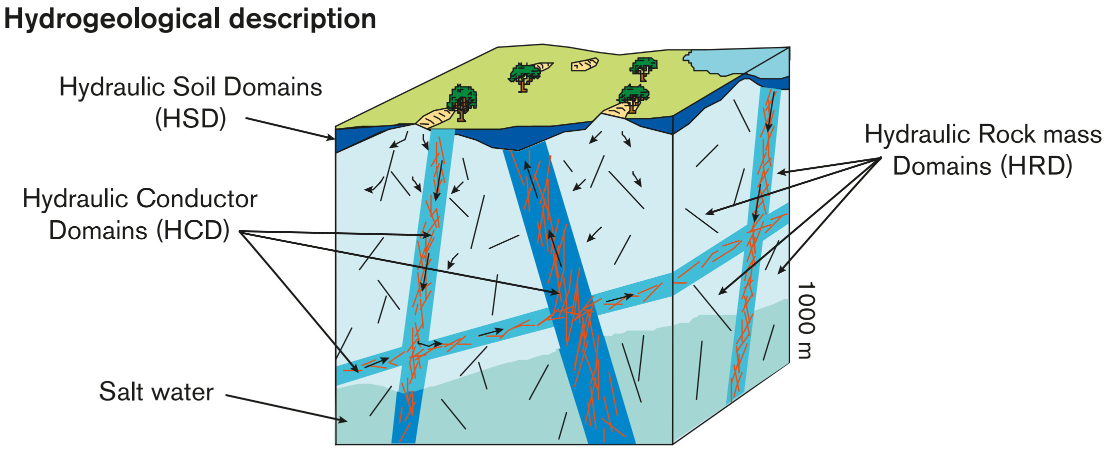

Figure 2-1. Cartoon showing the division of the crystalline bedrock and the regolith (Quaternary deposits) into three hydraulic domains, HCD, HRD and HSD. (Source: Figure 3-2 in /Rhén et al. 2003/.)

The division into hydraulic domains constituted the basis for the conceptual modelling, the planning of the site investigations and the groundwater flow modelling carried out in the SDM studies. Besides the three hydraulic domains, the systems approach also encompasses the following three model components:

- a dual-porosity model for the modelling of salt transport in the fracture system (advection and dispersion) and in the rock matrix (diffusion),
- initial conditions for groundwater flow and hydrochemistry, and
- boundary conditions for groundwater flow and hydrochemistry.

2.3 Summary of the bedrock hydrogeological model

2.3.1 General

The bedrock in the Forsmark area has been thoroughly characterised with both single-hole and cross-hole (interference) tests. Constant-head injection tests and difference flow logging pumping tests have been used in parallel to characterise the fracture properties close to the boreholes, and interference tests have been used for larger-scale studies. The overall experience from these investigations is that spatial variability in the structural geology significantly affects the bedrock hydrogeology and associated hydraulic properties at all depths. There is a substantial depth trend in deformation zone transmissivity and in the conductive fracture frequency in the bedrock between the deformation zones; the uppermost part of the bedrock is found to be significantly more conductive than the deeper parts. In conclusion, the strong contrasts in the structural-hydraulic properties with depth encountered inside the target volume suggest a hydraulic phenomenon that causes shallow penetration depths of the near-surface groundwater flow system. This probably contributes to the observed slow transient evolution of fracture water and porewater hydrochemistry at repository depth, although the slow evolution is mainly due to the low permeability at these depths.

The left picture in Figure 2-2 illustrates the high water yield of boreholes drilled in the uppermost part of the bedrock close to ground surface. The right picture shows a man carrying two unbroken 3 m long drill cores acquired from repository depth. Hundreds of such unbroken drill cores are obtained within the target volume, information that conforms to the low water yields encountered at repository depth. The spatial extent of these two observations, a permeable "shallow bedrock aquifer" on top of a sparsely fractured bedrock of low permeability is hypothesised in modelling stage 2.2. The hypothesis was not falsified by data from the new boreholes, single-hole hydraulic tests and interference tests conducted in modelling stage 2.3. The frequency and the transmissivity of conductive fractures are plotted versus depth in Figure 2-12.

Figure 2-2. *Two key features of the bedrock in the target area at Forsmark. Left: High water yields are often observed in the uppermost c 150 m of the bedrock. Right: The large number of unbroken drill cores gathered at depth support the observation of few flowing test sections in the deeper bedrock. (Source: Figure 10-1 in /Follin 2008/.)*

2.3.2 Hydraulic characteristics of hydraulic conductor domains (HCD)

The hydrogeological model suggested for the deterministically modelled deformation zones (Figure 2-3) has four main characteristics.

- The division of the deformation zones into major sets and subsets is useful from a hydrogeological point of view. Most of these structural entities are steeply dipping and strike WNW-NW, NNW and NNE-NE-ENE; one is gently dipping (G).
- All deformation zones, regardless of orientation (strike and dip), display a substantial decrease in transmissivity with depth. The data suggest a contrast of c 20,000 times in the uppermost one kilometre of the bedrock, i.e. more than four orders of magnitude. Hydraulic data below this depth are lacking (Figure 2-4).
- The lateral heterogeneity in transmissivity is also substantial (a few orders of magnitude) but more irregular.
- The highest transmissivities within the candidate area, regardless of depth, have been observed among the gently dipping deformation zones. The steeply dipping deformation zones that strike WNW and NW have, relatively speaking, higher mean transmissivities than steeply dipping deformation zones in other directions.

An exponential model for the depth dependency of the in-plane deformation zone transmissivity was simulated in /Follin et al. 2007b/ based on the data shown in Figure 2-4. The depth trend model may be written as:

$$T(z) = T(0)10^{z/k} \qquad (2\text{-}1)$$

where T(z) is the deformation zone transmissivity, z is the elevation relative the sea level of year 1970 (RHB 70), $T(0)$ is the expected value of the transmissivity of the deformation zone at zero elevation and k is the depth interval that gives an order of magnitude decrease of the transmissivity. The value of $T(0)$ can be estimated by inserting a measured value [z', $T(z')$] in Equation (2-1), i.e.:

$$T(0) = T(z')10^{-z'/k} \qquad (2\text{-}2)$$

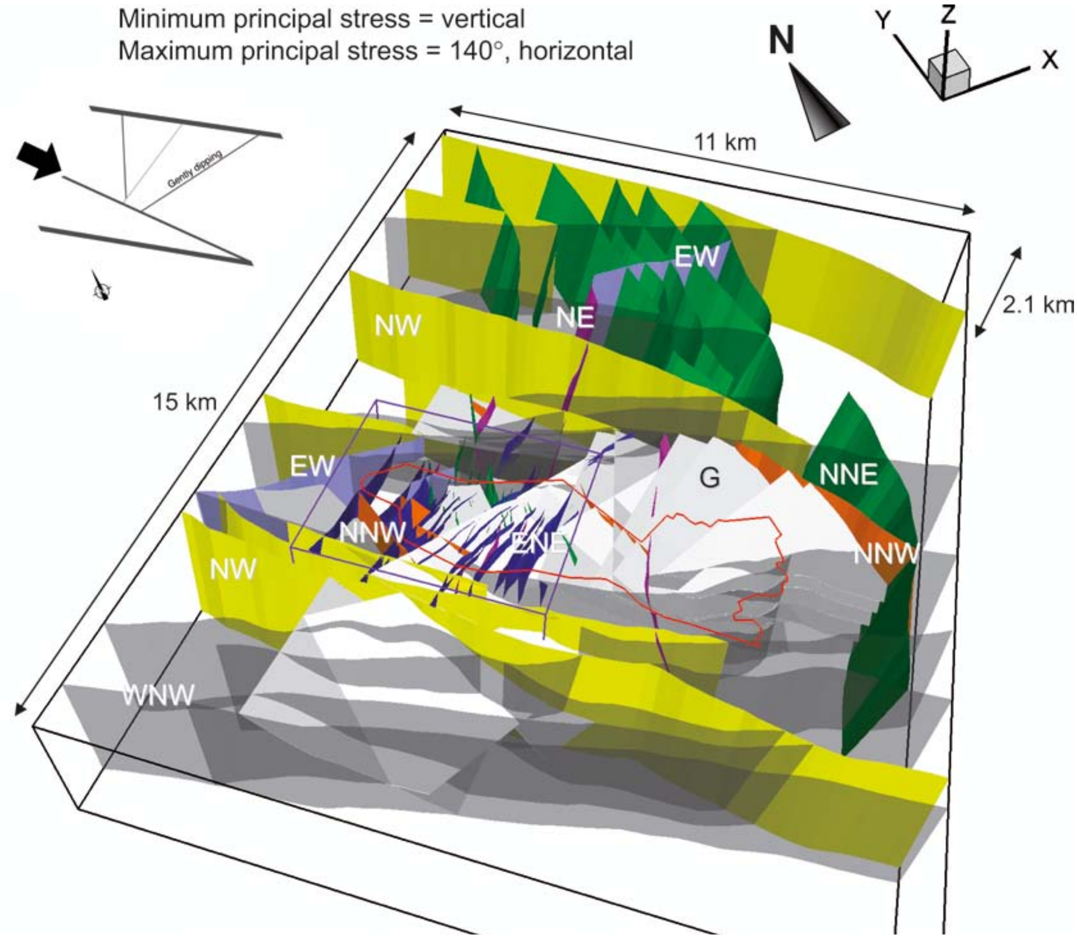

Figure 2-3. 3-D visualisation of the regional model domain and the 131 deformation zones modelled deterministically for Forsmark stage 2.2. The steeply dipping deformation zones (107) are shaded in different colours and labelled with their principal direction of strike. The gently dipping zones (24) are shaded in pale grey and denoted by a G. The border of the candidate area is shown in red and regional and local model domains in black and purple, respectively. The inset in the upper left corner of the figure shows the direction of the main principal stress. (Source: Figure 3-4 in /Follin 2008/.)

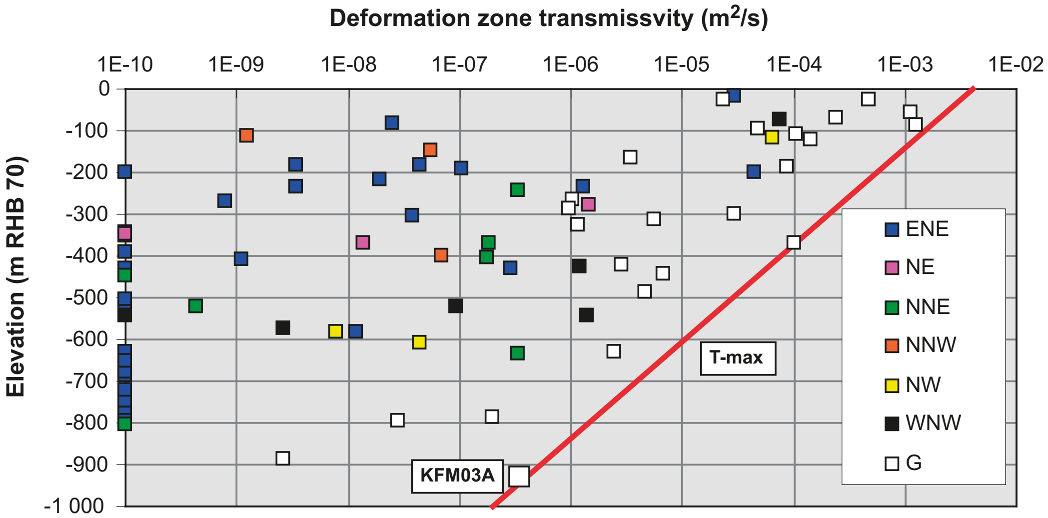

***Figure 2-4.** Transmissivity data versus depth for the deterministically modelled deformation zones. The transmissivities are coloured with reference to the orientations of the deformation zones, where G means gently dipping. The deformation zones with no measurable flow are assigned an arbitrary low transmissivity value of $1 \cdot 10^{-10}$ m^2/s in order to make them visible on the log scale. (Source: Figure 5-1 in /Follin 2008/.)*

In the case of several measurements at different locations in the same zone, the geometric mean of the calculated values of $T(0)$ is used as an effective value, $T_{eff}(0)$ in Equation (2-1). With this approach, the effect of conditioning to a measurement is to extrapolate the conditioned value over the entire extent of the deformation zone laterally, but not more than 100 m vertically, see Figure 2-5. Lateral heterogeneity was simulated in /Follin et al. 2008/ by adding a log-normal random deviate to the exponent in Equation (2-1), i.e.:

$$T(z) = T(0)10^{z/k+N(0,\sigma_{\log(T)})} \qquad (2\text{-}3)$$

where $\sigma_{\log(T)} = 0.632$. The applied value of $\sigma_{\log(T)}$ implies that 95% of the lateral spread in T is assumed to be within 2.5 orders of magnitude. Furthermore, the transmissivity model assumed a nugget covariance model for the lateral spatial variability, which was conditioned on measured transmissivity data. Since the heterogeneity away from the measurement boreholes is undetermined, this required a stochastic approach using several model realisations, see Figure 2-5 for an example. The calibrated deterministic base model realisation derived in /Follin et al. 2007b/ corresponds to case where $\sigma_{\log(T)}$ was set to zero.

The kinematic porosity of the deformation zones is not investigated. In the groundwater flow modelling, values of the kinematic porosity are calculated from the ratio between the transport aperture and the geological thickness. The transport apertures are calculated from the transmissivities of the deformation zones (see Equation (2-1) in /Follin 2008/ and Equation (3-17) in section 3.2.2) and the values of the geologic thicknesses are provided by /Stephens et al. 2007/.

2.3.3 Hydraulic characteristics of the hydraulic rock domains (HRD)

The hydrogeological model of the fracture domains, i.e. the fractured bedrock between the deterministically modelled deformation zones (Figure 2-6, Figure 2-7, and Figure 2-8) has four main characteristics:

- The division of the bedrock between the deterministically modelled deformation zones in the candidate area into six fracture domains, FFM01-06, and five fracture sets, NS, NE, NW, EW and HZ, is useful from a hydrogeological point of view.
- The conductive fracture frequency shows very strong variations with depth, and a discrete network model for conductive fractures within the target volume is adopted that is split into three layers; above 200 m depth, between 200 and 400 m depth, and below 400 m depth.
- The hydraulic character of the fracture domains is dominated by the gently dipping HZ fracture set, and with only a small contribution from the steeply dipping NS and possibly NE fracture sets. However, the depth trend in fracture transmissivity for the fracture domains is not as conclusive as for the deformation zones.
- The sparse number of steeply dipping flowing features at depth within the target volume suggests that fractures associated with the gently dipping HZ fracture set may be fairly long (large) in order to form a sufficiently connected network.

For the bedrock outside the candidate area, due to lack of data the discrete fracture network (DFN) approach associated with the fracture domain concept is replaced by a continuous porous medium (CPM) approach in the hydrogeological modelling for the SDM. Approximate values for this rock are taken from hydraulic single-hole tests in deep boreholes at Finnsjön /Andersson et al. 1991/ using the results given for the geometric mean of 3 m double-packer injection tests in the bedrock between deformation zones, see Table 2-2. A depth dependency is suggested by the data, which was simplified in the SDM to a step-wise model consistent with the depth zonations used in FFM01 in the SDM work. Table 2-3 shows the parameter setup of the hydrogeological DFN model used for the target volume in the groundwater flow modelling. r_0 and k_r are the location parameter and the shape parameter, respectively, of the assumed power-law size-intensity distribution.

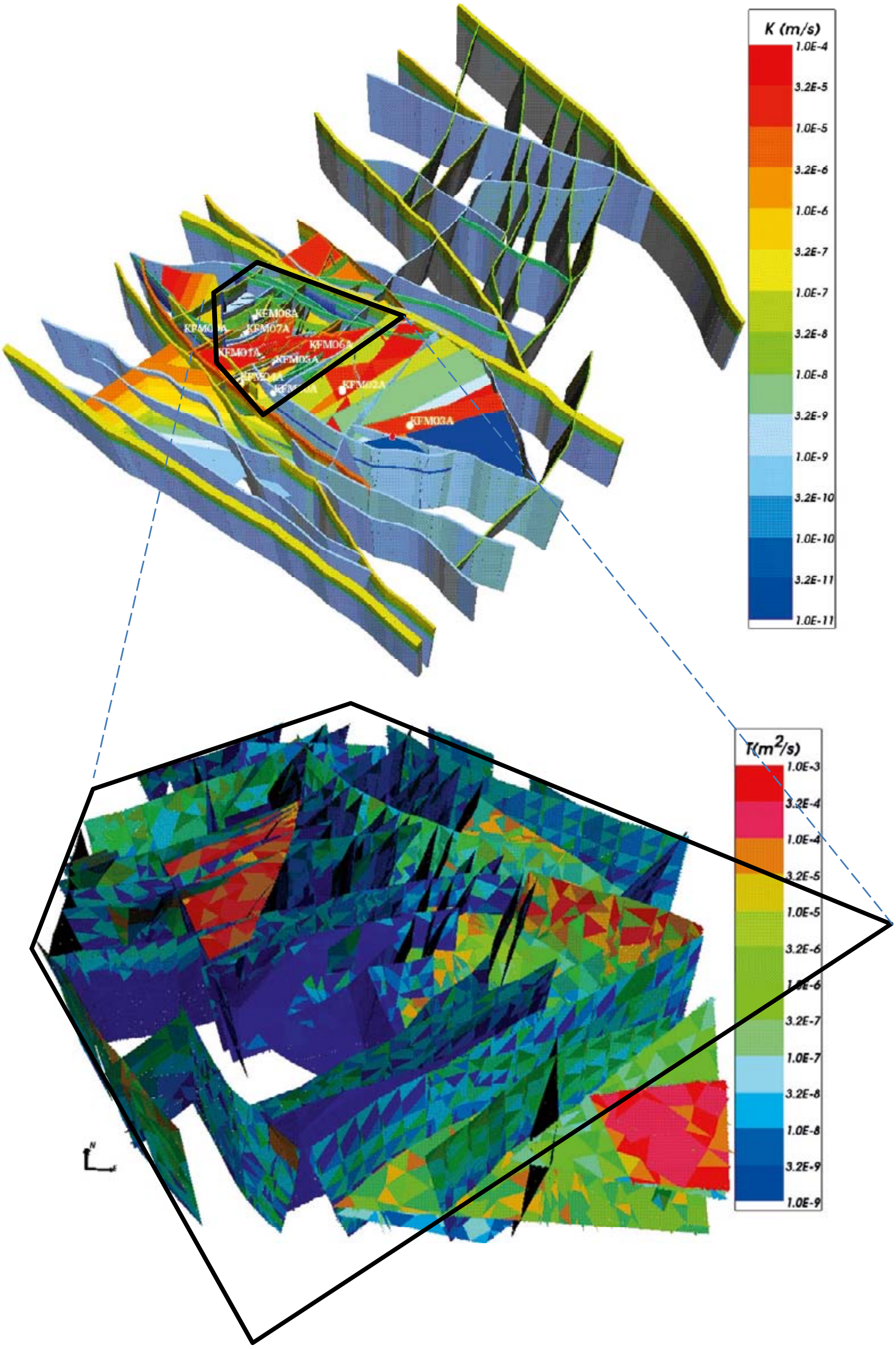

Figure 2-5. *Top: The resulting homogeneous (deterministic) property model of the HCDs using Equation (3-1). Here, the regional scale deformation zones are coloured to indicate the hydraulic conductivity within the zones and drawn as volumes to show their assigned hydraulic width. Bottom: Example visualisation of a stochastic realisation of the deformation zones that occur inside the local model domain using Equation (2-3) to define heterogeneous hydraulic properties. (Modified after Figure 6-1 and Figure 6-2 in /Follin 2008/.)*

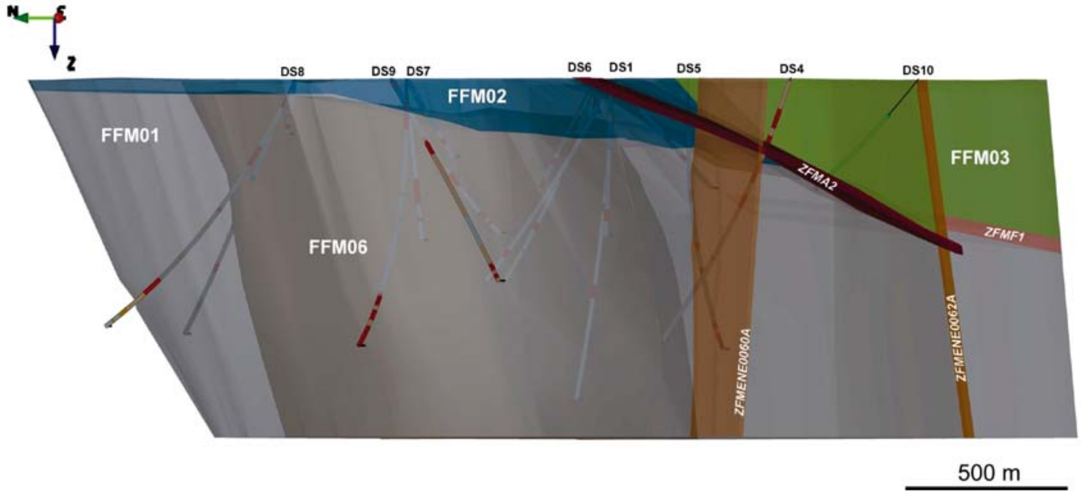

Figure 2-6. *Three-dimensional view of the fracture domain model, viewed towards ENE. Fracture domains FFM01, FFM02, FFM03 and FFM06 are coloured grey, dark grey, blue and green, respectively. The gently dipping and sub-horizontal zones A2 and F1 as well as the steeply dipping deformation zones ENE0060A and ENE0062A are also shown. (Source: Figure 3-10 in /Follin 2008/.)*

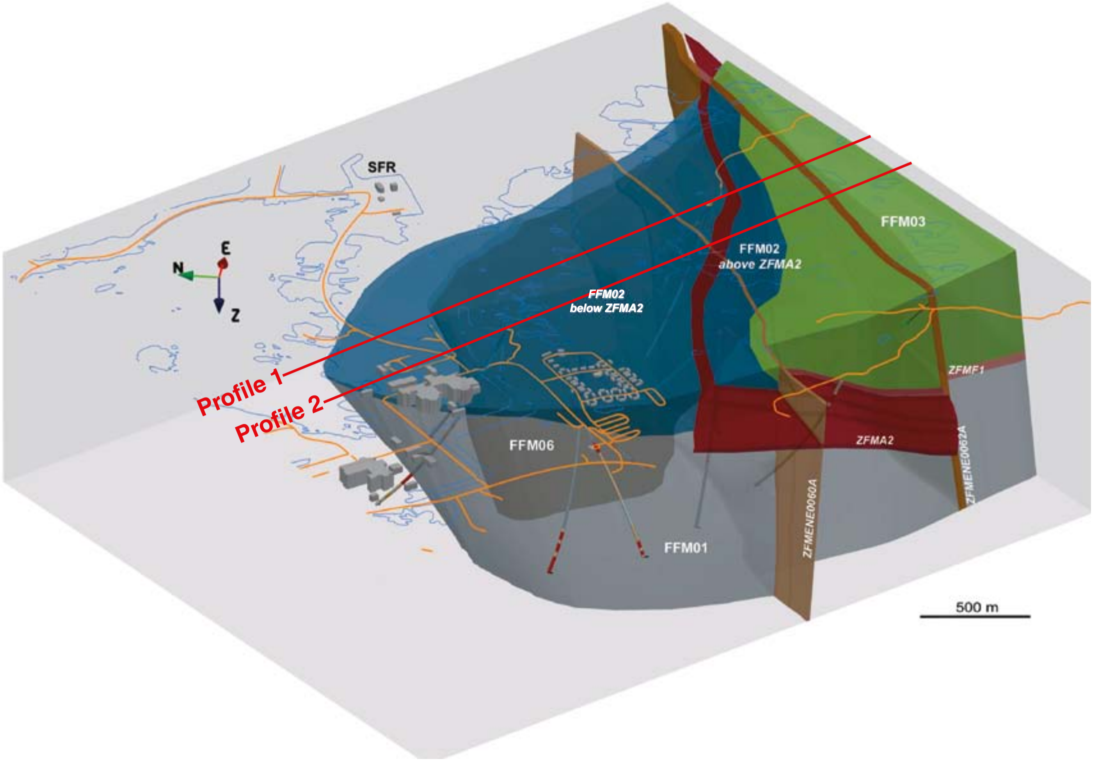

Figure 2-7. *Three-dimensional view towards ENE showing the relationship between deformation zone A2 (red) and fracture domain FFM02 (blue). Profile 1 and 2 are shown as cross-sections in Figure 2-8. (Source: Figure 3-11 in /Follin 2008/.)*

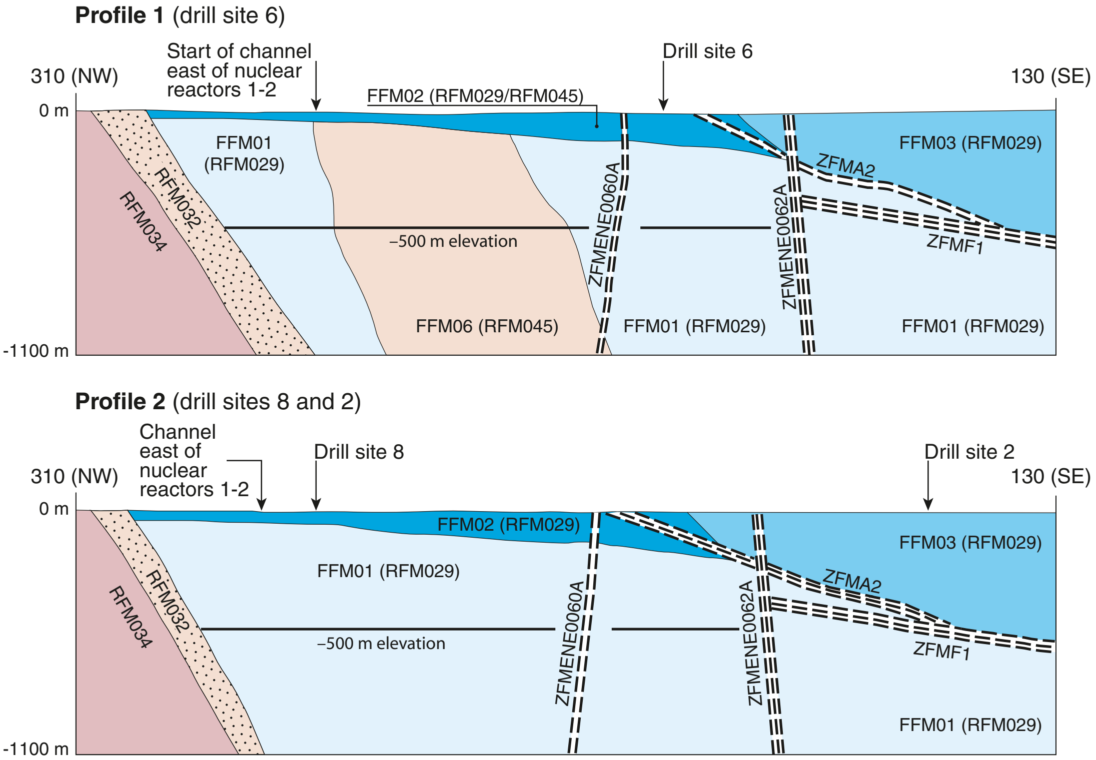

Figure 2-8. *Simplified profiles in a NW-SE direction that pass through the target volume. The locations of the profiles are shown in Figure 2-7. The key fracture domains, FFM01,-02 and -06, for a final repository at Forsmark occur in the footwall of zones A2 (gently dipping) and F1 (sub-horizontal). The major steeply dipping zones ENE0060A and ENE0062A are also included in the profiles. (Source: Figure 5-4 in /Olofsson et al. 2007/.)*

Table 2-2. Homogeneous and isotropic hydraulic properties used for the HRDs outside the candidate area. (Source: Table 3-6 in /Follin et al. 2007a/.)

Elevation (m RHB 70)	Hydraulic conductivity (m/s)	Kinematic porosity (-)
> –200	$1{\cdot}10^{-7}$	$1{\cdot}10^{-5}$
–200 to –400	$1{\cdot}10^{-8}$	$1{\cdot}10^{-5}$
< –400	$3{\cdot}10^{-9}$	$1{\cdot}10^{-5}$

2.3.4 Hydrogeological characteristics of the target volume

The cross-section cartoon in Figure 2-9 summarises the key components of the conceptual model of the bedrock hydrogeology in the target volume at Forsmark.

- The flow at repository depth in fracture domains FFM01 and FFM06 is probably channelised in the sparse network of connected fractures, **D**, which is dominated by two fracture sets, HZ and NE. The HZ fracture set is interpreted to be longer and probably more transmissive than the NE set.
- **D** connects to **A** and **C**, where **A** represents the steeply dipping NNE-ENE deformation zones, which are abundant but hydraulically heterogeneous, and **C** represents the intensely fractured fracture domain FFM02, which lies on top of **D**.
- The groundwater flow in **C** is dominated by the HZ fracture set, which occurs with a high frequency. More importantly, **C** is intersected by several extensive, horizontal fractures/sheet joints, **B** (Figure 2-10), which can be very transmissive (Figure 2-2).
- **B** and **C** and the outcropping parts of **A** probably form a shallow network of flowing fractures. The network is interpreted to be highly anisotropic, structurally and hydraulically. Together with **D**, which is close to the percolation threshold, the network creates a hydrogeological situation that is referred to as a shallow bedrock aquifer on top of a thicker bedrock segment with aquitard-type properties (Figure 2-11).

Figure 2-12 summarises the findings of the investigations with PFL-f method[1] in fracture domains FFM01-03 and -06. As an example, the hydrogeological DFN parameters deduced for FFM01 and FFM06 are tabulated in Table 2-3. The semi-correlated transmissivity-fracture size model referenced in the table may be written as:

$$\log(T) = \log(a\ r^{b}) + \sigma_{\log(T)}\ N[0,1] \qquad (2\text{-}4)$$

where T is the fracture transmissivity, r is the fracture radius, a and b are constants and $N[0,1]$ denotes a normally distributed random deviate with a mean equal to zero and a standard deviation of 1. In Table 2-3, r_0 and k_r are the location parameter and the shape parameter, respectively, of the assumed power-law size-intensity distribution. The kinematic porosity of individual fractures is not investigated during the site investigations. In the groundwater flow modelling conducted for the SDM-Site, values of the grid kinematic porosity of an equivalent continuous porous medium (ECPM) model are calculated from the transport aperture. The transport apertures, in turn, are calculated from the fracture transmissivities (see Equation (2-1) in /Follin 2008/ and Equation (3-17) in section 3.2.2).

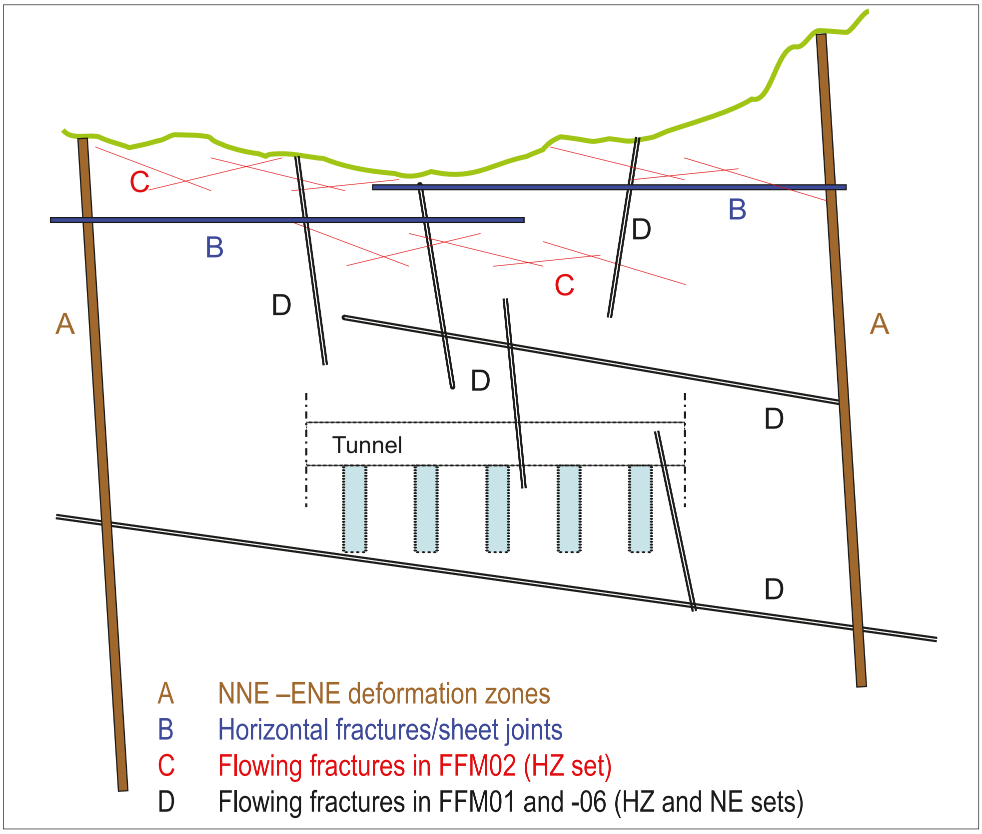

Figure 2-9. *A 2-D cartoon looking NE that summarises the hydrogeological conceptual model of the bedrock within the target volume at Forsmark. (Source: Figure 10-3 in /Follin 2008/.)*

---

[1] The PFL tool is a logging device developed by Posiva Oy to detect continuously flowing fractures in sparsely fractured crystalline rock. The physical limitations of the PFL tool and the principles for its operation are explained in detail in SKB's P-report series, e.g. /Rouhiainen and Sokolnicki 2005/, The PFL-f method implies a particular measurement procedure, where the specific capacity is determined fracture-wise with a spatial resolution of 0.1 m.

Figure 2-10. *Picture from the construction of the 13 m deep and more than one kilometre long canal between the Baltic Sea and the nuclear power reactors in Forsmark. Horizontal fractures/sheet joints are encountered along the entire excavation. The sheet joints follow the undulations of the bedrock surface implying that many of them do not outcrop, but stay below the bedrock surface as this dips under the Baltic Sea. There are several "horizons" of extensive sheet joints on top of each other as determined by the hydraulic interference tests. (Source: Figure 5-14 in /Follin 2008/.)*

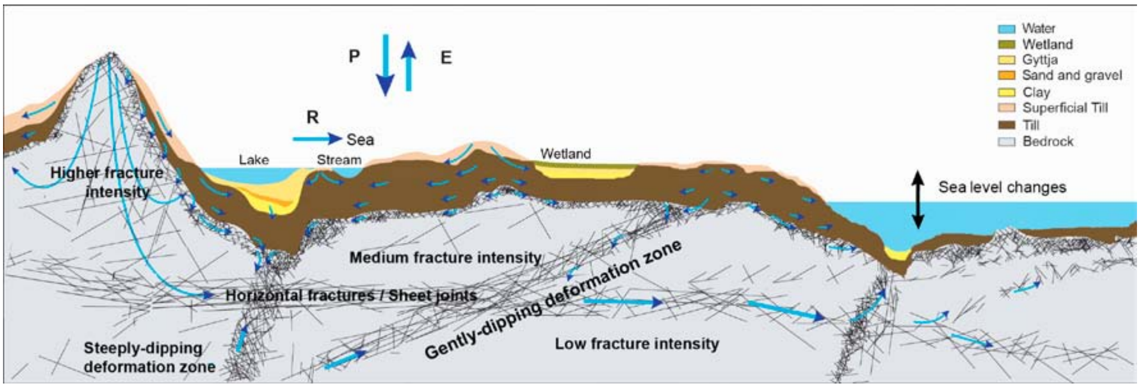

Figure 2-11. *Cross-section cartoon visualising the notion of a shallow bedrock aquifer and its impact on the groundwater flow system in the uppermost part of the bedrock within the target area. The shallow bedrock aquifer is hydraulically heterogeneous but at many places it is limiting the penetration of the recharge from above. The shallow bedrock aquifer is also conceived to constitute an important discharge horizon for the groundwater flow in outcropping deformation zones. P = precipitation, E = evapotranspiration, R = runoff. (Source: Figure 5-16 in /Follin 2008/.)*

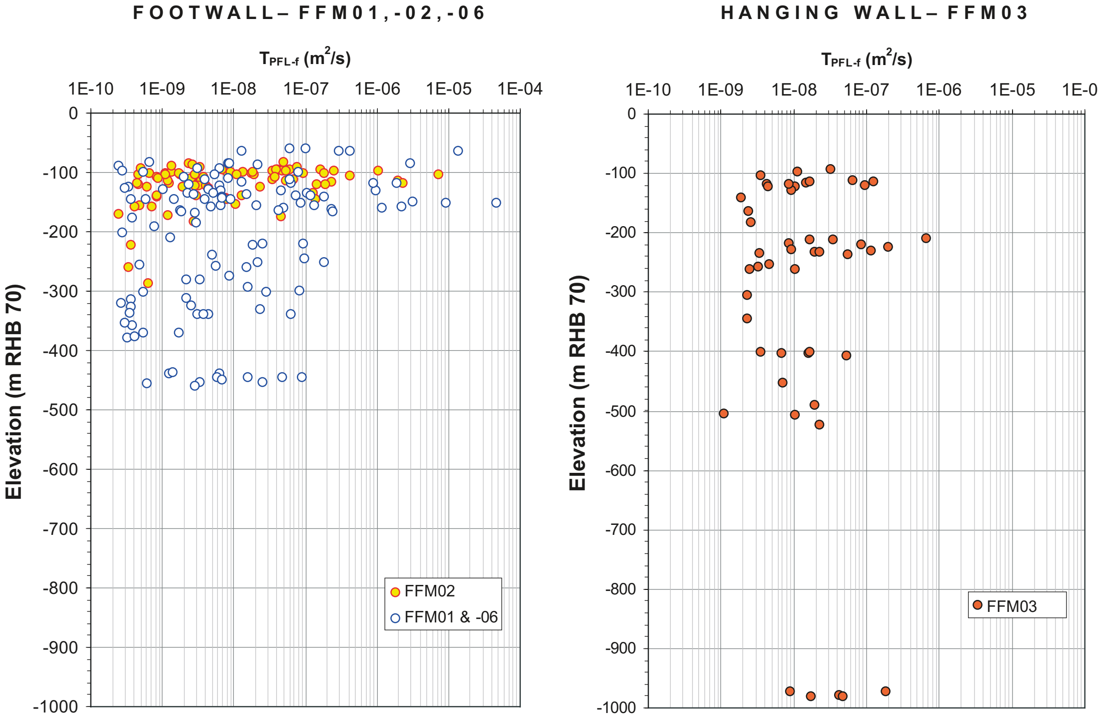

KFM01A, -01D, -02A (B½), -04A (B½),
-05A (< –100m), -06A, -07A, -08A, -08C, -08D

KFM02A (T½), -03A, -05A(> –100m), -10A

Figure 2-12. *Inferred transmissivities of connected open fractures detected with the PFL-f method in fracture domains FFM01–02 and -06 (left) and in FFM03 (right). In the legend, "footwall" and "hanging wall" refer to the gently dipping deformation zone ZFMA2. (Source: Figure 5-12 in /Follin 2008/.)*

Table 2-3. Hydrogeological DFN parameters for the semi-correlated transmissivity model of FFM01 and FFM06 with depth dependency: above –200 m, –200 m to –400 m and below –400 m RHB 70. (Source: Appendix C in /Follin 2008/.)

Fracture domain (m RHB 70)	**Fracture set name**	**Orientation set pole: (trend, plunge), conc.**	**Size model, power-law (r_0, k_r)** (m, –)	**Intensity ($P_{32,open}$) valid size interval: (r_0, 564 m)** (m²/m³)	**Transmissivity model constants Eq. (2-4)**
FFM01 & –06 > –200	NS	(292, 1) 17.8	(0.038, 2.50)	0.073	$(a,b,\sigma) = (6.3 \cdot 10^{-9}, 1.3, 1.0)$
	NE	(326, 2) 14.3	(0.038, 2.70)	0.319	
	NW	(60, 6) 12.9	(0.038, 3.10)	0.107	
	EW	(15, 2) 14.0	(0.038, 3.10)	0.088	
	HZ	(5, 86) 15.2	(0.038, 2.38)	0.543	
FFM01 & –06 –200 to –400	NS	As above	As above	0.142	$(a,b,\sigma) = (1.3 \cdot 10^{-9}, 0.5, 1.0)$
	NE	As above	As above	0.345	
	NW	As above	As above	0.133	
	EW	As above	As above	0.081	
	HZ	As above	As above	0.316	
FFM01 & –06 < –400	NS	As above	As above	0.094	$(a,b,\sigma) = (5.3 \cdot 10^{-11}, 0.5, 1.0)$
	NE	As above	As above	0.163	
	NW	As above	As above	0.098	
	EW	As above	As above	0.039	
	HZ	As above	As above	0.141	

2.4 Summary of the regolith hydrogeological model (HSD)

All known regolith at Forsmark is deposited during the Quaternary period, and thus is generally referred to as Quaternary deposits. In addition, most of the Quaternary deposits at Forsmark are probably deposited during or after the latest deglaciation (Weichsel). Figure 2-13 shows the conceptual model of the stratigraphy. The model consists of nine layers (L1–L3, Z1–Z6). Not all layers exist everywhere, and the thickness of individual layers varies significantly. The overall thickness of the Quaternary deposits varies from less than a decimetre to a maximum of 42 m /Hedenström et al. 2008/. The definition of the nine layers is shown in Table 2-4.

The conceptual model is developed for the area shown in Figure 2-14, which covers most of the site descriptive regional model area. The model is truncated in the south slightly more than in the regional-scale hydrogeological model. The interpreted thicknesses of the Quaternary deposits are also shown in Figure 2-14. The compilation of different kinds of data obtained from several types of investigations has produced this model. The accuracy of the map varies, therefore, and the most detailed information was obtained from the central part of the model area and in the near-shore coastal area. The profile in Figure 2-14 shows the stratification of the Quaternary deposits s beneath Lake Bolundsfjärden as an example.

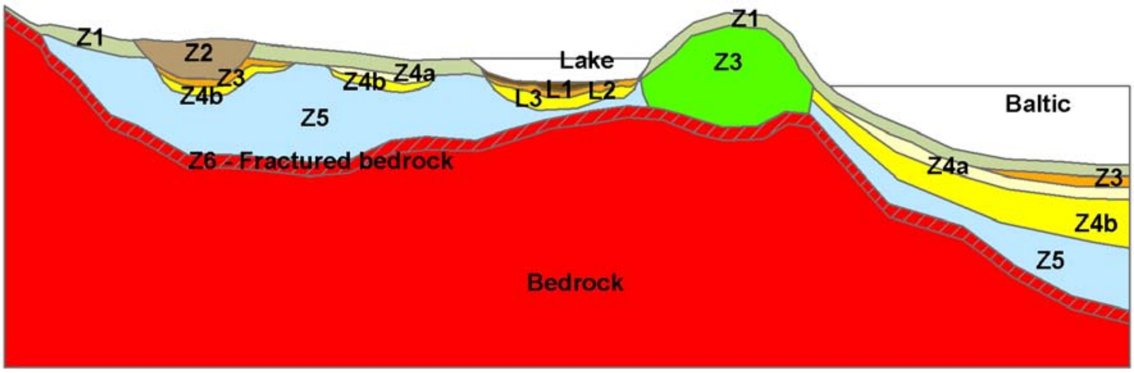

Figure 2-13. *Conceptual model for the layering of Quaternary deposits at Forsmark. The different layers are explained in Table 3-4¶ (Source: Figure 3-1 in /Hedenström et al. 2008/.)*

Table 2-4. Names and definitions of Quaternary deposits (Modified after Table 2-4 in /Hedenström et al. 2008/.)

Layer	Description and comments
L1	Layer consisting of different kinds of gyttja/mud/clay or peat. Interpolated from input data, thickness will therefore vary.
L2	Layer consisting of sand and gravel. Interpolated from input data, thickness will therefore vary.
L3	Layer consisting of different clays (glacial and postglacial). Interpolated from input data, thickness will therefore vary.
Z1	Surface affected layer present all over the model, except where peat is found and under lakes with lenses. Thickness is 0.10 m on bedrock outcrops, 0.60 m elsewhere. If total regolith thickness is less than 0.60 m, Z1 will have the same thickness as the total, i.e. in those areas only Z1 will exist.
Z2	Surface layer consisting of peat. Zero thickness in the sea. Always overlies by Z3.
Z3	Middle layer of sediments. Only found where surface layers are other than till, clay or peat.
Z4a	Middle layer consisting of postglacial clay. Always overlies by Z4b.
Z4b	Middle layer of glacial clay.
Z5	Corresponds to a layer of till.. The bottom of layer Z5 corresponds to the bedrock surface.
Z6	Upper part of the bedrock. Fractured rock. Constant thickness of 0.5 m. Calculated as an offset from Z5.

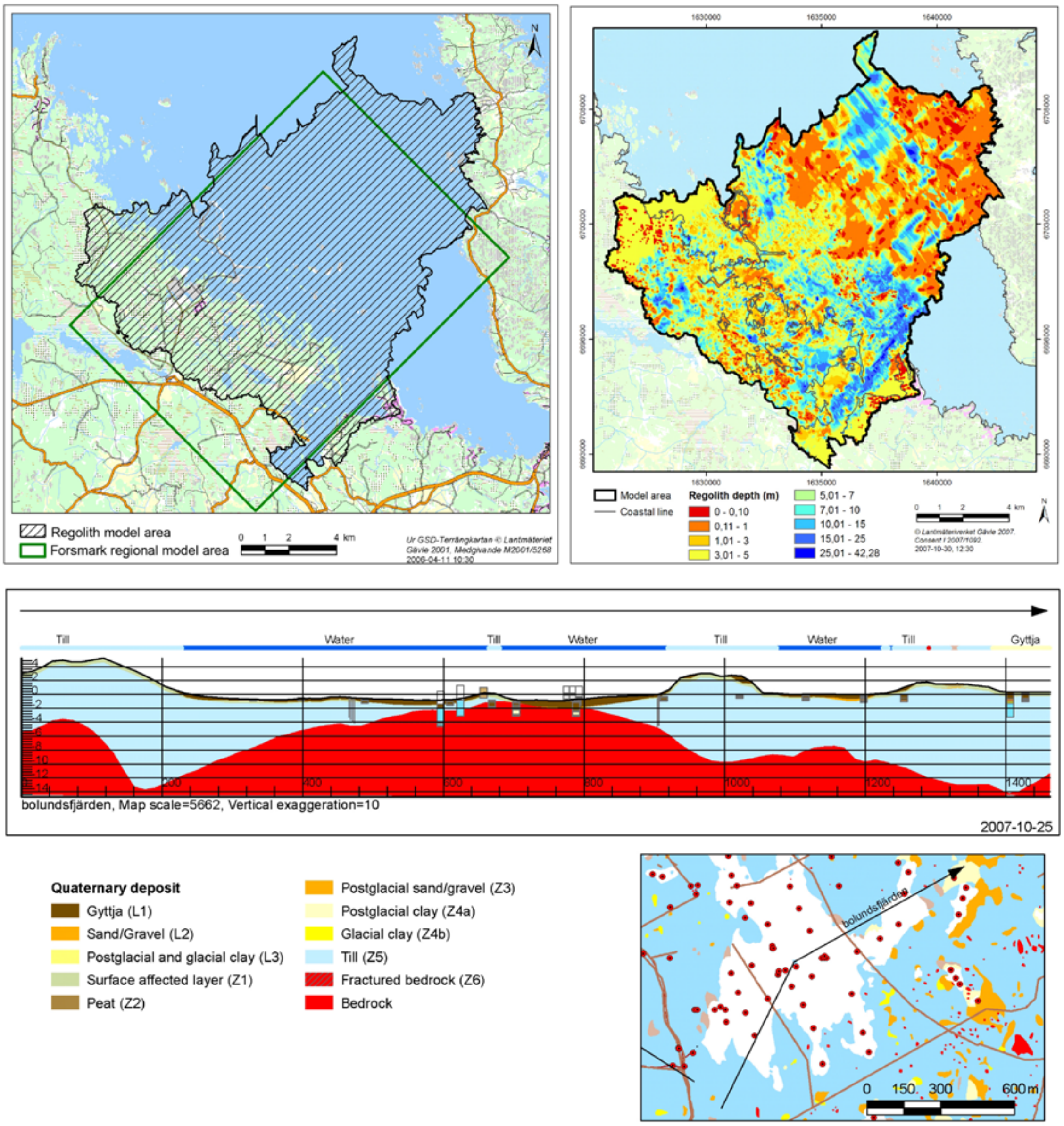

Figure 2-14. Top left: Extent of the model of the Quaternary deposits in stage 2.2. Top right: Interpreted total thickness of the Quaternary deposits. Bottom: Example cross-section showing the interpreted stratification and thicknesses of the Quaternary deposits beneath Lake Bolundsfjärden. (Based on figures from Appendix 2 of /Hedenström et al. 2008/.)

Table 2-5 and Table 2-6 show the parameter values provided for groundwater flow modelling by the surface system group /Bosson et al. 2008/. Most of the values represent so-called ‘best estimates’ based on site-specific data supported by generic data when site-specific data are scarce, cf /Johansson 2008/.

This complex stratigraphy is handled in different ways in the SDM studies depending on the objectives of the flow modelling and the software used, see /Follin et al. 2007b/ and /Bosson et al. 2008/. In /Follin et al. 2007b/, the Quaternary deposits are substituted by four element layers each of constant 1 m thickness. The same equivalent hydraulic conductivity tensor was specified for each vertical stack of four grid elements, but was varied horizontally from element-to-element, and is anisotropic between horizontal and vertical components. The horizontal component of the tensor is based on the arithmetic mean of the hydraulic properties of the original stratigraphy, whereas the vertical component is based on its harmonic mean. The resulting hydraulic conductivity distribution is illustrated in Figure 2-15.

Table 2-5. Values of the total porosity and the specific yield of the Quaternary deposits suggested for groundwater flow modelling in SDM stage 2.2. (Modified after Table 2-4 in /Bosson et al. 2008/.)

Layer	Total porosity [–] and specific yield [–] of layers with several types of Quaternary deposits					
	Fine till	Coarse till	Gyttja	Clay	Sand	Peat
L1	–	–	0.50 / 0.03	–	–	0.60 / 0.20
Z1	0.35 / 0.15	0.35 / 0.15	–	0.55 / 0.05	0.35 / 0.20	0.40 / 0.05
Z5	0.25 / 0.03	0.25 / 0.05	–	–	–	–
	Total porosity [–] and specific yield [–] of layers with one type of Quaternary deposits					
L2	0.35 / 0.20					
L3	0.55 / 0.05					
Z2	0.40 / 0.05					
Z3	0.35 / 0.20					
Z4	0.45 / 0.03					

Table 2-6. Values of the saturated hydraulic conductivity of the Quaternary deposits suggested for groundwater flow modelling in SDM stage 2.2. (Modified after Table 2-4 in /Bosson et al. 2008/.)

Layer	*K* [m/s] of layers with several types of Quaternary deposits					
	Fine till	Coarse till	Gyttja	Clay	Sand	Peat
L1	–	–	$3 \cdot 10^{-7}$	–	–	< 0.6 m depth: $1 \cdot 10^{-6}$
Z1	$3 \cdot 10^{-5}$	$3 \cdot 10^{-5}$	–	$1 \cdot 10^{-6}$	$1.5 \cdot 10^{-4}$	> 0.6 m depth: $3 \cdot 10^{-7}$
Z5	$1 \cdot 10^{-7}$	$1.5 \cdot 10^{-6}$	–	–	–	–
	K **[m/s] of layers with one type of Quaternary deposits**					
L2	$3 \cdot 10^{-4}$					
L3	< 0.6 m depth: $1 \cdot 10^{-6}$; > 0.6 m depth: $1.5 \cdot 10^{-8}$					
Z2	$3 \cdot 10^{-7}$					
Z3	$1.5 \cdot 10^{-4}$					
Z4	$1.5 \cdot 10^{-8}$					

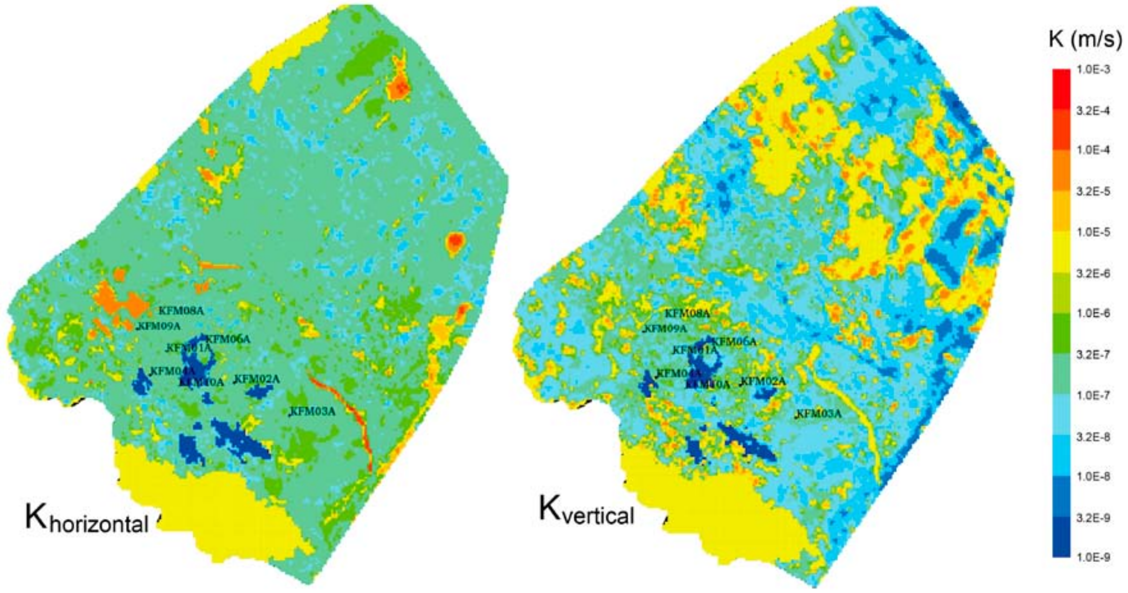

Figure 2-15. *Resulting effective hydraulic conductivity for HSD top layer based on Quaternary deposits layer thicknesses and hydraulic properties. Left: E-W horizontal component. Right: vertical component. (Source: Figure 6-10 in /Follin 2008/.)*

2.5 Groundwater flow modelling and confirmatory testing

The main objectives of the groundwater flow modelling carried out for the SDM are to investigate the behaviour of a numerical implementation of the conceptual hydrogeological model and test its performance against three sets of confirmatory data:

- transient, large-scale cross-hole (interference) test responses,
- steady-state, natural (undisturbed) groundwater levels in the uppermost 150 m, and
- hydrochemical observations in deep boreholes.

In general, the behaviour of the numerical flow model is found to be sound and the matching against the confirmatory data sets reasonable. However, it is noted that the performance of the groundwater flow model, which is based on equivalent continuous porous media (ECPM) properties, is slightly improved if the anisotropy of the horizontal to vertical hydraulic conductivity ratios of the upscaled values for both the Quaternary deposits (HSD) and the fracture domains (HRD) are increased compared with the up-scaled values derived from the initial structural-hydraulic settings described above. The objective of the multiple simulations carried out in /Follin et al. 2008/ is to address the sensitivity of the resulting calibrated deterministic base model simulation developed in /Follin et al. 2007b/ to parameter uncertainty, e.g. heterogeneity.

3 Concepts and methodology

3.1 Governing equations

Coupled groundwater flow and salt transport in fractured rocks that give rise to variations in salinity and hence fluid density are modelled in DarcyTools according to the following formulation of the mass conservation equation:

$$\frac{\partial \rho \phi}{\partial t} + \frac{\partial}{\partial x}(\rho u) + \frac{\partial}{\partial y}(\rho v) + \frac{\partial}{\partial z}(\rho w) = Q \qquad (3\text{-}1)$$

where ρ is fluid density [ML^{-3}], ϕ is the kinematic porosity [–], t is time [T], (u, v, w) are the directional components of the volumetric (Darcy) flux [LT^{-1}] at the location (x, y, z) [L,L,L] in a Cartesian coordinate system, and Q is a source/sink term per unit volume of fluid mass [$ML^{-3}T^{-1}$]. The mass conservation equation is turned into a pressure equation by invoking the assumptions behind Darcy's law:

$$\begin{aligned} \rho u &= -\frac{K_x}{g}\frac{\partial P}{\partial x} \\ \rho v &= -\frac{K_y}{g}\frac{\partial P}{\partial y} \\ \rho w &= -\frac{K_z}{g}\frac{\partial P}{\partial z} - K_z(\rho - \rho_0) \end{aligned} \qquad (3\text{-}2)$$

where K_x, K_y and K_z are the orthogonal components of the hydraulic conductivity tensor parallel to the Cartesian coordinate system [LT^{-1}], g is the acceleration due to gravity [LT^{-2}], ρ_0 is a reference fluid density [ML^{-3}], and P is the dynamic (residual) fluid pressure [$ML^{-1}T^{-2}$] at the location (x, y, z):

$$P = p + \rho_0 g z \qquad (3\text{-}3)$$

where p is the gauge pressure [$ML^{-1}T^{-2}$] and $\rho_0 g z$ is the hydrostatic pressure, P_0.

The hydraulic conductivity K is related to the permeability k [L^2] through the relation:

$$K = \frac{\rho g}{\mu} k \qquad (3\text{-}4)$$

where μ is the fluid dynamic viscosity [$ML^{-1}T^{-1}$]. For variable-density flow at isothermal conditions, ρ and μ are given by the following state laws:

$$\rho = \rho_0 [1 + \alpha C] \qquad (3\text{-}5)$$

$$\mu = \mu_0 \qquad (3\text{-}6)$$

where α and μ_0 are constants and C represents the salinity (mass fraction) [–]:

$$C = TDS / \rho \qquad (3\text{-}7)$$

The migration of salt is modelled in DarcyTools in terms of advection and dispersion processes in the mobile (fracture) pore system and as a diffusion process in the immobile (rock matrix) pore system. The advection-dispersion equation for the mobile pore system is modelled in DarcyTools according to the following equation:

$$\begin{aligned} \rho\phi\frac{\partial C}{\partial t} &+ \frac{\partial}{\partial x}\left(\rho u C - \rho\gamma D_x \frac{\partial C}{\partial x}\right) \\ &+ \frac{\partial}{\partial y}\left(\rho v C - \rho\gamma D_y \frac{\partial C}{\partial y}\right) \\ &+ \frac{\partial}{\partial z}\left(\rho w C - \rho\gamma D_z \frac{\partial C}{\partial z}\right) = QC + Q_C \end{aligned} \qquad (3\text{-}8)$$

where D_x, D_y and D_z are the orthogonal components of the diffusion tensor parallel to the Cartesian coordinate system [L^2T^{-1}], Qc represents the diffusive exchange of salt per unit volume of fluid mass between the mobile and immobile pore volumes [$ML^{-3}T^{-1}$], and γ is a dimensionless coefficient that describes the dependency of the kinematic porosity of the mobile pore system on the dynamic pressure:

$$\phi = \phi_0 \gamma \tag{3-9}$$

$$\gamma = 1 + \frac{S_s}{\phi_0} \frac{(P - P_0)}{\rho g} \tag{3-10}$$

where S_s is the specific storage of the mobile pore system [L^{-1}]. For the sake of clarity, it is noted that hydrodynamic dispersion (dispersivity) is not considered in Equation (3-8). The classic continuum concept of longitudinal and transverse dispersion is replaced by the notion that it is sufficient to work with a fine grid discretisation of the underlying discrete fracture network realisation. DarcyTools uses an unstructured computational grid that allows for complex and spatially varying grid refinements including grid discontinuities. The usage of the latter feature is discussed in Appendix E.

3.2 Methodology

3.2.1 Finite volume method

DarcyTools uses a staggered computational grid, which means that scalar quantities such as pressure, flow porosity and salinity use a cell-centred mesh, whereas directional quantities such as hydraulic conductivity, hydrodynamic diffusivity, mass flux, and Darcy flux use a mesh centred at the cell walls. This grid arrangement is first introduced by /Harlow and Welch 1965/ and is described in textbooks, e.g. /Patankar 1980/. Each variable is assumed to be representative for a certain control volume, which is the volume for which the equations are formulated. DarcyTools uses the finite volume method to transform the differential equations into algebraic equations of the type:

$$a_P\Phi_P = a_W\Phi_W + a_E\Phi_E + a_S\Phi_S + a_N\Phi_N + a_B\Phi_B + a_T\Phi_T + S_\phi \tag{3-11}$$

where Φ denotes the variable in question, a_i are directional coefficients (West, East, South, North, Bottom, and Top) and S_ϕ represents source/sink terms. The equations are solved by the MIGAL multi-grid equation solver /Svensson et al. 2010/.

3.2.2 Continuum representation of hydraulic properties of discrete fractures

Principle

The principle used to represent hydraulic properties of discrete fractures as equivalent grid cell hydraulic properties in DarcyTools works as follows:

A fracture variable (P_f) contributes to the grid cell variable (P_c) by an amount which is equal to the intersecting volume of the fracture (V_f) times the value of the fracture variable. Contributions from all fractures (N) that intersect the grid cell control volume are added and the sum is divided by the volume of the cell (V_c), i.e.:

$$P_c = \sum_{i=1}^{N} \left(V_f \, P_f\right)_i / V_c \tag{3-12}$$

The intersecting volume of the fracture ,*f* may be written as:

$$V_f = L_f \, W_f \; b_f \tag{3-13}$$

where L_f , W_f and b_f denote the physical dimensions (length, width and thickness) of the intersecting fracture in three orthogonal directions. For the sake of simplicity, it is assumed in the equations below that the fracture thickness b_f is much thinner than the geometrical resolution of the computational grid (the grid size).

Grid-cell hydraulic conductivity

DarcyTools assumes that fracture transmissivity (T_f) is a scalar quantity and that fracture hydraulic conductivity (K_f) may be written as:

$$K_f = T_f / b_f \tag{3-14}$$

where bf is the fracture thickness. Thus, the contribution from an intersecting fracture to the hydraulic conductivity of the intersected grid cell may be written as:

$$(K_c)_f = etc = (L_f \ W_f \ T_f) / V_c \tag{3-15}$$

Since DarcyTools uses a staggered computational grid, K_c is a directional quantity.

Grid-cell kinematic porosity

DarcyTools assumes that the kinematic porosity of a fracture (ϕ_f) can be written as:

$$\phi_f = (e_t)_f / b_f \tag{3-16}$$

where $(e_t)_f$ is the fracture transport aperture. The fracture transport aperture is modelled based on Äspö Task Force 6c results /Dershowitz et al. 2003/, which assume a power-law function between the fracture aperture and the fracture transmissivity:

$$(e_t)_f \ = a \ (T_f)^b \tag{3-17}$$

The values of the parameters a and b used in this work are defined in /Dershowitz et al. 2003/, where $a = 0.46$ and $b = 0.5$.

Thus, the contribution from an intersecting fracture to the kinematic porosity of the intersected grid cell can be written as:

$$(\phi_c)_{,f} \ = (L_f \ W_f \ (e_t)_f) / V_c \tag{3-18}$$

3.2.3 Fracture transmissivity

The equations given in section 3.2.2 reveal that fracture transmissivity is the key hydraulic quantity in DarcyTools, i.e. fracture transmissivity is used to define both grid cell hydraulic conductivity and grid cell kinematic porosity.

DarcyTools assumes that a power-law function prevails between fracture transmissivity and fracture size (L_f). The power-law function may be written as:

$$\log(T_f) = \log\left[a_T\left(\frac{L_f}{100}\right)^{b_T}\right] + d_T U[-0.5,0.5] \tag{3-19}$$

where a_T is the transmissivity value of a fracture with $L_f = 100$ m and b_T is the exponent of the power-law function. d_T is a factor that scales a uniformly distributed random deviate U and is used when uncertainty in the power-law function is addressed.

For the sake of clarity it is noted that the relationship between the power-law parameters used in DarcyTools (a_T,b_T) and the corresponding power-law parameters (a,b) derived in SDM-Site and recommended for use in SR-Site Forsmark /Selroos and Follin 2010/ can be written as:

$$b_T = b \tag{3-20}$$

$$a_T = a \left(100 / \sqrt{\pi}\right)^{b_T} \tag{3-21}$$

For the sake of clarity, it is emphasised that the stochastic fractures used in the work reported here are imported from the flow modelling of periods of temperate climatecondition /Joyce et al. 2010/, see section 4.2.

3.2.4 Particle tracking

The particle tracking routine, PARTRACK, has two modes of operation; the first is the classic way of moving the particle along the local velocity vector, whereas the second method uses the so called "flux-weighting" approach, and works as follows.

- A particle entering a scalar cell will, if no dispersion effects are activated, stay in the cell for a time that is equal to the free volume of the cell divided by the flow rate through the cell.
- When the particle is ready to leave the cell, it will leave through one of the cell walls that has an outgoing flow direction. The choice between cell walls with an outgoing flow is made with a likelihood that is proportional to the outflows. If several particles are traced, the cloud will thus split up in proportion to the flow rates. Complete mixing in a cell is assumed.

3.2.5 Diffusive exchange of salt

In DarcyTools, the exchange of dissolved solids between the fracture water and the matrix porewater is modelled with a one-dimensional multi-rate diffusion model /Haggerty and Gorelick 1995/. The diffusion process is represented by a series of discrete exchange rate coefficients, α_{min}–α_{max} [T^{-1}], where the time scale of the remotest diffusive exchange is $1/\alpha_{min}$. Another parameter governing the diffusion process in the model of /Haggerty and Gorelick 1995/ is the ratio between the diffusive and advective pore spaces, β [-]. In fractured crystalline rock, the matrix porosity is approximately 10–100 times greater than the kinematic porosity /Follin et al. 2005/.

The chosen range of values of the exchange rate coefficients not only affects the time scales but also the penetration depths of the multi-rate diffusion process. In the work reported here, ten exchange rate coefficients are used. The value of α_{min} is set to $1 \cdot 10^{-10}$ s^{-1}, which implies a time scale of approximately 300 years for the remotest diffusive exchange. The value of β is set to 10, i.e. ten times more pore space in the matrix than in the fractures. Both settings are regarded as conditional. Other parameter values would imply other time scales.

4 Model specification

4.1 Additional concepts and methodology

The concepts and methodology shown in Chapter 1 can be used to satisfy the following two objectives of the work:

- predict the magnitude and spatial distribution of the inflow, and
- predict the magnitude and spatial distribution of the upconing of deep saline water.

In order to fulfil the remaining objectives of the work, i.e.:

- predict the magnitude and spatial distribution of the drawdown of the groundwater table,
- predict the role of grouting for the inflow, drawdown and upconing phenomena, and
- predict the saturation period after the open repository has been closed (backfilled), the following algorithms/routines are added.
- The position of the groundwater table is modelled with a free surface algorithm that can handle both natural conditions and the drawdown due to the inflow to an open repository (Appendix A).
- The impact of grouting on the calculated inflow rates, drawdown of the groundwater table and upconing of deep saline water is studied by altering the hydraulic conductivity of the computational grid cells in contact with the modelled repository (Appendix B).
- The time scale of the saturation period is estimated by assuming that the hydration process of the unsaturated parts of the backfill can be modelled as single-phase (saturated) groundwater flow, where the specific storage of the backfill varies in space depending on the transients in the dynamic pressure (Appendix C).

4.2 Base case

The requirements of SR-Site on the hydrogeological modelling of the excavation and operational phases may be summarised as follows:

- The model domain and the elevation of the top surface are the same as in the SDM work (Figure 4-1).
- The geometry and hydraulic properties of discrete geological features in the bedrock such as deformation zones, sheet joints and fracture network realisations are the same as in the SDM work. The specific values used are imported from the groundwater flow modelling of the temperate period carried out by /Joyce et al. 2010/ (Figure 4-2, Figure 4-3 and Figure 4-4). Concerning the hydraulic properties of the uppermost 20 m of the model domain (including the minimum values of the hydraulic properties below 20 m depth), the values shown in Table 4-1 and Figure 4-5 are applied.
- The salinity and pressure during the simulation of the excavation and operational phases are fixed on the lateral sides of the model domain implying unaffected steady-state conditions a few kilometres away from the modelled repository.
- The salinity and pressure values used on the lateral boundaries are derived from a simulation of the shoreline displacement and the known changes of the salinity in the Baltic basin in the Forsmark area during Holocene time, i.e. between 8000 BC and 2000 AD (Figure 4-6). (The lateral surfaces of the model domain are modelled as impervious boundaries (no flow and no diffusion of salt) during Holocene time and the initial conditions at 8000 BC are in accordance with those used in the SDM work (Table 4-2).

- The terrestrial parts of the top surface of the model area are assigned a fixed maximum value of the mean net precipitation of 130 mm/y of fresh water in all simulations. Likewise, the bottom surface of the model domain is modelled as an impervious flow boundary with a fixed salinity in all simulations. The bottom surface is located at the same depth as in the SDM work, –1,200 m elevation.
- Present-day lakes, wetlands, main surface water (stream) runoff and groundwater chemistry are loosely used as "calibration targets" for the modelled evolution of the hydrological and hydrochemical conditions during Holocene time (Figure 4-7 and Figure 4-8). The simulated conditions at 2000 AD are used as reference for the identification of disturbances caused by the subsequent flow modelling of the excavation and operational phases.
- The location and geometry of a final repository at Forsmark is imported from /SKB 2008b/ (Figure 1-2 and Figure 4-9).
- Three scenarios (operation stages A–C) of the repository development are studied, i.e. not all parts of the repository are in operation (depressurised) at the same time (Figure 1-2).
- Three levels of grouting efficiency, I–III, are studied for each operation stage A–C (Table 4-3).
- For the modelling of the saturation process following the closure of the operational phase, the backfill material is assumed to have hydraulic properties similar to Friedland Clay /Börgesson et al. 2006/.
- Two thresholds of the inflow rate to any deposition hole are analysed as a means to quantify the effect of using hydraulic criteria for rejecting a deposition hole:

  Q1: Deposition hole inflow is greater than 0.1 L/min.

  Q2: Deposition hole inflow is greater than 1% of the total inflow to the deposition tunnel (including its deposition holes).

The two inflow rate criteria are analysed alone and in combination with two geometry-based fracture rejection criteria, referred to as FPC (full perimeter criterion) and EFPC (expanded FPC), see Figure 4-10 and Figure 4-11. In summary, the following four variants of deposition hole rejection criteria are analysed:

I. {Q1}
II. {Q2}
III. {Q1 ∪ Q2}
IV. {Q1 ∪ Q2} | exclusion of {FPC ∪ EFPC}

The prioritised variants of the scenario analyses carried out for SR-Site are number III and number IV. Variant III looks at the combination of criteria Q1 and Q2 and Variant IV looks at the combination of criteria Q1 and Q2 after all deposition hole positions that fail the combination of criteria FPC and EFPC have been excluded.

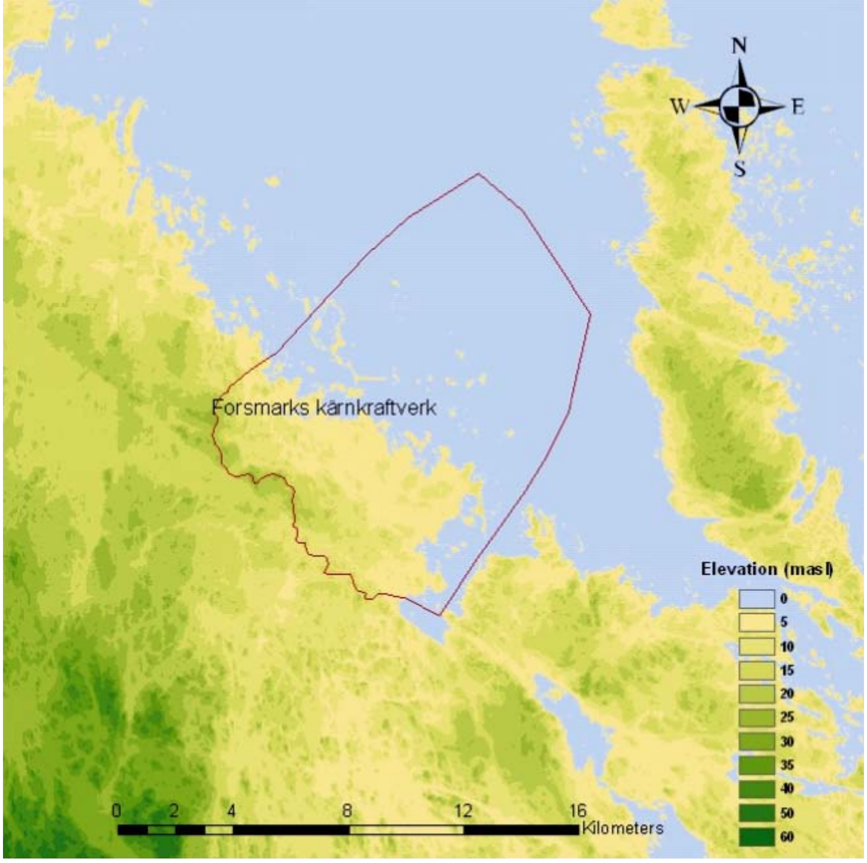

Figure 4-1. *Regional topography in the Forsmark area based on the F2.2 digital elevation map on a 20 m grid scale. The regional model domain is shown by the red line. (Geographic data ©Lantmäteriverket Gävle 2007. Consent I 2007/1092).*

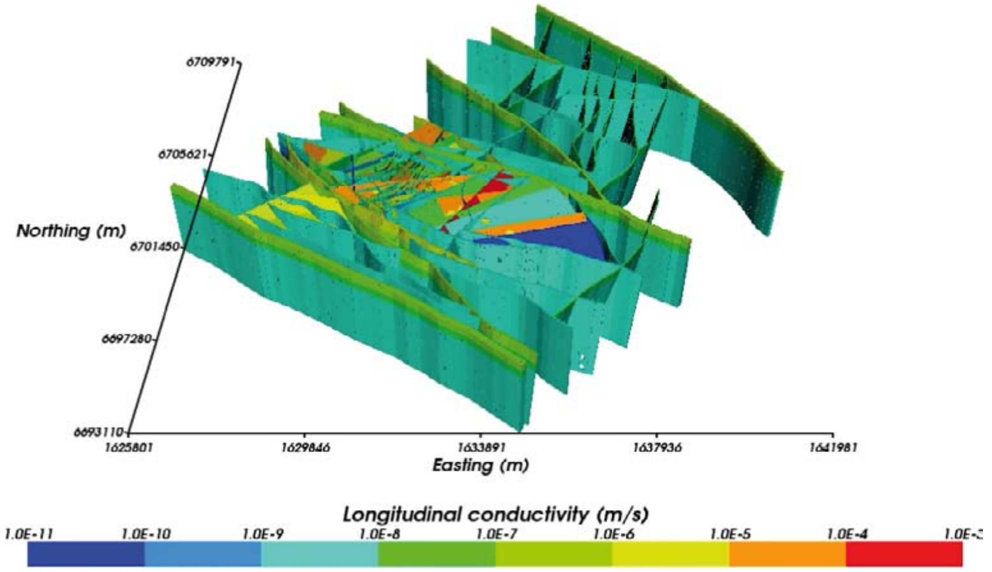

Figure 4-2. *Visualisation of regional and local scale deformation zones (HCD). Each zone is coloured by its hydraulic conductivity and drawn according to its inferred hydraulic thickness. The y-axis points towards north. (Source: Figure 4-1 in /Joyce et al. 2010/.)*

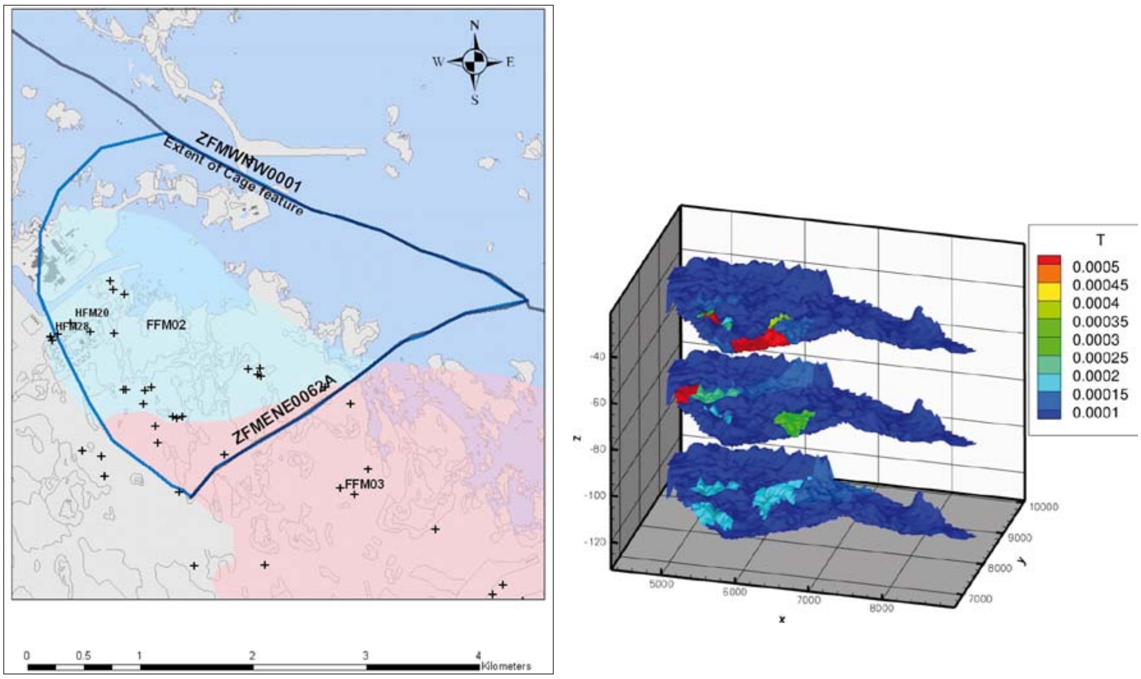

Figure 4-3. *The hypothesised lateral extent (left) and elevations (right) of the discrete features modelled to represent the sheet joints observed in the shallow bedrock aquifer in the SDM work (cf Figure 2-10 and Figure 2-11). The crosses in the left image mark the positions of percussion- and core-drilled boreholes for which transmissivity measurements are available. The bluish area in the upper image represents fracture domain FFM02 and the pinkish area represents fracture domain FFM03. (Source: Figure 5-17 in /Follin 2008/.)*

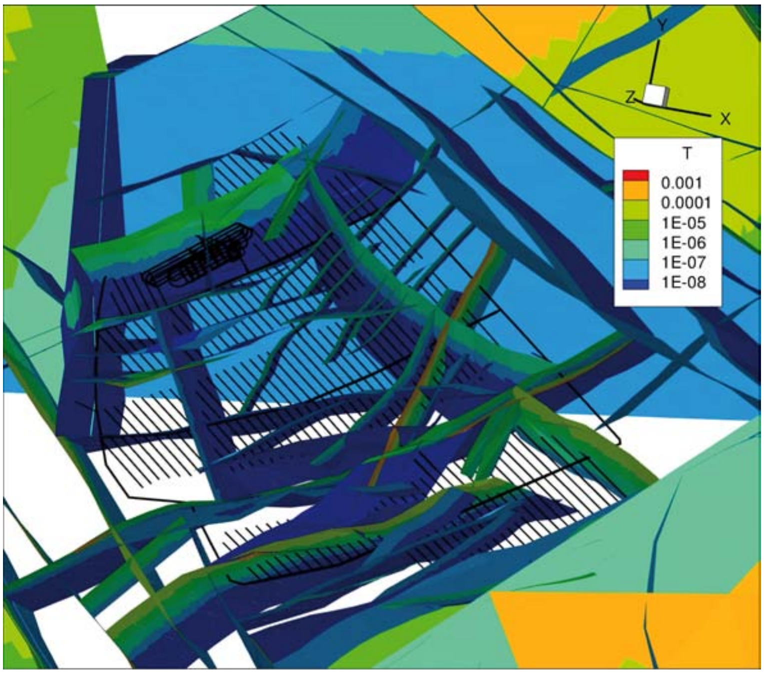

Figure 4-4. *Example view of the repository layout at −465 m elevation and some of the deterministically modelled deformation zones nearby. In the base case, the deformation zones have homogeneous hydraulic properties with depth dependency according to Equation (2-1). (Some zones are deleted in this visualisation for the sake of visibility).*

Table 4-1. Grid cell hydraulic properties applied in this work for the uppermost 20 m of the model domain and the minimum values allowed below this depth.

Property	Depth interval	Value
Hydraulic conductivity K_c [m/s]	< 20 m	$K_{c,h} = \max \begin{cases} 1 \cdot 10^{-7} \\ 5 \cdot 10^{-3}\, 10^{-Depth/3} \end{cases}$ $K_{c,v} = 1 \cdot 10^{-6}$
	≥ 20 m	$K_{c,h} \geq 1 \cdot 10^{-10}$ $K_{c,v} \geq 1 \cdot 10^{-10}$
Kinematic porosity ϕ_c [-]	< 20 m	$\phi_c = \max \begin{cases} 1 \cdot 10^{-3} \\ 5 \cdot 10^{-2}\, 10^{-Depth/20} \end{cases}$
	≥ 20 m	$\phi_c = 5 \cdot \max \begin{cases} 1 \cdot 10^{-5} \\ f(\phi_f);\ \phi_f = (0.46\sqrt{T_f})/b_f \end{cases}$ [2] T_f = fracture transmissivity b_f = fracture thickness
Specific storage S_s [m^{-1}]	≥ 0 m	$S_s = 1 \cdot 10^{-9}$

Table 4-2. Assumed initial conditions at 8000 BC at Forsmark /Selroos and Follin 2010/.

Region	Depth interval	Initial salinity
Footwall of zone A2 (FFM01, -02, -06)	Ground surface to –350 m	0%
	–350 m to –1,500 m	Linearly increasing to 7.2%
	Below –1,500 m	7.2%
Elsewhere	Ground surface to –500 m	0%
	–500 m to –2,300 m	Linearly increasing to 7.2%
	Below –2,300 m	7.2%

---

[2] The grid cell kinematic porosity is increased by five times to compensate for a reduced pore space due to the usage of a size-truncated Hydro-DFN model.

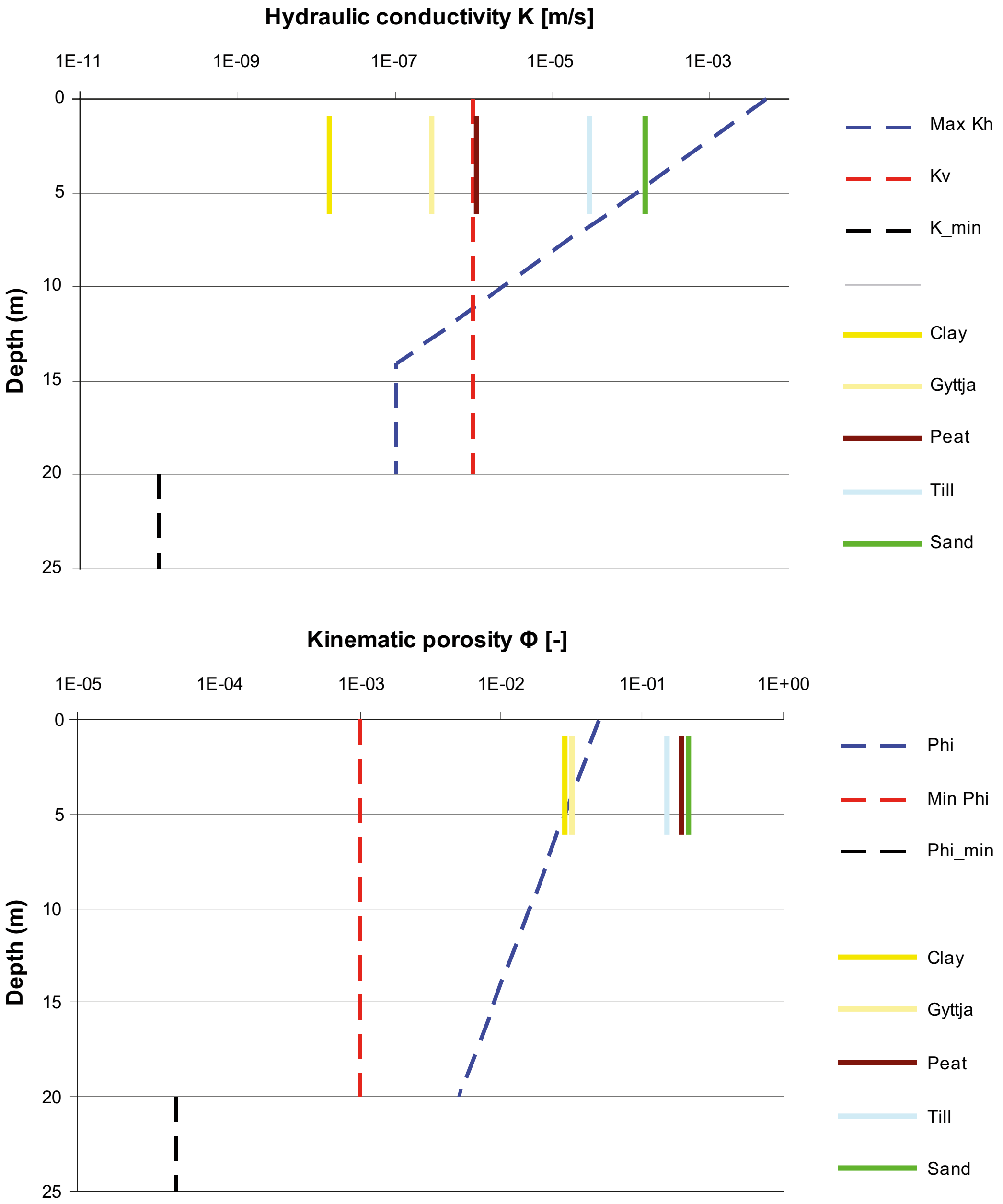

Figure 4-5. *The blue and red dashed lines represent the values used in this work to simulate the hydraulic properties of the Quaternary deposits and the uppermost bedrock. The black dashed lines represent the minimum values of hydraulic properties of the non-fractured parts of the bedrock below this depth (cf Table 4-1). The solid lines represent the values shown in Table 2-5 and Table 2-6.*

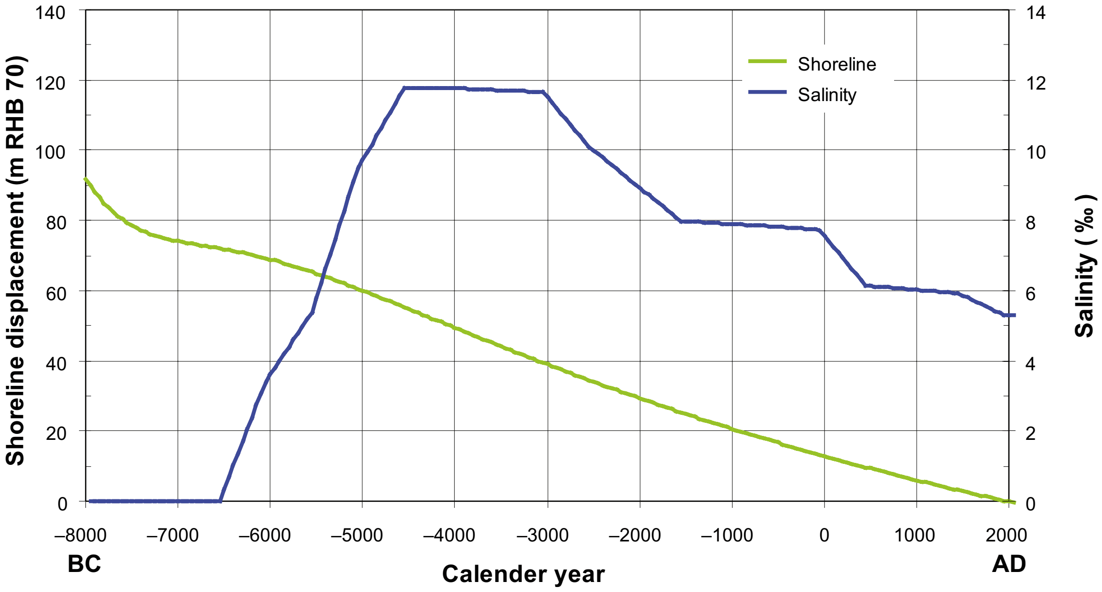

Figure 4-6. Evolution of the shoreline displacement and the salinity of the Baltic Sea close to Forsmark during Holocene time (8000 BC to 2000 AD). (Modified after Figure 2-9 and Figure 2-10 in /Follin 2008/.)

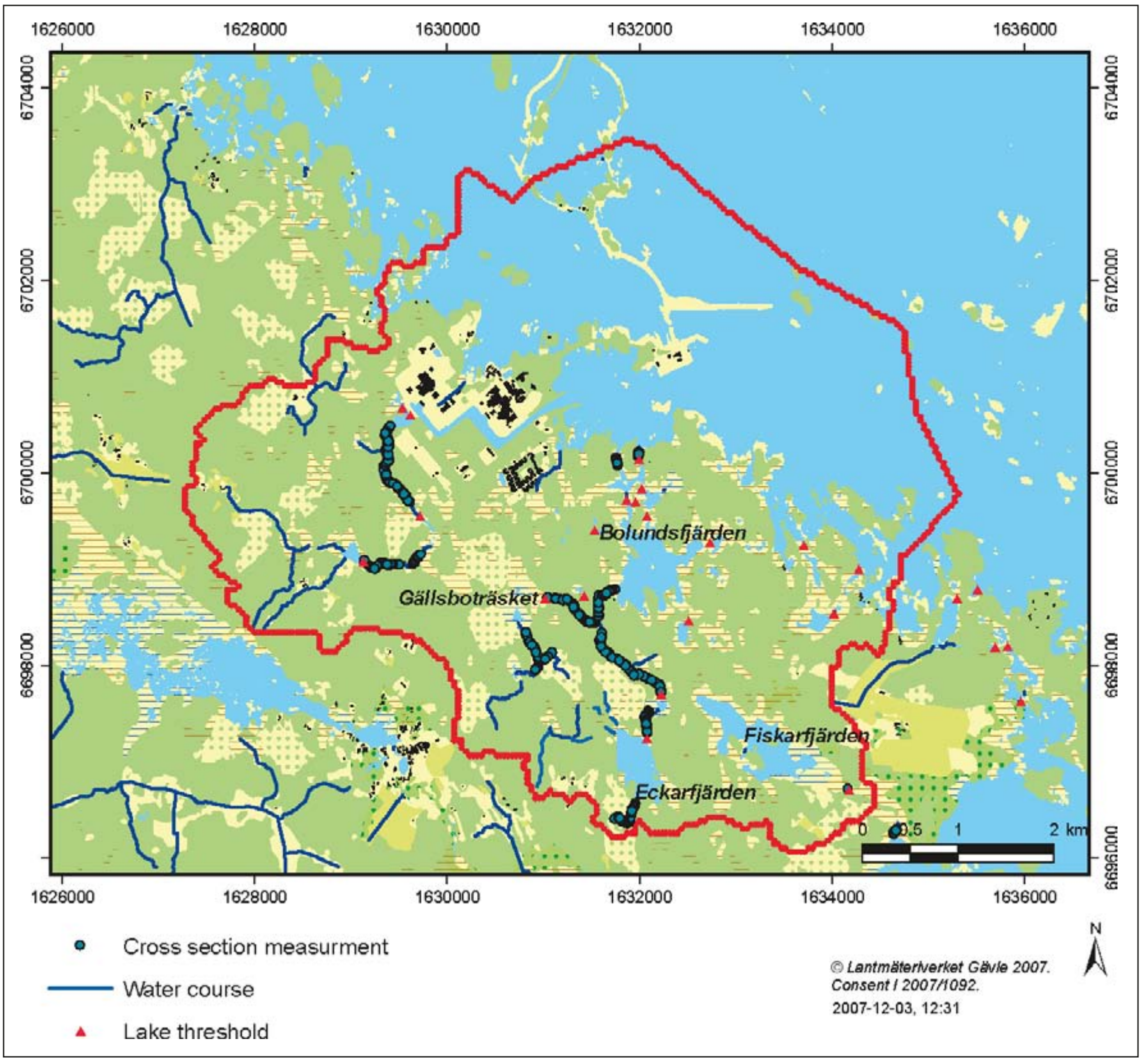

Figure 4-7. Location of major streams, major lakes (blue areas) and wetlands (white coloured areas) in the Forsmark area. (Modified after Figure 2-13 in /Bosson et al. 2008/.)

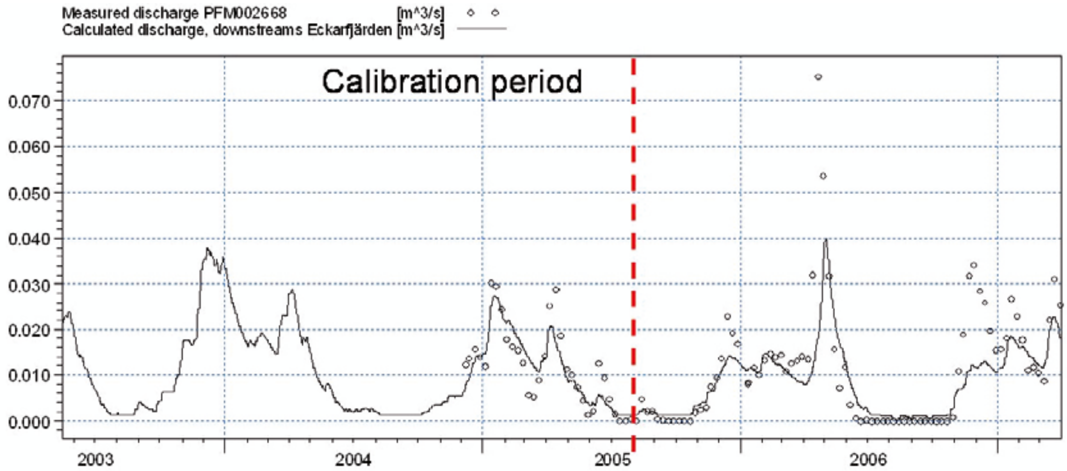

ME=0.00257794
MAE=0.00485087
RMSE=0.00885377
STDres=0.00847015
R(Correlation)=0.746629
R2(Nash_Sutcliffe)=0.496239

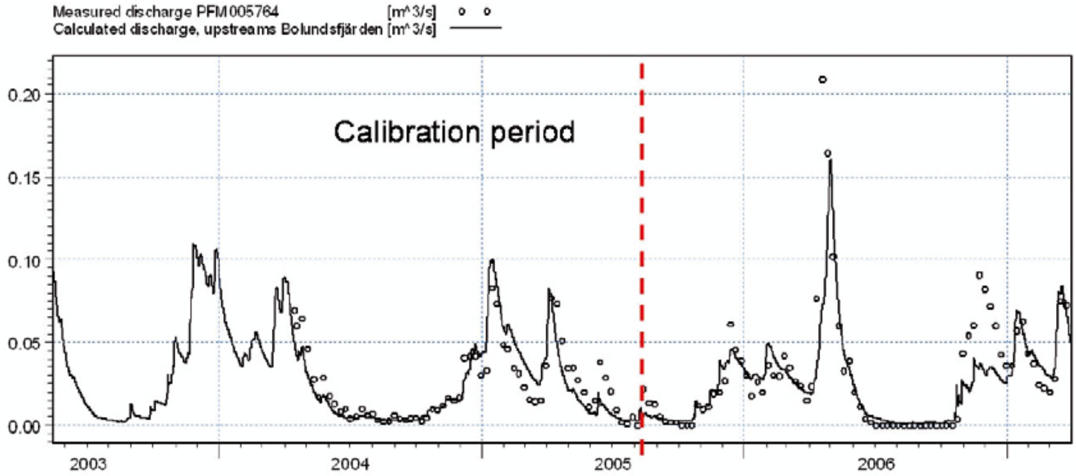

ME=0.00412174
MAE=0.0105443
RMSE=0.0198595
STDres=0.0194271
R(Correlation)=0.786033
R2(Nash_Sutcliffe)=0.600523

Figure 4-8. *The open circles show weekly measured stream runoff (m^3/s) from Lake Eckarfjärden (top) and Lake Bolundsfjärden (bottom). The black lines show the simulated diurnal stream runoff in the SDM work using the MIKE SHE code. (Modified after Figure 5-6 and Figure 5-9 in /Bosson et al. 2008/.)*

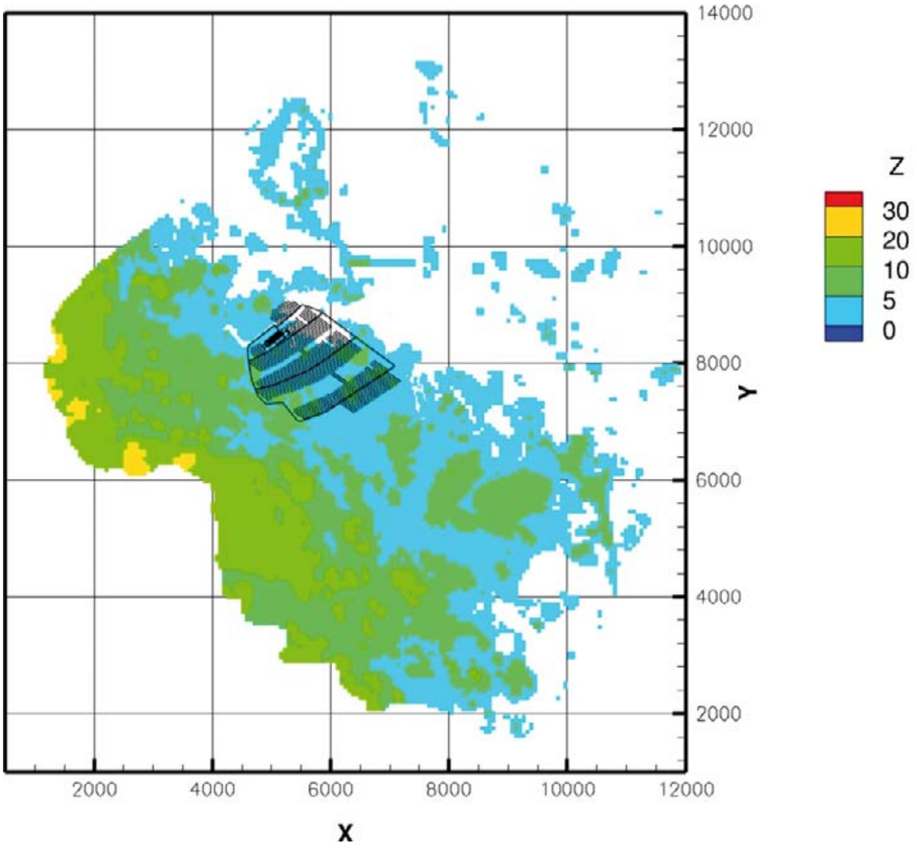

Figure 4-9. Plan view of the ground elevation and the suggested location of a final repository at Forsmark in local DarcyTools coordinates. The values shown in the legend are expressed in m RHB 70. The origin of the local coordinate system is placed at Easting: 1626000 and Northing: 6692000 with regard to the national 2.5 gon W 0:-15, RT 90 coordinates ("RAK system"). The y-axis in the local coordinate system points towards north.

Table 4-3. Definition of the studied levels of grouting efficiency.

Level	Definition
I	The hydraulic conductivity of all cells in contact with the repository has a maximum value of $1 \cdot 10^{-7}$ m/s.
II	The hydraulic conductivity of all cells in contact with the repository has a maximum value of $1 \cdot 10^{-8}$ m/s.
III	The hydraulic conductivity of all cells in contact with the repository has a maximum value of $1 \cdot 10^{-9}$ m/s except where the modelled ungrouted hydraulic conductivity is 10^{-6} m/s or greater. At these positions the hydraulic conductivity has a maximum value of $1 \cdot 10^{-8}$ m/s.

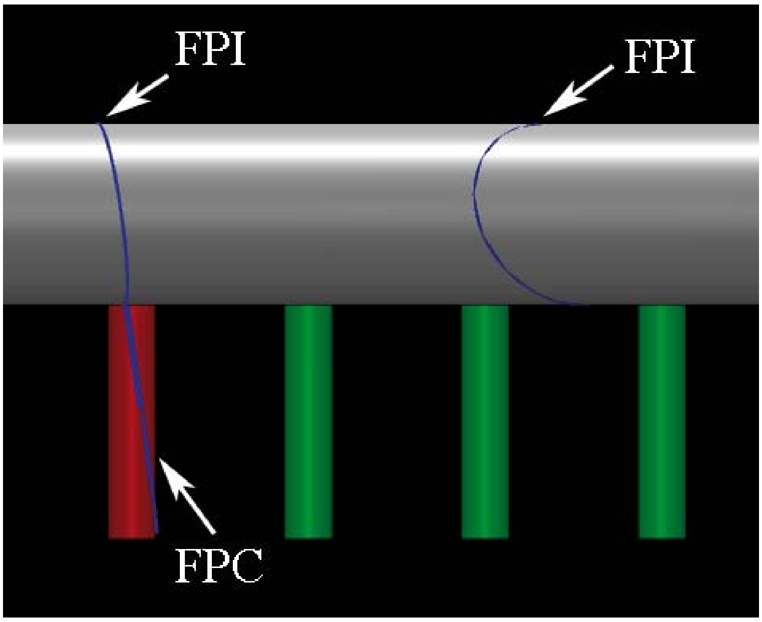

Figure 4-10. *Definition of FPI (Full Perimeter Intersection) and FPC (Full Perimeter Criterion). The FPI mapped in the deposition tunnel is judged to represent the trace of a discriminating fracture, FPC, if its projection intersects the deposition hole. (Figure 5-1 in /Munier 2006/.)*

Figure 4-11. *Definition of EFPC (Expanded Full Perimeter Criterion). A potentially discriminating fracture can remain undetected despite the use of the FPC in the deposition tunnel. (Figure 5-2 in /Munier 2006/.)*

4.3 Sensitivity study

Seven cases are studied as a means to study the sensitivity of the base model simulation to variations in the geometrical and hydraulic properties other than the impact of different levels of grouting efficiency.

1. The number of possible deposition holes is reduced by honouring the union probability of the FPC and EFPC criteria (cf Figure 4-10 and Figure 4-11).
2. A single deposition tunnel (Figure 4-13).
3. A stochastic representation of the deformation zone properties (Figure 4-14) together with another (second) realisation of the stochastic Hydro-DFN model.
4. No salinity (fresh water groundwater flow).
5. The HRD outside the candidate area was modelled as a continuous porous medium (CPM) for SDM-Site Forsmark, with hydraulic properties as specified in Table 2-2. For the sake of SR-Site, the HRD outside the candidate area was also modelled as an equivalent continuous porous medium (ECPM) using a preliminary Hydro-DFN model developed for the bedrock around SFR /Öhman and Follin 2010/ (Table 4-4).
6. The amount of sea water recharge to the modelled repository is investigated by reducing the vertical hydraulic conductivity in the sediments below the Baltic Sea by two orders of magnitude. This case is combined with the previous case (a preliminary Hydro-DFN model developed for the bedrock around SFR).
7. Simultaneous operation of two repositories, a final repository for spent nuclear fuel and SFR, the existing repository for short-lived radioactive waste c 1 km north of the investigated candidate area (Figure 4-15).

Cases 1-3 are of interest for the operation of a final repository since they describe the sensitivity of the inflow rates to late changes in the usage of the planned repository (Case 1), a partially excavated repository (Case 2), and a spatial variability in the hydraulic properties (Case 3).

Cases 4-6 are of interest for the operation of a final repository; however the main objective for their inclusion is invoked by Case 7, i.e. to study the potential hydraulic interference due to a simultaneous operation of two repositories.

Case 7 is computationally more demanding than Cases 1-3 due to the inclusion of SFR, which required a different computational grid. As a means to simplify and speed up the groundwater flow simulations, it was decided to study the sensitivity of the inflow rates to a final repository using a constant fluid density and steady-state flow. These assumptions are studied in Case 4. The notion is that Cases 5-7 should adopt the same approach, i.e. a constant fluid density and steady-state flow, provided that the differences between the modified base case and Case 4 are minute.

The inclusion of SFR required an update of the hydrogeological model since SFR is located in a HRD that is modelled as a continuous porous medium (CPM) for SDM-Site Forsmark. The properties of this CPM are specified in Table 2-2. For the sake of Case 7, it is decided to designate Case 5 to study the sensitivity of the inflow rates to SFR as well as to a final repository for an extended Hydro-DFN model.

Since SFR is located below the Baltic Sea, it is decided to check the sensitivity of the inflow rates to SFR and a final repository for a different leakage through the off-shore (sea) sediments than through the on-shore (land) sediments. Thus, in Case 6 the vertical hydraulic conductivity of the HSD below the Baltic Sea is reduced by two orders of magnitude, from $1 \cdot 10^{-6}$ m/s to $1 \cdot 10^{-8}$ m/s.

It is not feasible to carry out the sensitivity study for all operation stages and grouting levels. For the sake of simplicity, we therefore used a modified setup of the base case as a reference.

- All construction parts of the repository layout are held open at the same time.
- The grouting efficiency is fixed to level II (see Table 4-3).

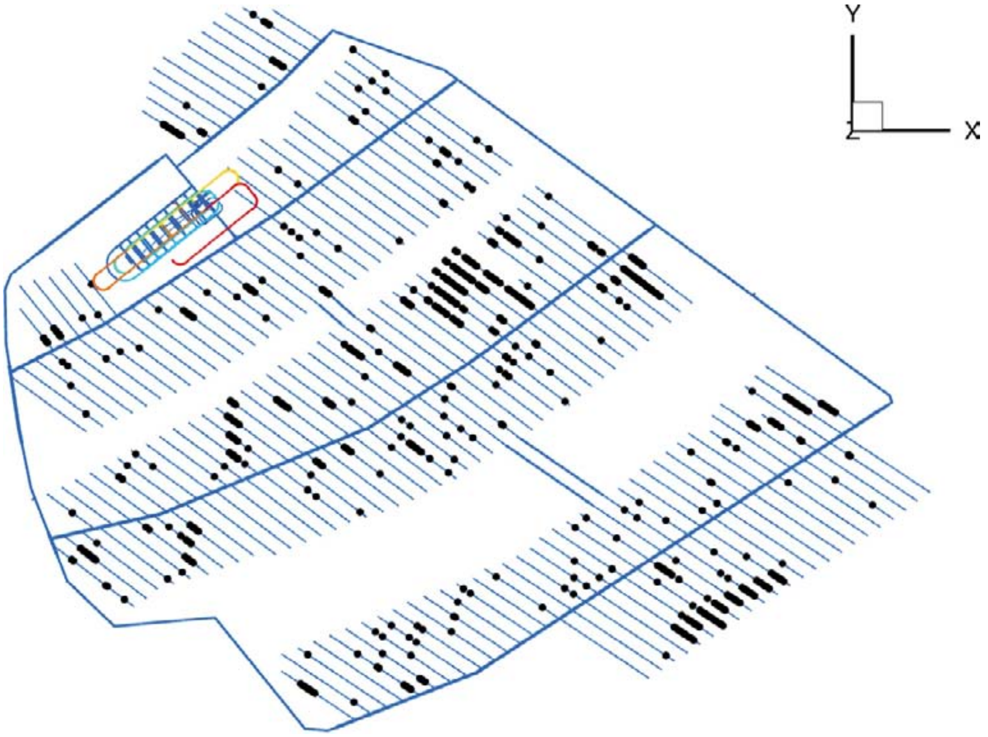

Figure 4-12. Plane view of the first variant and sensitivity test. The view shows the repository layout with the rejected deposition holes for the first realisation of the underlying Hydro-DFN model shown as dots. Out of a total of 6,916 possible deposition holes, 610 deposition holes are rejected based on the union probability of the FPC and EFPC criteria {FPC ∪ EFPC}. The y-axis points towards north.

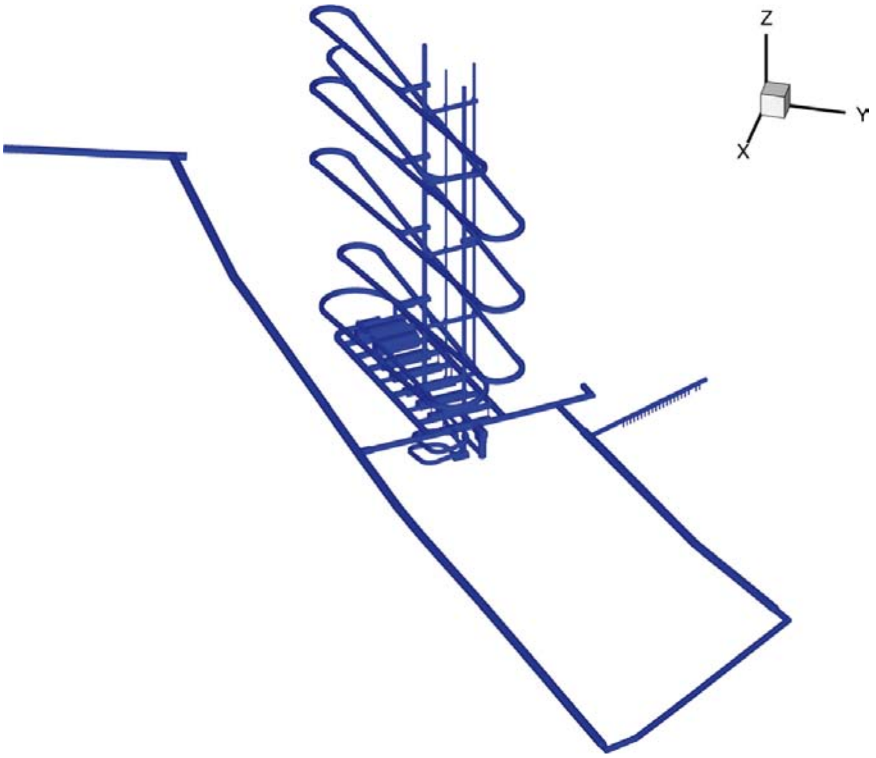

Figure 4-13. Visualisation of the second variant and sensitivity test, a single deposition tunnel. The y-axis points towards north.

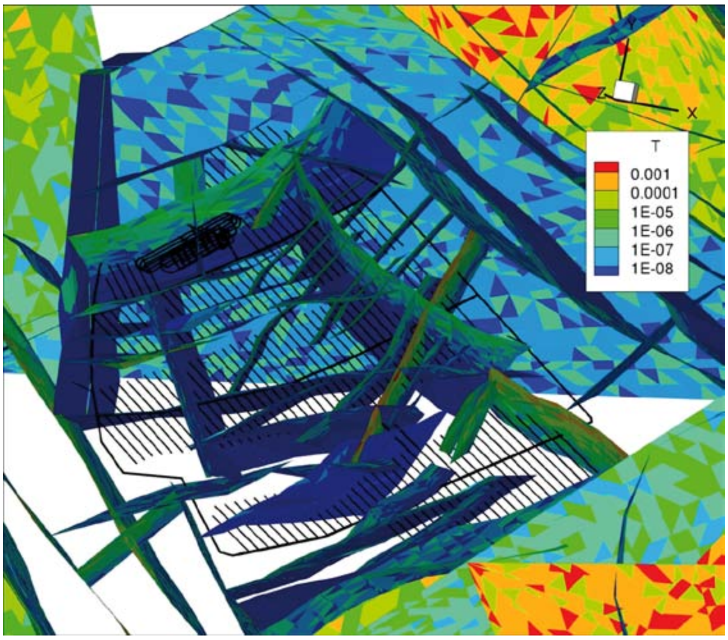

Figure 4-14. *Along with the second DFN realisation, the deformation zones are also modelled as heterogeneous. Stochastic hydraulic properties are generated according to Equation (2-3). The y-axis points towards north. (Some zones are deleted in this visualisation for the sake of visibility.)*

Table 4-4. Preliminary hydrogeological DFN parameters of the HRD outside the candidate area with depth dependency: above –60 m, –60 m to –245 m and below –245 m RHB 70. (Appendix A in /Öhman and Follin 2010/.)

Fracture domain (m RHB 70)	**Fracture set name**	**Orientation set pole: (trend, plunge), conc.**	**Size model, power-law** (r_0, k_r) (m, –)	**Intensity,** (P_{32})**, valid size interval:** $(r_0, 169\ m)$ (m^2/m^3)	**Parameter values for a correlated transmissivity model:** $T = a\ r^b$ (a,b)
> –60	EW	(3, 7) 12.6	(0.038, 3.45)	2.597	(6.0 · 10^{-9}, 1.29)
	NW	(233, 12) 13.2	(0.038, 3.10)	1.153	(8.0 · 10^{-9}, 1.13)
	NE	(128, 8) 11.7	(0.038, 3.45)	1.339	(1.0 · 10^{-9}, 1.25
	HZ	(116, 85) 27.6	(0.038, 2.60)	1.059	(2.0 · 10^{-8}, 1.48)
	GD	(232, 85) 6.5	(0.038, 2.79)	1.865	(3.7 · 10^{-8}, 1.16)
–60 to –245	EW	(5, 13) 8.5	(0.038, 3.45)	1.407	(6.0 · 10^{-9}, 1.29)
	NW	(234, 6) 12.3	(0.038, 2.95)	0.856	(8.0 · 10^{-9}, 1.13)
	NE	(128, 6) 11.5	(0.038, 3.45)	1.033	(1.0 · 10^{-8}, 1.25)
	HZ	(137, 84) 7.1	(0.038, 2.55)	0.848	(2.1 · 10^{-9}, 1.85)
	GD	(354, 85) 7.1	(0.038, 2.72)	1.204	(4.0 · 10^{-9}, 1.05)
< –245	EW	(3, 20) 9.7	(0.038, 3.45)	0.918	(6.0 · 10^{-9}, 1.29)
	NW	(233, 7) 14.9	(0.038, 3.10)	0.867	(8.0 · 10^{-9}, 1.13)
	NE	(305, 0) 11.2	(0.038, 3.45)	1.023	(1.0 · 10^{-8}, 1.25)
	HZ	(128, 81) 27.9	(0.038, 2.75)	0.595	(1.4 · 10^{-9}, 1.45)
	GD	(269, 85) 6.6	(0.038, 2.70)	1.283	(2.2 · 10^{-9}, 0.90)

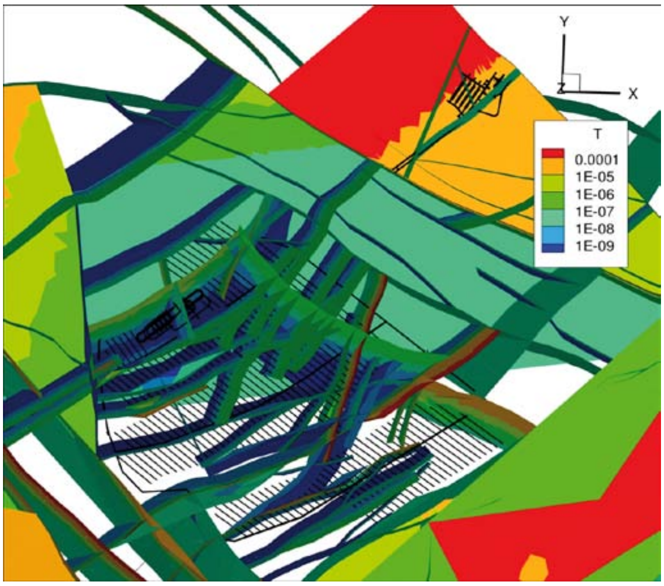

***Figure 4-15.** View showing a final repository for spent nuclear fuel at Forsmark and SFR, the existing repository for short-lived radioactive waste. The shortest distance between the two repositories is less than 1 km. The y-axis points towards north. In this image, the deformation zones have homogeneous hydraulic properties with depth dependency according to Equation (2-1). In addition, some zones are deleted for the sake of visibility.*

4.4 Grid setup and grid cell hydraulic properties

The discretisation of the computational grid is refined in the vicinity of the repository in order to resolve the repository layout and to study the effects of grouting. The largest cell size away from the repository is 128 metres (Figure 4-16 and Figure 4-17) and in the proximity of the repository the cell size is 4 metres (Figure 4-18). This high resolution is needed to resolve the deposition tunnels, which have a height of 4.8 metres and width of 4.2 metres. A vertical cross-section through the repository is shown in Figure 4-19. The vertical resolution of the cells close to the top boundary is 2 metres. In total about 1.4 million cells are used to model the problem as outlined. The origin of the local grid horizontal coordinates is positioned at (Easting, Northing) = (1626000, 6692000).

The vertical permeability field around the repository as implemented in the base case groundwater flow realisation is illustrated by two perpendicular vertical cross-sections and a horizontal plane at –465 m elevation in Figure 4-20. (It is recalled that the structural-hydraulic properties of the discrete features behind the base case realisation were imported from the temperate modelling work conducted by /Joyce et al. 2010/.)

Figure 4-21 and Figure 4-22 show horizontal close up views of the grid cell vertical permeability and kinematic porosity around the repository. The horizontal dimensions of the two views shown in Figure 4-21 and Figure 4-22 are approximately 2.5 km by 3.5 km, cf Figure 4-16. In Figure 4-23, the view in Figure 4-22 is accompanied by two other horizontal close up views of the grid cell kinematic porosity; –300 m and –600 m. Note that the repository layout is inserted in the views above and below repository depth in order to facilitate the reading.

Figure 4-24 and Figure 4-25 show cumulative density functions (CDFs) of k_c and ϕ_c at –465 m elevation for a regular 4 m lattice within a subarea of $(2\ \text{km})^2$ centred on the two views shown in Figure 4-21 and whereas the vertical permeability varies between $2 \cdot 10^{-17}\ \text{m}^2$ ($Kc,v \approx 1 \cdot 10^{-10}$ m/s) and $1.5 \cdot 10^{-13}\ \text{m}^2$ ($Kc,v \approx 7.5 \cdot 10^{-7}$ m/s).

The area with high kinematic porosity in the view at –300 m elevation in Figure 4-23 is the transmissive, gently dipping deformation zone ZFMA2. The repository is located in the footwall bedrock of this zone.

The significant contrast in kinematic porosity (hence also in hydraulic conductivity) between elevations –300 m and –600 m suggests that the changes in the groundwater chemistry at repository depth due to the excavation and operational phases will be more influenced by percolating shallow fresh and/or brackish water than by upconing of deep saline water.

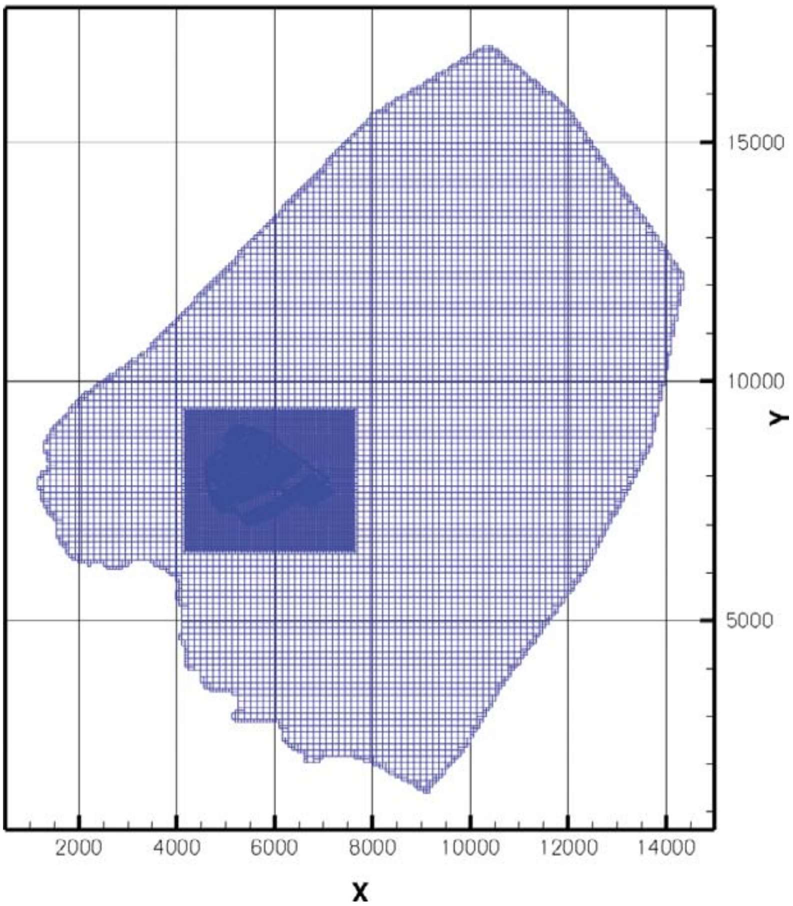

Figure 4-16. *Plane view of the model area and the computational grid at –465 m elevation. The size of the largest grid cells is 128 m. Within an area of about 3.5 km times 2.5 km around the repository the grid size is refined using an unstructured grid. The y-axis points towards north.*

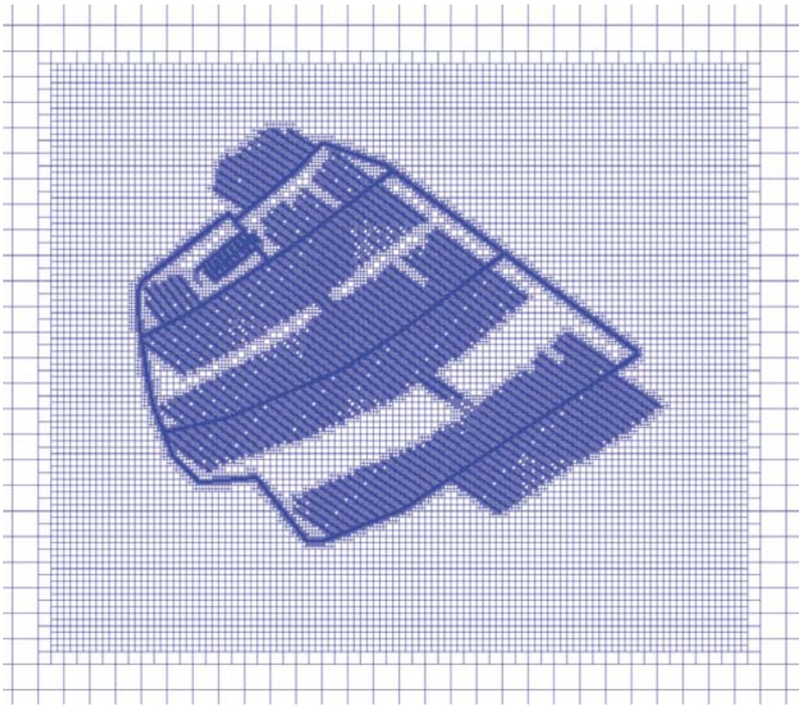

Figure 4-17. *Plane view of the computational grid at –465 m elevation. The discretisation around the repository was refined using an unstructured grid.*

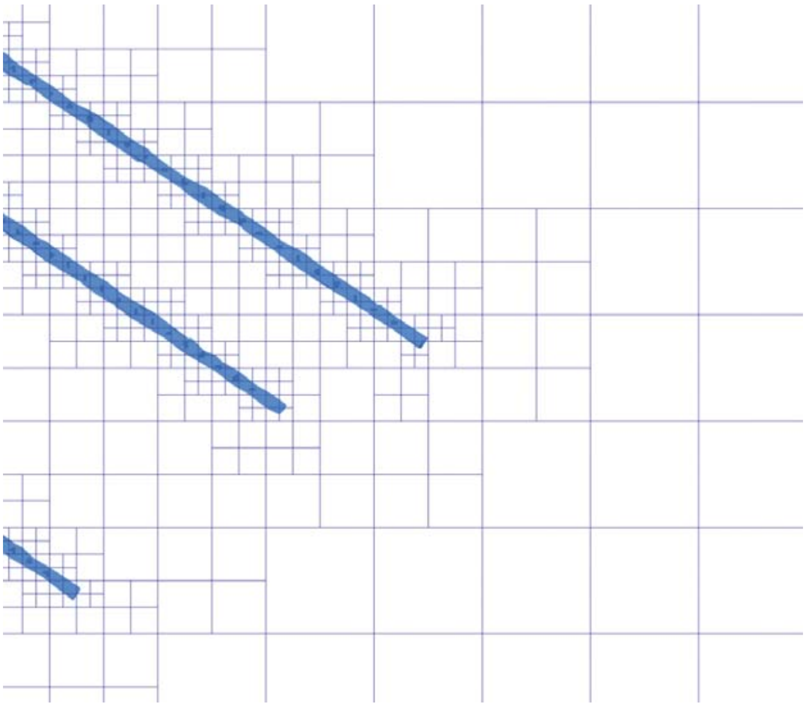

Figure 4-18. Enlargement showing the discretisation of the eastern corner of the repository. The size of the smallest grid cells was 4 m.

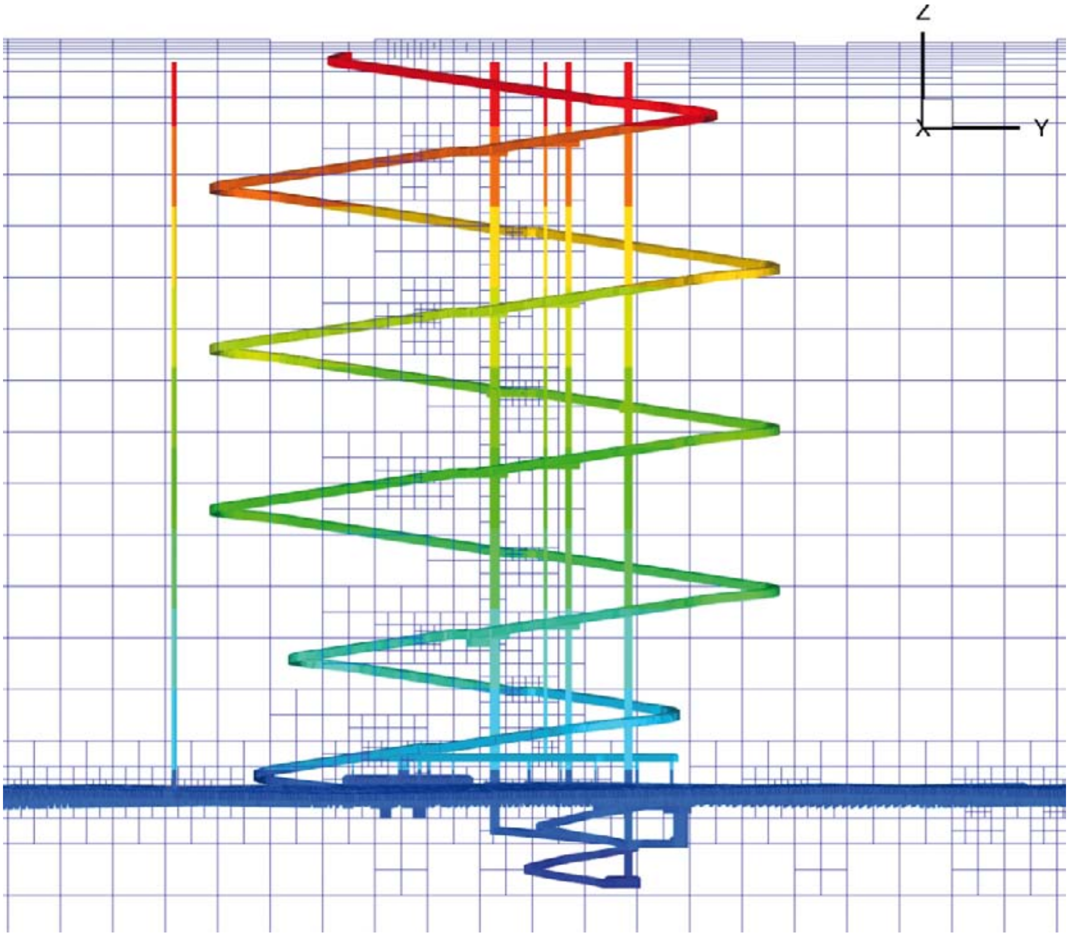

Figure 4-19. Vertical cross-section (South-North) through the simulated repository. The local x-coordinate for the cross-section is 5,020 m (cf Figure 2-18). The y-axis points towards north.

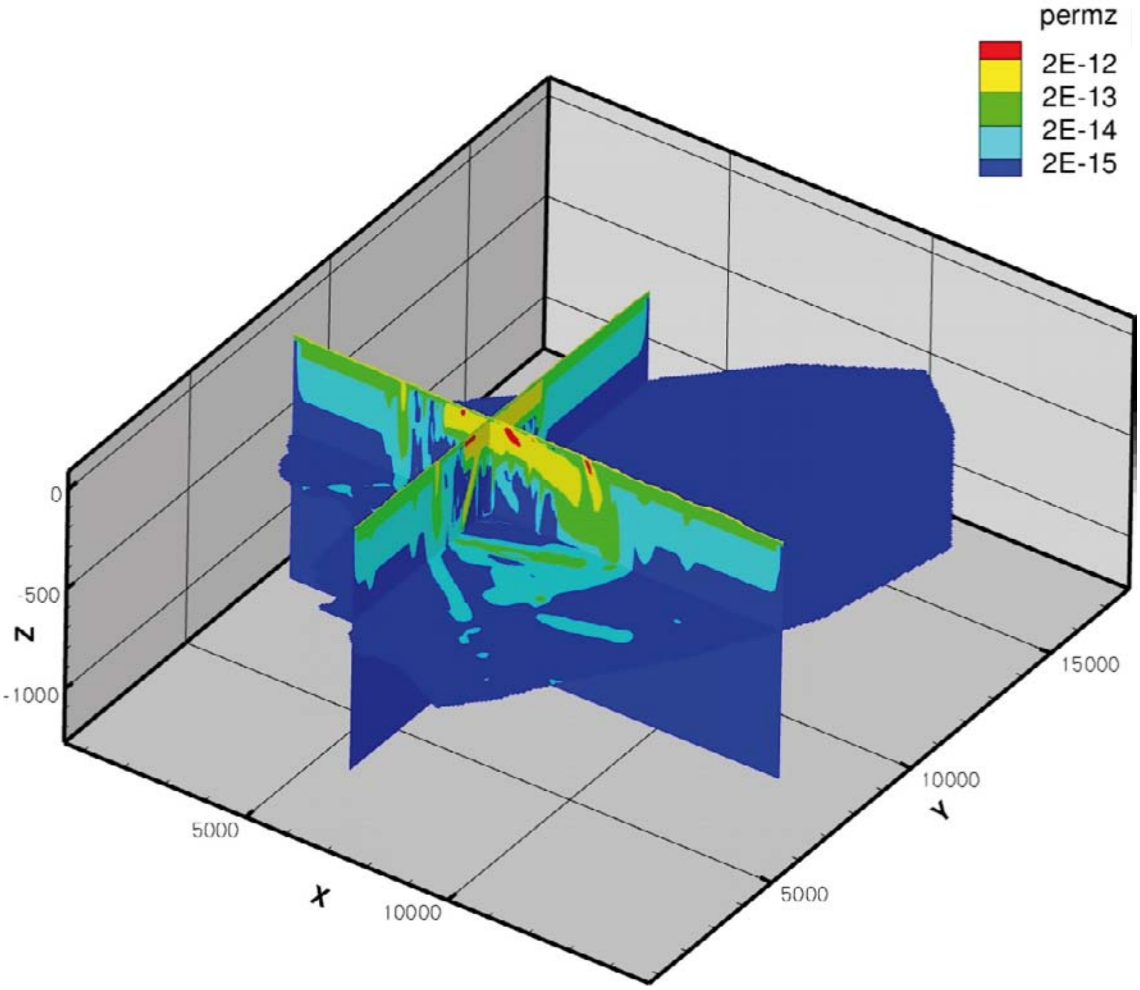

***Figure 4-20.** The vertical permeability field around the repository illustrated by two perpendicular vertical cross-sections and a horizontal plane at –465 m elevation.*

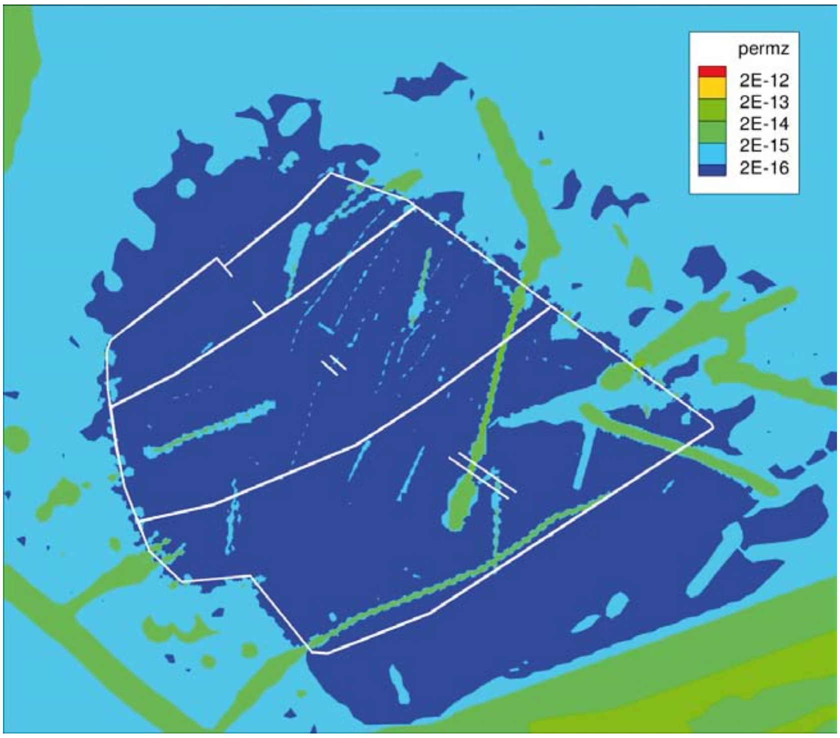

Figure 4-21. *Plane view of the grid cell vertical permeability field in the target area in the footwall at –465 m elevation. The white lines represent the main tunnels.*

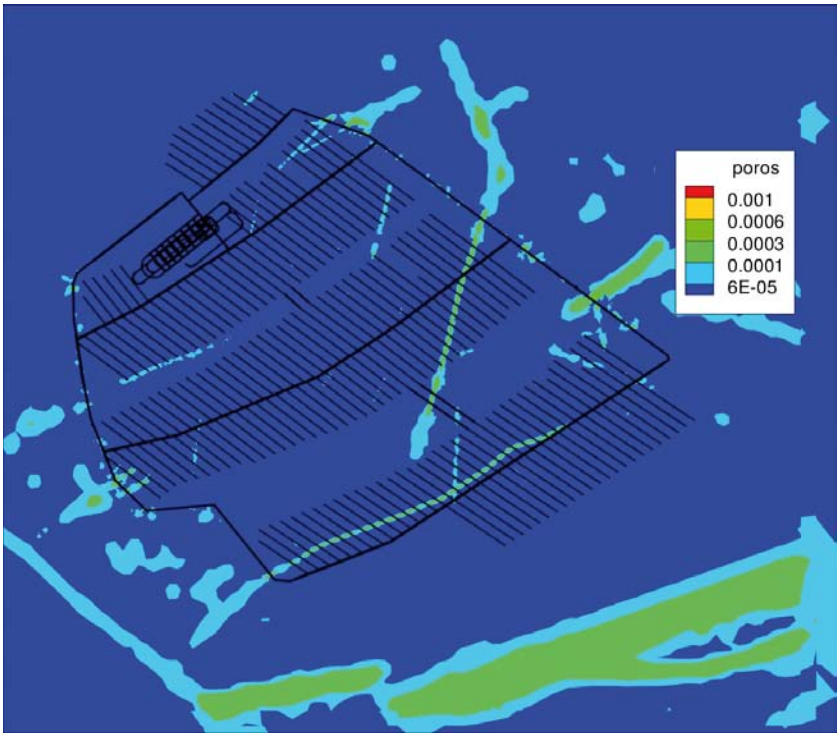

Figure 4-22. *Plane view of the grid cell kinematic porosity field in the target area in the footwall at –465 m elevation. The black lines represent the repository tunnels.*

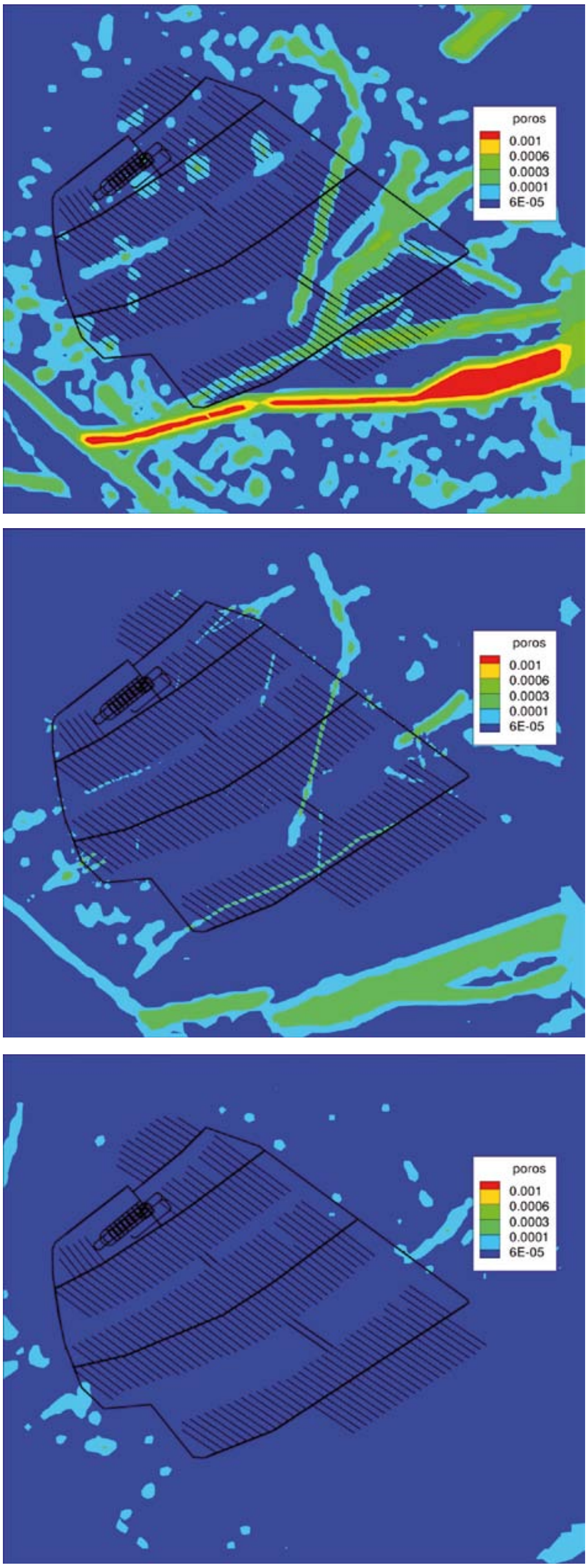

Elevation –300 m

Elevation
–465 m
(repository depth)

Elevation –600 m

Figure 4-23. *Horizontal close up views of the grid cell kinematic porosity at three elevations; –300 m, –465 m and –600 m. The repository layout is inserted in the views above and below repository depth (–465 m elevation) in order to facilitate the reading.*

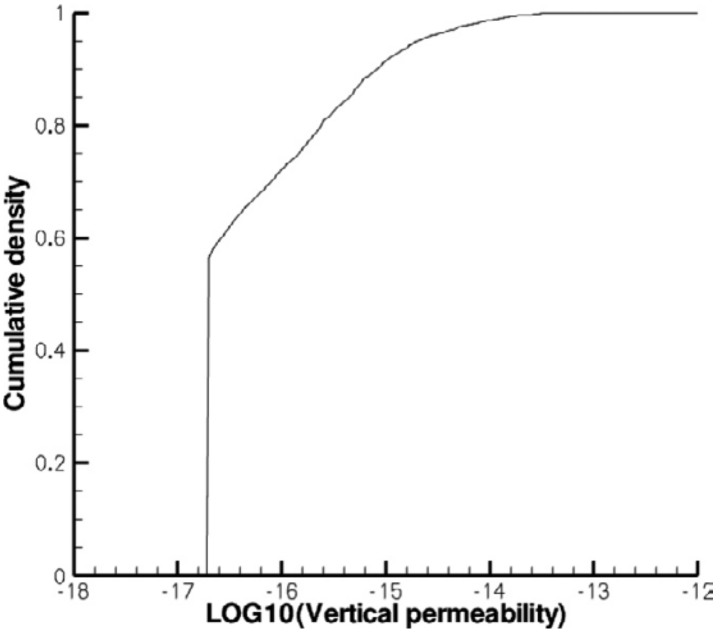

Figure 4-24. Cumulative density function plot of kc for all 4 m grid cells values within a subarea of (2 km)^2 centred on the view shown in Figure 4-21.

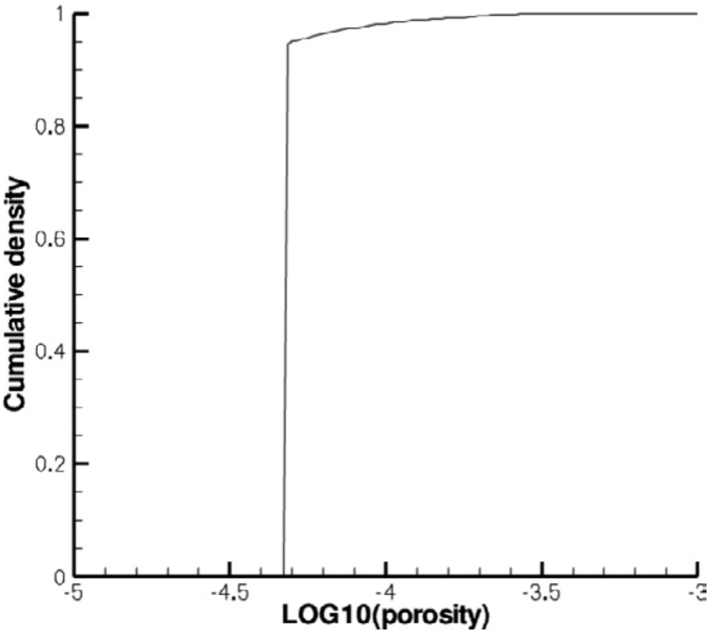

Figure 4-25. Cumulative density function plot of φc for all 4 m grid cells values within a subarea of (2 km)^2 centred on the view shown in Figure 4-22.

4.5 Scoping calculation of the total inflow rate

From the hydraulic data of the deformation zones and the fracture domains presented in Chapter 2 (see, e.g. Figure 2-4 and Figure 2-12), it is conceived that it is the structural-hydraulic properties of the bedrock nearest to the repository that governs the total inflow rate. Figure 2-9 illustrates the suggested hydrogeological model at Forsmark. (A close up view of the grid cell vertical permeability around the repository as for the base case groundwater flow realisation is shown in Figure 4-21.) Since the conductive fracture frequency at repository depth is very low and the fracture transmissivities are also low, the hydraulic conductivity of the bedrock is low as well. A simple mass balance calculation may be used to illustrate the situation at hand:

For a cross section area of 6 km^2, which roughly covers the horizontal extent of the repository layout, the total inflow rate to the repository is of the order of 30 L/s if the head change associated with a gauge pressure of zero in the tunnels takes place in the next 100 m of the repository and the vertical hydraulic conductivity of that interval is $1 \cdot 10^{-9}$ m/s (vertical permeability $2 \cdot 10^{-16}$ m/s). This flow rate value is of the same order of magnitude as the maximum possible flow rate, 25 L/s, associated with the net precipitation130 mm/y ($4.1 \cdot 10^{-9}$ m/s) over the same area.

This calculation suggests that the blueish area in Figure 4-21 is probably not a problem with regard to inflow. However, there will be local differences in the inflow rate due to heterogeneity in the structural-hydraulic properties. In particular, the grouting efficiency of intersecting deformation zones will determine the magnitude of the total inflow rate. Likewise, effects on the groundwater chemistry at depth, if any, are likely to coincide where poorly grouted deformation zones intersect the repository tunnels. Effects on the groundwater table above a repository at Forsmark, if any, are likely to occur where such deformation zones outcrop, i.e. as envisaged in /Axelsson and Follin 2000/.

4.6 Advective travel time

The grid cell hydraulic conductivity and kinematic porosity are both important for the transport simulation of dissolved solids, i.e. the salinity (C). They are also important for the advective travel time (t_w) of non-reactive and non-sorbing particles simulated by means of particle tracking. For a one-dimensional, homogeneous conduit of length L [L] that is subjected to a constant hydraulic head gradient J_L [-], the advective travel time for a non-reactive and non-sorbing particle can be estimated from Darcy's law:

$$t_{w,L} = \frac{\phi_L \, L}{K_L \, J_L} \tag{4-1}$$

where K_L and ϕ_L are the hydraulic conductivity and kinematic porosity of the one-dimensional, homogeneous conduit. The CDF plot shown in Figure 4-24 reveals that the ratio of the maximum value to the minimum value of the permeability (or hydraulic conductivity) in proximity of the repository in Figure 4-21 is about 7,500 for a 4 m grid size. In contrast, Figure 4-25 reveals that the corresponding ratio of the kinematic porosity in Figure 4-22 is much smaller, about 20. This comparison suggests a greater significance of the heterogeneity in the permeability for the spread in the advective travel time. However, regardless of the value of the hydraulic conductivity, the advective travel time will always be fairly low due to the narrow range of low values of the kinematic porosity.

The analogy with a one-dimensional, homogeneous conduit may be considered quite arbitrary for a three-dimensional flow problem characterised by great heterogeneity. Notwithstanding, for the sake of understanding the output from DarcyTools, the impact of the parameter specification shown in Table 4-1 and Table 4-4 on the advective travel time is examined below. In particular, the cross correlation between the grid cell hydraulic conductivity and the grid cell kinematic porosity suggested by Equation (3-15) is examined.

Inserting Equation (3-15) in Equation (3-18) renders:

$$(t_w)_f = \frac{(\phi_c)_f \, L_f}{(K_c)_f \, J_f} = \frac{(e_t)_f \, L_f}{T_f \, J_f} \tag{4-2}$$

That is, if one assumes a homogeneous fracture that connects repository depth to ground surface, the advective travel time through the fracture depends on the fracture transmissivity, the fracture length, the hydraulic head gradient and the assumed relationship between fracture aperture and fracture transmissivity.

For an open repository, the vertical hydraulic gradient in a homogeneous fracture that connects repository depth to ground surface is 100% if the flow path length is of the same order as the fracture length. The structural-hydraulic properties of the discrete features behind the base case realisation imported from the temperate modelling work conducted by /Joyce et al. 2010/ were based on a semi correlated transmissivity model, cf Equation (3-17) and Table 2-3. For a fracture of length of 465 m and parameter values as specified in Table 2-3, the fracture transmissivity becomes $2.8 \cdot 10^{-8}$ m^2/s, the kinematic porosity $3.3 \cdot 10^{-4}$ and the advective travel time about three months. It is debatable if fractures of this size are homogeneous, but this calculation is according to the modelling methodology.

The minimum values of the hydraulic conductivity and the kinematic porosity specified for depths greater than 20 m in DarcyTools are shown in Table 4-1. Ideally, these values should be representative for intact rock, i.e. a crystalline matrix without fractures. However, realistically low values of the matrix permeability are not possible to use in this work due to computational constraints. Hydraulic tests on intact rock cores from Forsmark reveal matrix permeabilities that are about three orders of magnitude lower than the minimum value shown in Table 4-1 /Vilks 2007, Follin et al. 2007a/. In conclusion, the minimum values shown in Table 4-1 render a one-dimensional advective travel time of about seven years. Laboratory tests suggest that a more realistic value for the intact rock is of the order of 7,000 years, i.e. a time scale that is of the same order of magnitude as rock matrix diffusion.

Figure 4-26 shows a scatter plot of the kinematic porosity data and the vertical permeability data shown in Figure 4-24 and Figure 4-25. The degree of correlation varies considerably for the semi-correlated transmissivity model, but the range in the spread in the kinematic porosity decreases with increasing vertical permeability.

Figure 4-27 shows a summary plot made for the sake of an improved understanding of the advective travel time output presented in section 5.3. The advective travel times shown in Figure 4-27 are based on a hydraulic head gradient of 100% and a flow path length of 465 m. (The relation between hydraulic conductivity and permeability is given by Equation (3-4). Typically, the magnitude of *K* is seven orders of magnitude greater than the magnitude of *k*.).

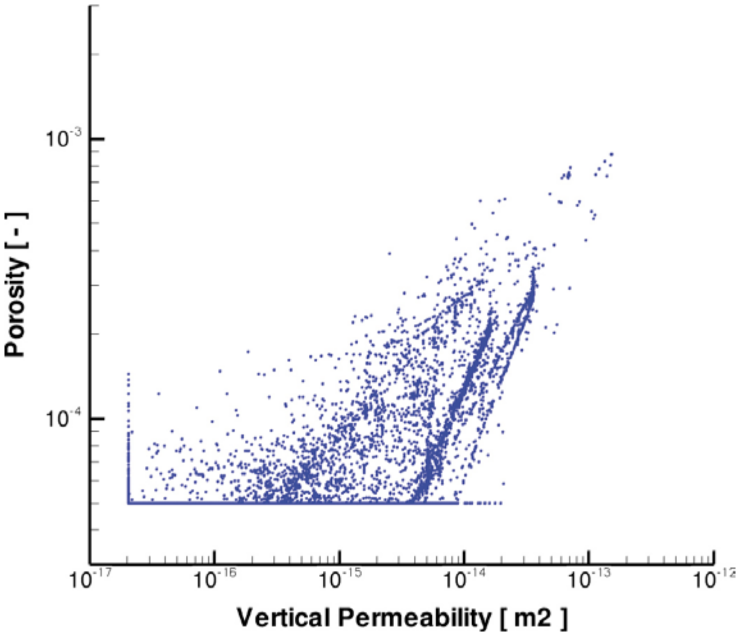

Figure 4-26. *Scatter plot of the kinematic porosity data and the vertical permeability data shown in Figure 4-24 and Figure 4-25.*

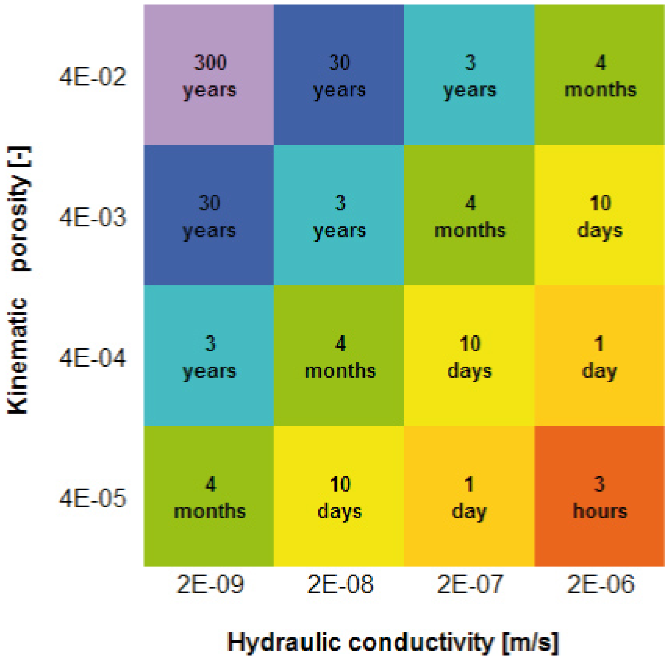

	2E-09	2E-08	2E-07	2E-06
4E-02	300 years	30 years	3 years	4 months
4E-03	30 years	3 years	4 months	10 days
4E-04	3 years	4 months	10 days	1 day
4E-05	4 months	10 days	1 day	3 hours

Figure 4-27. *Summary plot made for the sake of an improved understanding the advective travel time output presented in section 5.3. The advective travel times in this plot are based on a hydraulic head gradient of 100% and a flow path length of 465 m.*

5 Results

5.1 Comparison with natural conditions

Present-day lakes and wetlands, surface water (stream) runoff, and groundwater chemistry are loosely used as "calibration targets" for the modelled evolution of the hydrological and hydrochemical conditions during Holocene time (Figure 4-6, Figure 4-7 and Figure 4-8). For the sake of the work reported here, the surface topography is resolved by a cell size of 64 m and potential streams of all dimensions by a cell size of 32 m (Figure 5-1).

Figure 5-2 shows the simulated saturation level close to ground surface at present day. Areas with a predicted groundwater table (hydraulic head) above ground surface are marked blue, whereas areas with a predicted groundwater table below, but very close, ground surface are marked green. The latter may be perceived as wetlands, cf Figure 4-7. Figure 5-3 shows the simulated annual mean stream runoff rates for two of the modelled streams shown in Figure 5-1. The agreements of these comparisons are considered acceptable for the sake of the work reported here.

Figure 5-4 shows the simulated salinities at 2000 AD in per cent by weight at –465 m elevation. The area in Figure 5-4 centred on x = 5,500 m and y = 6,500 m coincides with the target volume in the footwall (Figure 2-6, Figure 2-7 and Figure 2-8), which is suggested as host rock for a final repository at Forsmark (Figure 4-16). The simulated salinity in the target volume is somewhat less than 1%. As a comparison, Figure 5-5 shows the measured concentrations of Total Dissolved Solids (TDS) in seven cored boreholes at Forsmark. According to Figure 5-5, the simulated salinity at repository depth corresponds well to the measured concentration of TDS.

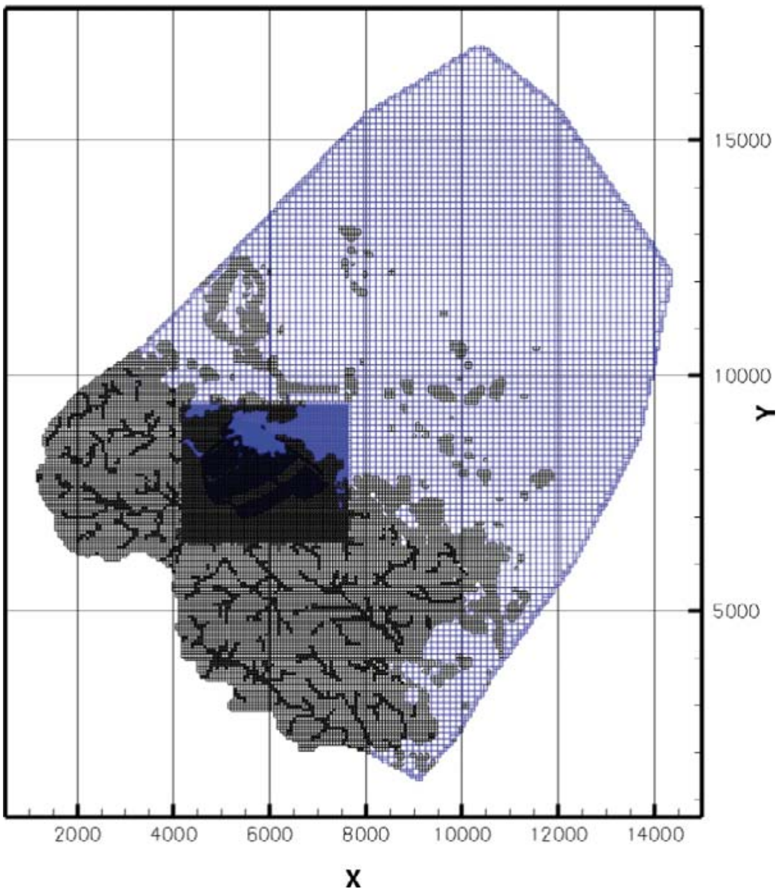

Figure 5-1. The surface topography is resolved by a cell size of 64 m and potential streams by a cell size of 32 m.The latter are indicated as black lines. The "stream cells" are assigned a hydraulic conductivity of 0.2 m/s. (It is noted that Figure 4-7 shows major streams only.)

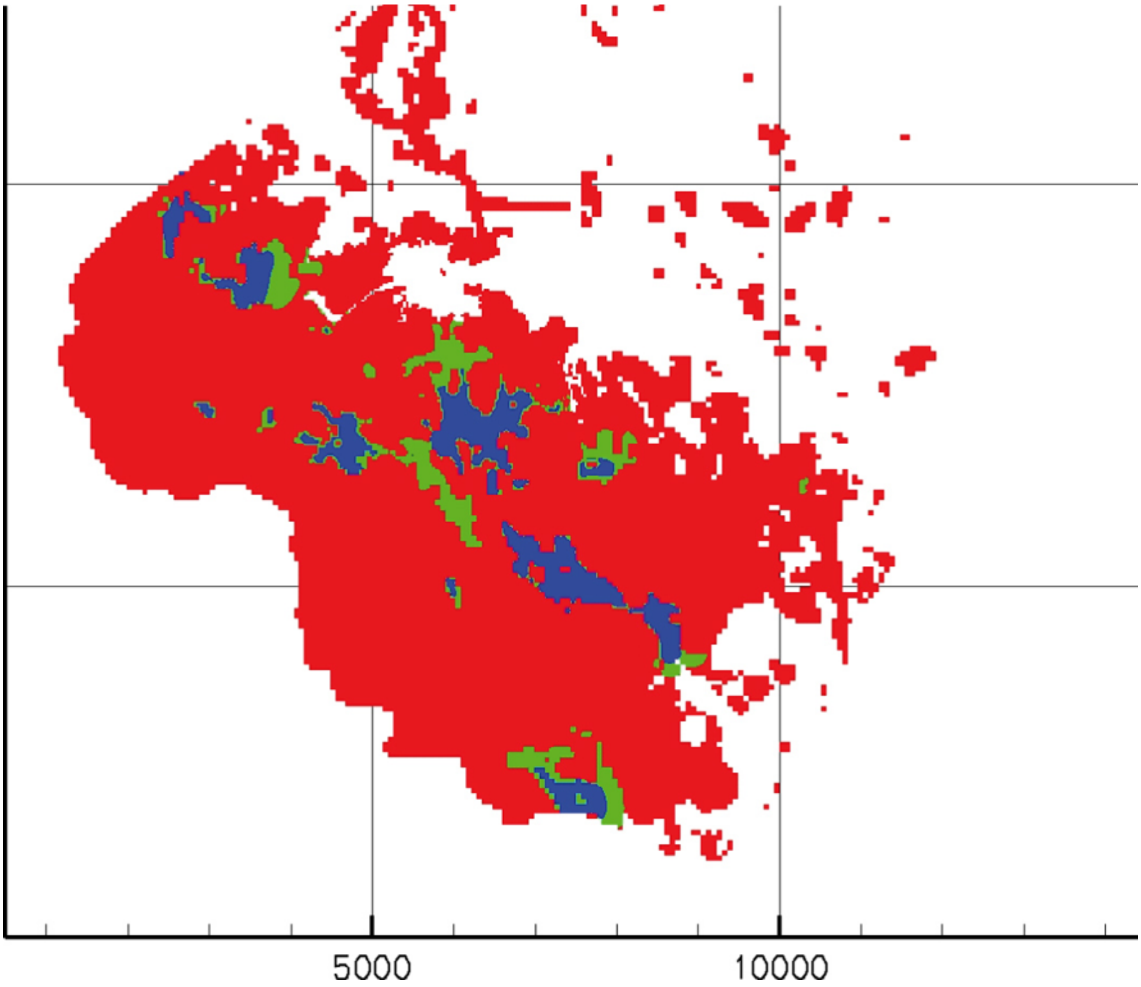

Figure 5-2. *Areas with a predicted groundwater table (hydraulic head) above ground surface are marked blue, whereas areas with a predicted groundwater table below, but very close, ground surface are marked green. The latter may be perceived as wetlands, cf Figure 4-7. In the red areas the groundwater table is significantly below the ground surface.*

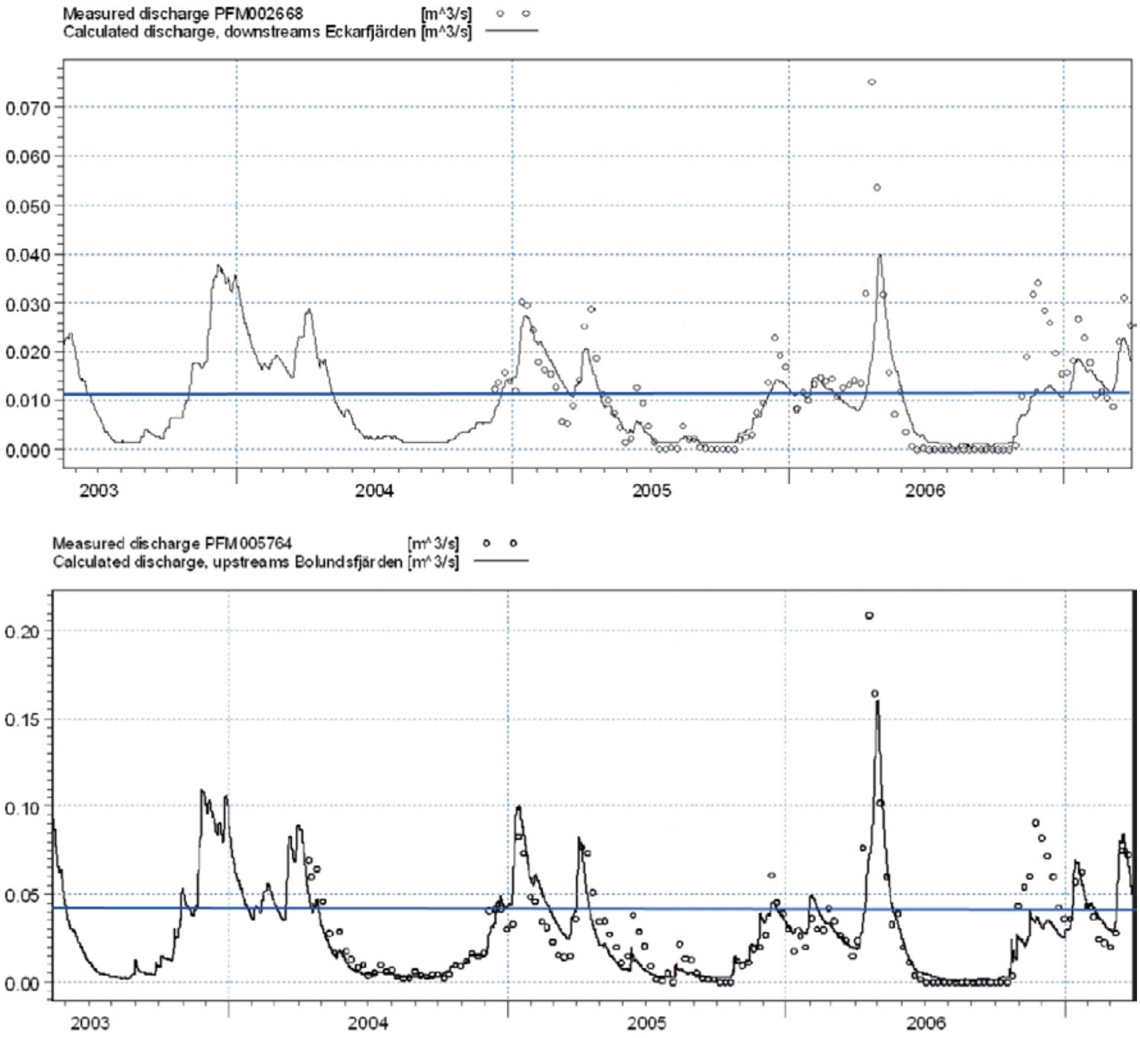

Figure 5-3. *Simulated annual mean stream runoff rates (blue lines) and measured weekly (open circles) stream runoff rates from Lake Eckarfjärden (top) and Lake Bolundsfjärden (bottom). The black lines show the simulated diurnal stream runoff rates in the SDM work using the MIKE SHE code (cf Figure 4-8). The simulated annual mean stream runoff rates, 0.011 m^3/s and 0.042 m^3/s, respectively, are based on an annual net precipitation of 130 mm/y /Bosson et al. 2008/.*

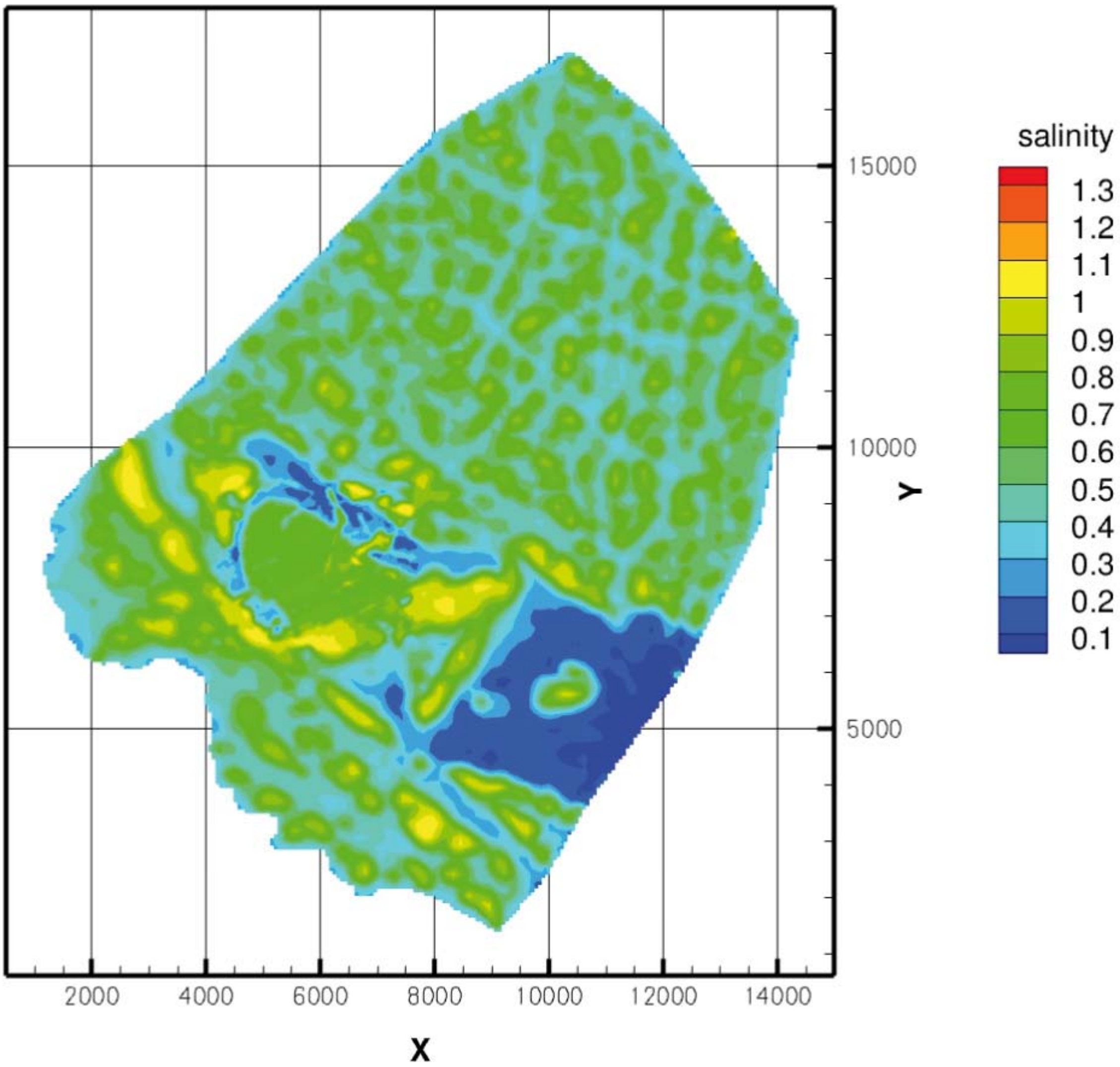

***Figure 5-4.** Simulated salinities 2000 AD in per cent by weight at –465 m elevation. A salinity of 0.1% by weight corresponds approximately to 1 g/L of TDS, cf Equation (3-7).*

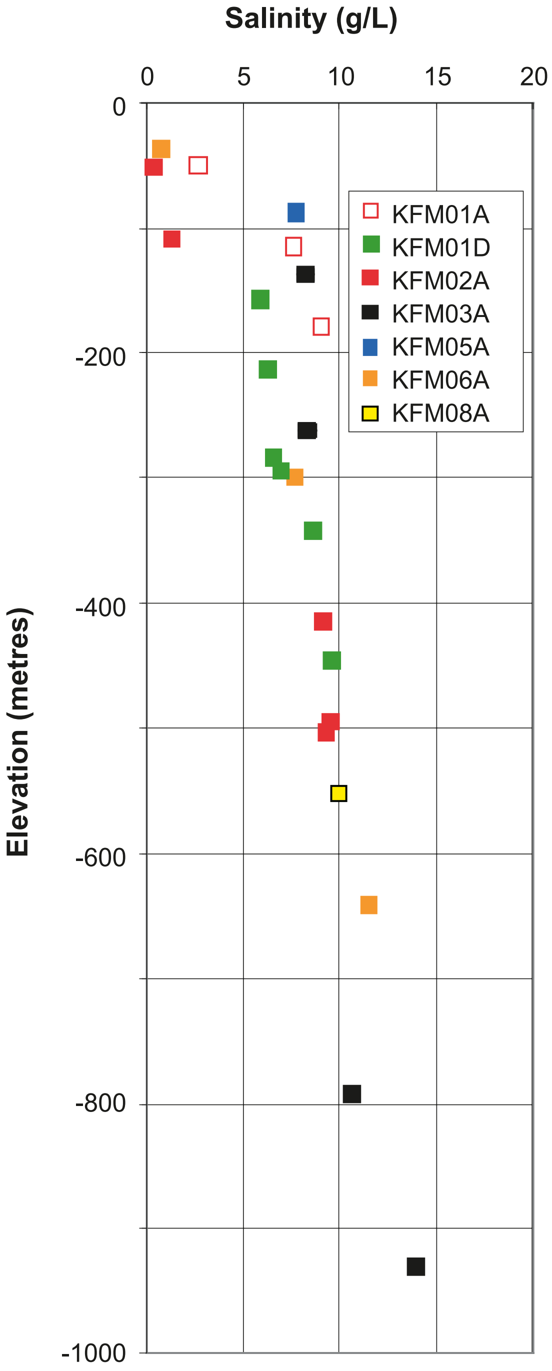

***Figure 5-5.** Measured concentration of total dissolved solids (TDS) versus depth for seven cored boreholes at Forsmark. 10 g/L of TDS corresponds approximately to a salinity of 1% by weight, cf Equation (3-7). (Modified after Figure 4-9 in /Follin 2008/.)*

5.2 Grouting efficiency

5.2.1 Inflow calculations

The inflow simulations during the excavation and operational phases are done for three operation stages A–C (Figure 1-2) and three levels of grouting efficiency I–III (Table 4-3). Table 5-1 summarises the calculated inflows to the different parts of a repository at Forsmark. The total inflow varied in the range 7 to 52 L/s (600 to 4,600 m^3/d), depending on which stage and level of grouting efficiency that is considered.

The three operation stages are run in sequence, where the first stage, A, lasted for 15 years, the second stage, B, lasted for 15 years and the third stage, C, lasted for 20 years, corresponding to a total operational time of 50 years. Figure 5-6 through Figure 5-9 represent operation stage C, i.e. the last one of the three operation stages. Operation stage C rendered the largest inflows. For the sake of visualisation, cells in contact with the repository walls are marked up with spheres in Figure 5-6 through Figure 5-9 if the inflow exceeded two specified thresholds, 0.1 and 0.5 L/min.

There are two observations in Figure 5-6 through that need to be commented upon:

- The ramp seems to have concentrated inflows in its upper part. A part of the simulated inflows to the ramp may be associated with the intersection with the modelled sheet joints (Figure 5-9).
- Large inflows at repository depth during operation stage C are predominantly encountered at the boundaries. This can be explained by the pressure distribution, see Figure 5-10. A large inflow requires both a great permeability (Figure 4-21) and a significant pressure gradient. It is clear from Figure 5-10 that the pressure gradients in the interior of an open deposition area (operation stage C in this example) will be fairly uniform, whereas high gradients are to be expected at the boundaries.

Table 5-1. Calculated inflow rates (L/s) to different parts of a final repository at Forsmark for three levels of grouting efficiency, I–III, and three stages of operation, A–C. The three operation stages are run in sequence, where stage A lasted for 15 years, stage B lasted for 15 years and stage C lasted for 20 years. CA = central area, DA = deposition area, MT = transport and main tunnels, VS = ventilation shaft.

Part of repository	Grouting level I Operation stage			Grouting level II Operation stage			Grouting level III Operation stage		
	A	B	C	A	B	C	A	B	C
CA	4	4	5	2	2	2	1	1	1
	0	0	0	0	0	0	0	0	0
	3	3	3	1	1	1	1	1	1
	0	0	0	0	0	0	0	0	0
DA-A	6	–	–	4	–	–	3	–	–
DA-B	–	8	–	–	6	–	–	3	–
DA-C	–	–	9	–	–	8	–	–	4
RAMP	16	17	17	6	6	6	2	2	2
MT-A	6	6	7	4	4	5	2	2	2
MT-B	–	1	1	–	1	1	–	0	0
MT-C	–	–	9	–	–	5	–	–	2
VS1	1	1	1	1	1	0	0	0	0
VS2	–	2	2	–	1	1	–	0	0
Total	**33**	**39**	**51**	**17**	**21**	**28**	**8**	**8**	**11**

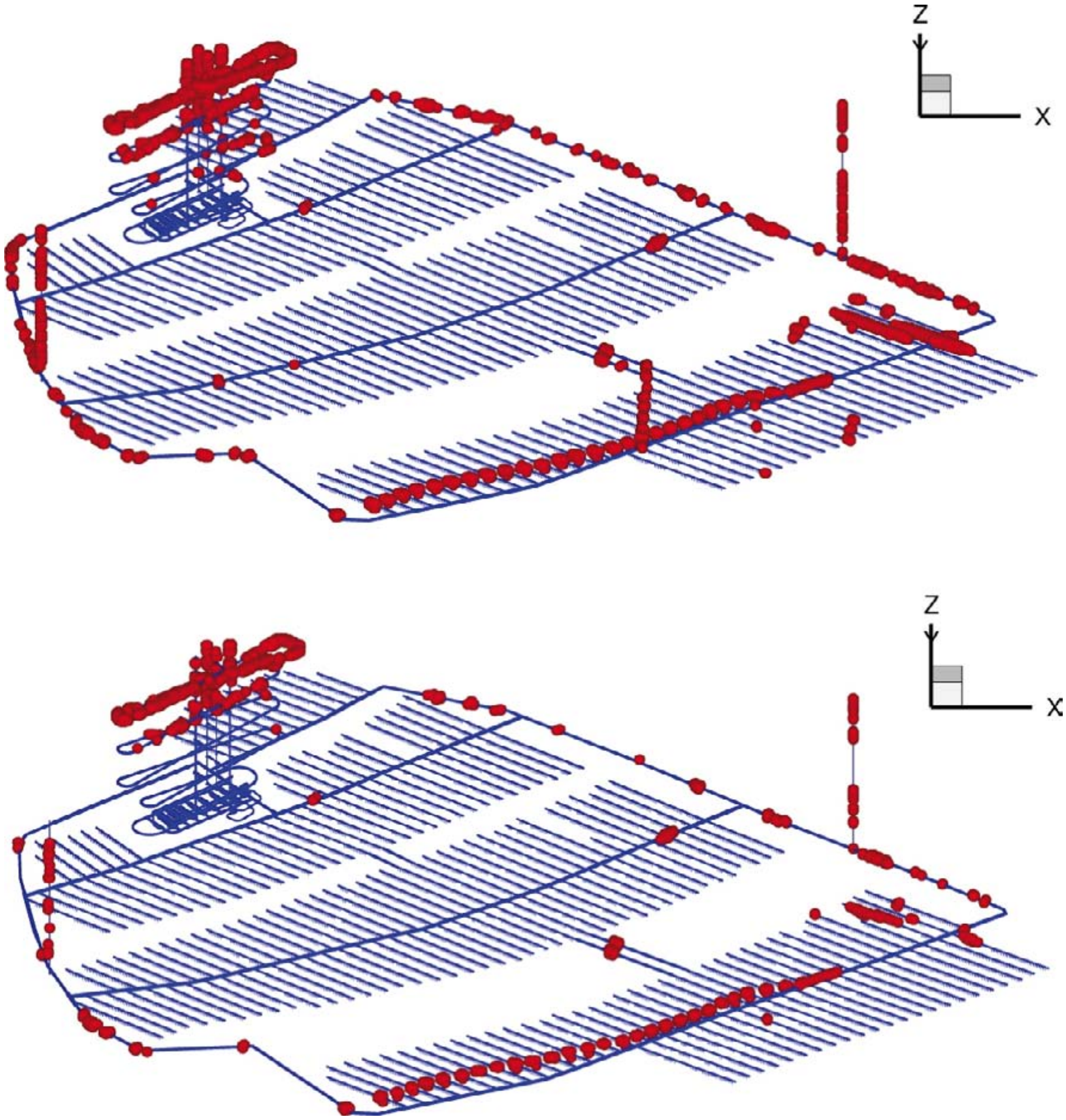

Figure 5-6. *Cells with an inflow rate greater than 0.1 L/min (top) and 0.5 L/min (bottom) are marked up by spheres. Operation stage C and grouting level I.*

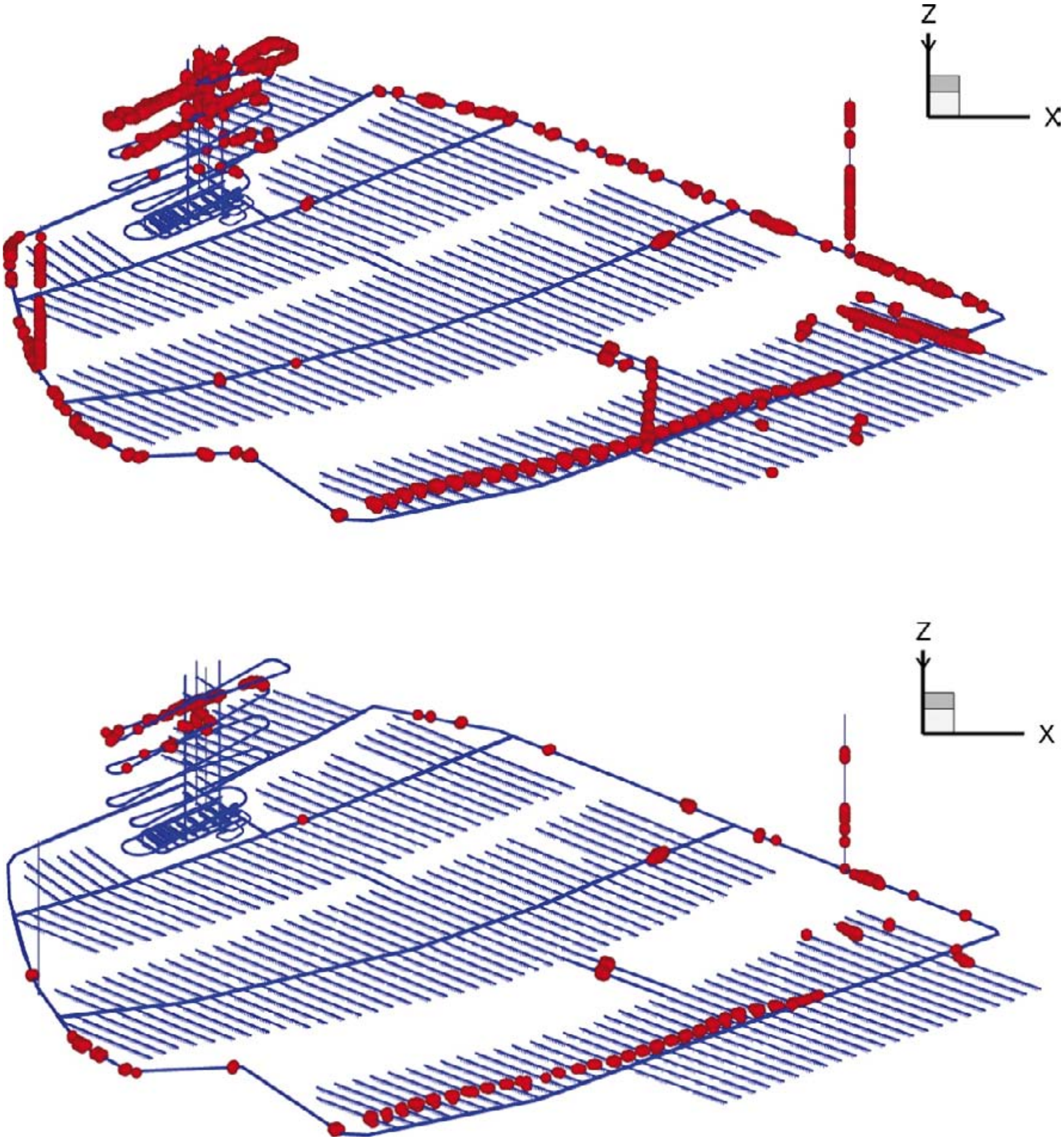

Figure 5-7. Cells with an inflow rate greater than 0.1 L/min (top) and 0.5 L/min (bottom) are marked up by spheres. Operation stage C and grouting level II.

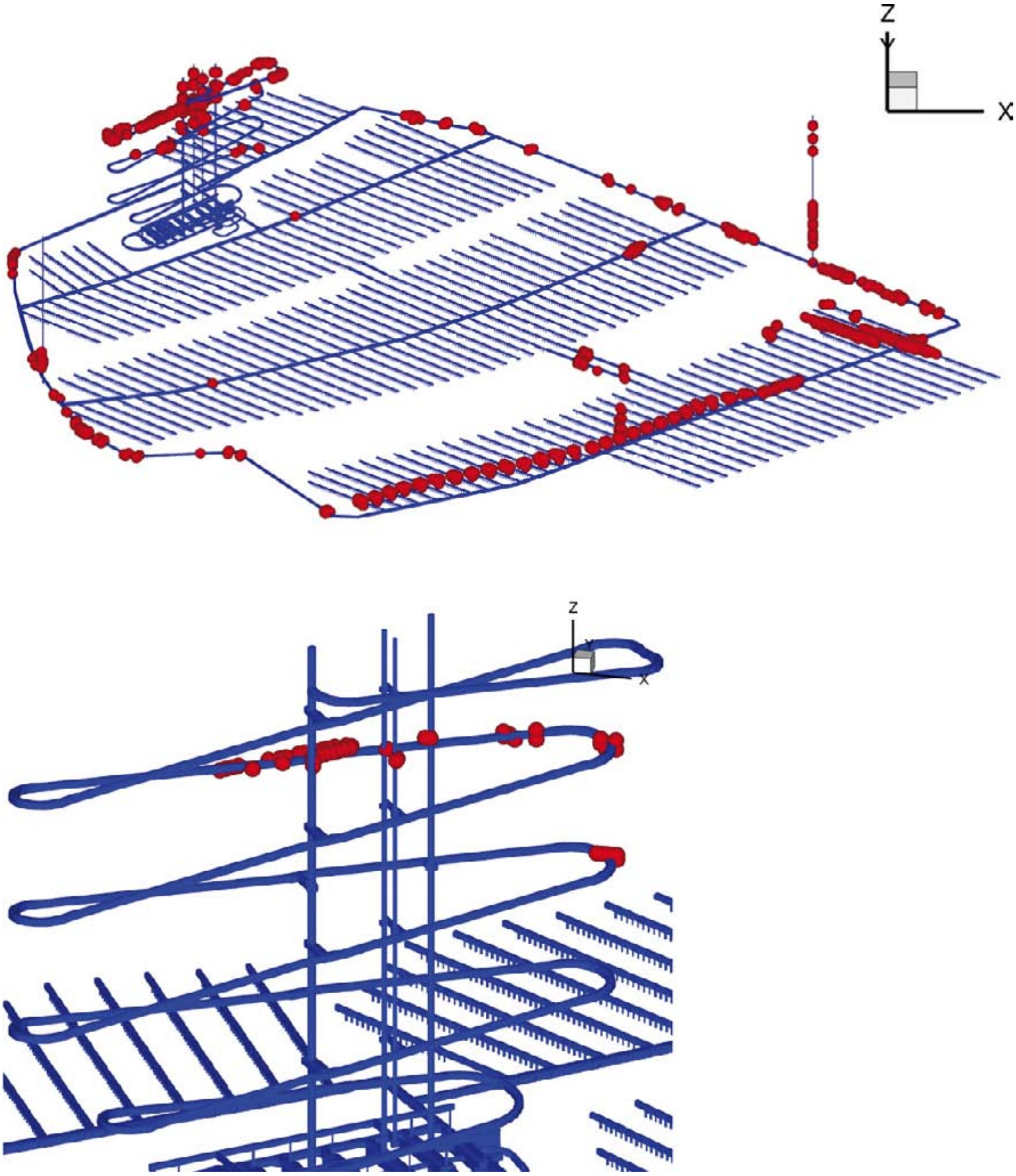

Figure 5-8. *Cells with an inflow rate greater than 0.1 L/min (top) and 0.5 L/min (bottom) are marked up by spheres. Operation stage C and grouting level III. Note that for this level of grouting efficiency all inflows greater than 0.5 L/min are in the ramp. Some of the high inflows in the ramp can be associated with the modelled sheet joints (Figure 5-9).*

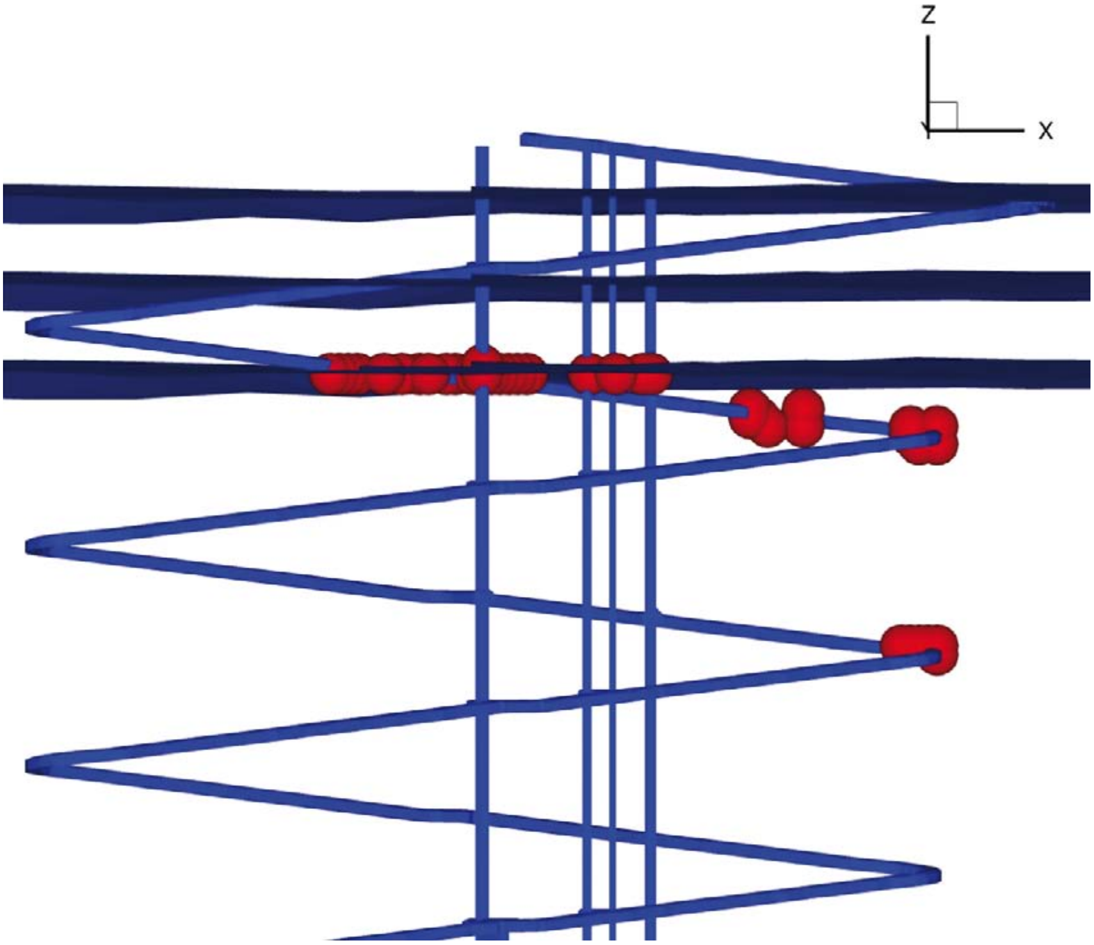

Figure 5-9. Calculated inflows to the ramp greater than 0.5 L/min for operation stage C and grouting level III. Some of the high inflows in the ramp can be associated with the modelled sheet joints. The x-axis points towards East.

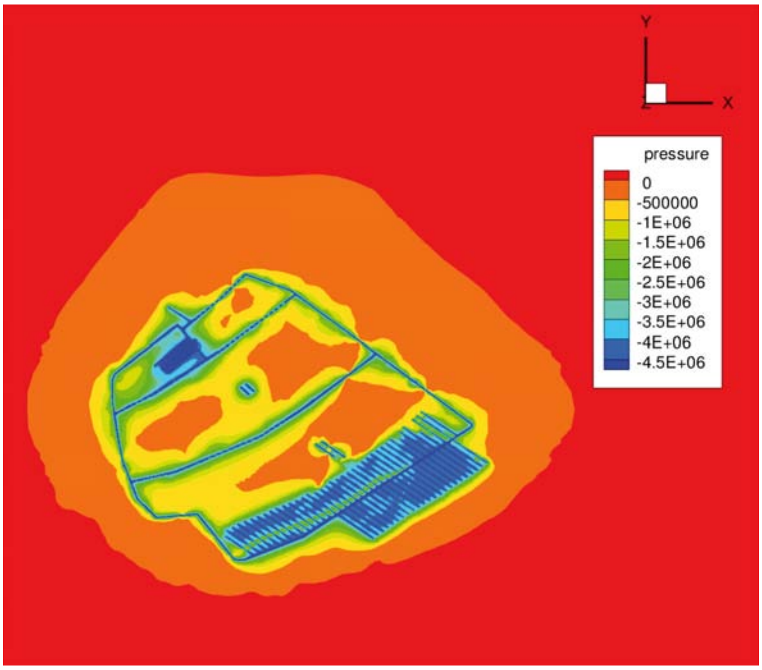

Figure 5-10. Residual pressure distribution (Pa) around a final repository at –465 m elevation. Operation stage C and grouting level III. (The definition of the residual pressure is shown in Equation (3-3).) The y-axis points towards North.

5.2.2 Drawdown of the groundwater table

The simulated drawdown of the groundwater table associated with the three levels of grouting efficiency, I–III, is shown in Figure 5-11. Only the drawdown for operation stage C is shown here. Stage C is the last stage and generates the largest inflows.

A drawdown of the groundwater table implies that shallow fresh and/or brackish water is transported towards the repository. The simulated drawdown is moderate though, in particular for grouting levels II and III. The largest drawdown is encountered in the proximity of the ramp. The chemical changes around the repository as a result of the drawdown are discussed in section 5.2.3.

5.2.3 Changes in the groundwater composition

The effect of the drawdown on the salinity distribution at repository depth for grouting level II and operation stage C is shown in Figure 5-12. Figure 5-12 suggests that deep saline water from below is transported towards the repository where the shaft and ramp are located mainly, whereas the groundwater composition at the other parts of the layout appear to be more diluted, i.e. influenced by the less saline groundwater that exist above the repository. The simulated changes in the chemical conditions suggest that this interpretation may be overly simplistic, however. The two uppermost images shown in Figure 5-13 represent the simulated conditions at –300 m elevation. These images suggest that water with a higher salinity than the initial water composition at this elevation may also infiltrate into the bedrock during the excavation and operational phases. The source for such water is most likely the brackish Baltic Sea, and the plausible structures that can provide such flows are the encountered sheet joints. In the model, these extend all the way from the Singö deformation zone, under Asphällsfjärden and across the target area where the repository is located, see Figure 4-3.

5.3 Flow paths and travel times to an open repository

It is of interest to investigate the advective flow paths and travel times to the modelled repository. The flow paths indicate the location of potential recharge areas and the travel times can be used in hydrochemical calculations. For the sake of the work reported here, we used the modified base case described in section 4.3, i.e. all parts of the repository layout are held open and had a grouting efficiency corresponding to level II.

The flow paths from the recharge areas carrying water to the open repository were identified by means of reversed particle tracking. That is, particles were released at repository depth and traced in a reversed flow field. The total simulation time was ten years and the time step was ten days.

The starting positions for the released particles are all cells in contact with the repository below −440 m elevation with an inflow rate greater than 0.1 L/min. In total 2,850 inflow points fulfilled this criterion. Figure 5-14 shows traces of 100 randomly selected particles. The body of these particles recharge right above the repository.

The advective travel times for the 2,850 inflow points are shown as a cumulative density function curve in Figure 5-15. The mass recovery was 100% and the median of the advective travel times from ground surface to an open repository is of the order of one year. This value is very low and suggests high advective transport velocities close to the repository. It is noted that the advective travel time computations are uncertain since the specified values of the grid cell hydraulic properties are affected by uncertainty in the definition of the grid cell kinematic porosity, see Section 4.6.

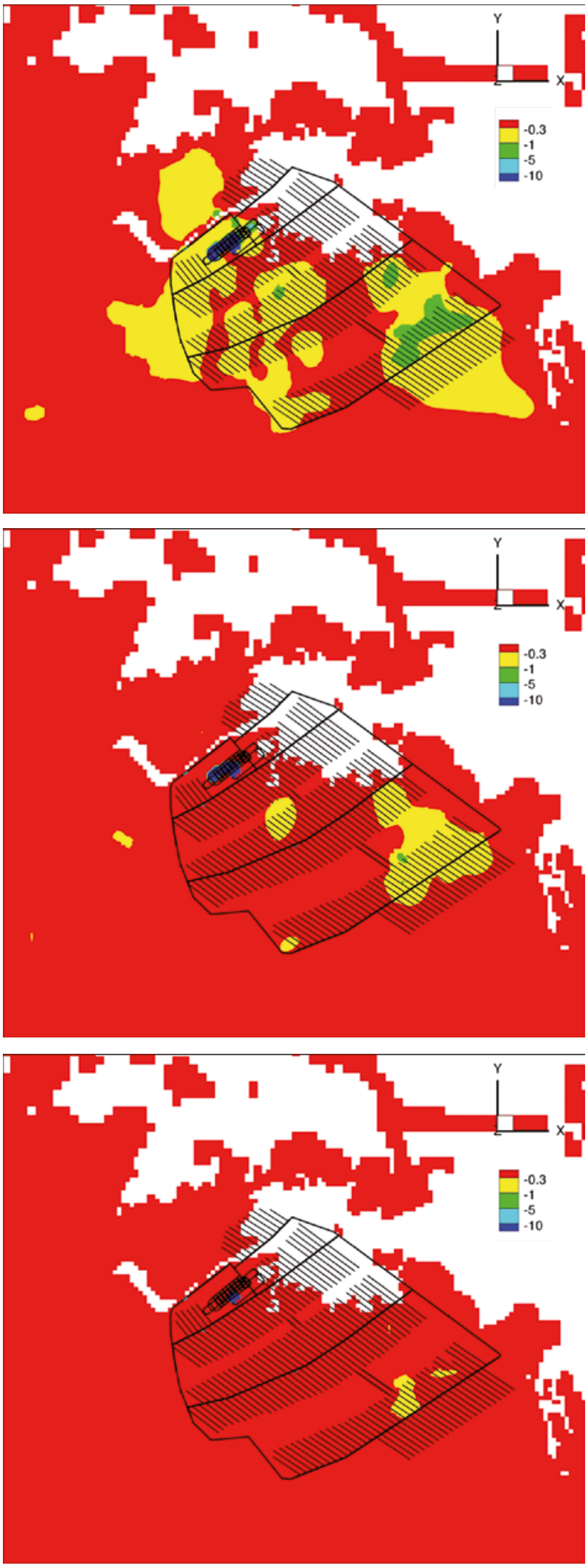

Operation
stage C
Grouting
level I

Operation
stage C
Grouting
level II

Operation
stage C
Grouting
level III

***Figure 5-11.** Simulated drawdown of the groundwater table at the end of operation stage C for three different levels of grouting efficiency, I–III. The values shown in the legend are expressed in metres. The y-axis points towards North.*

Elevation
–465 m
Pre-repository
conditions

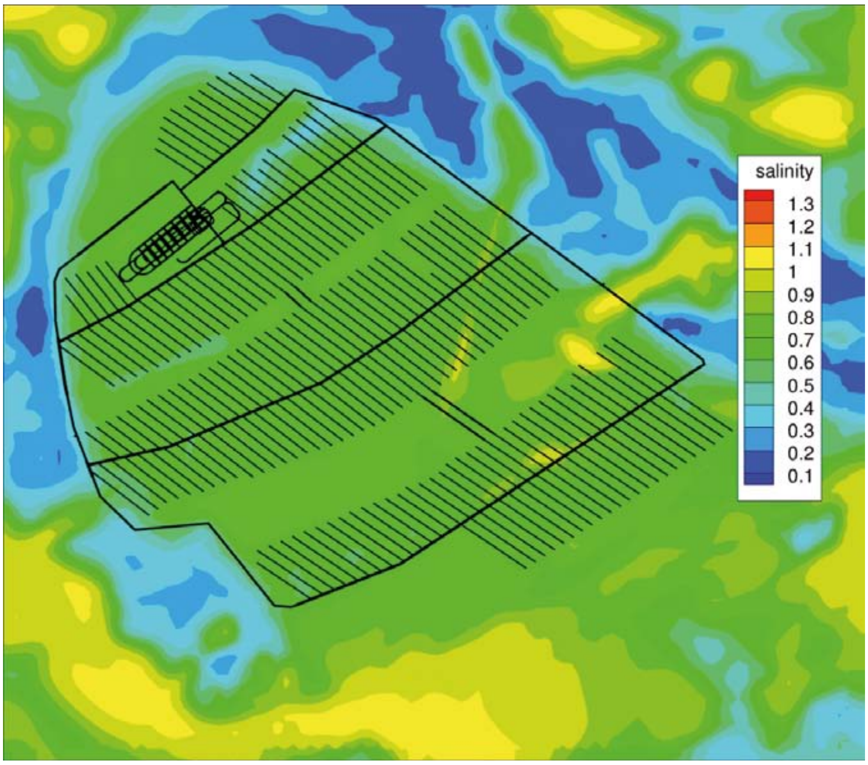

Elevation –465 m
Conditionsat the end
of Operation stage C
Grouting level **II**

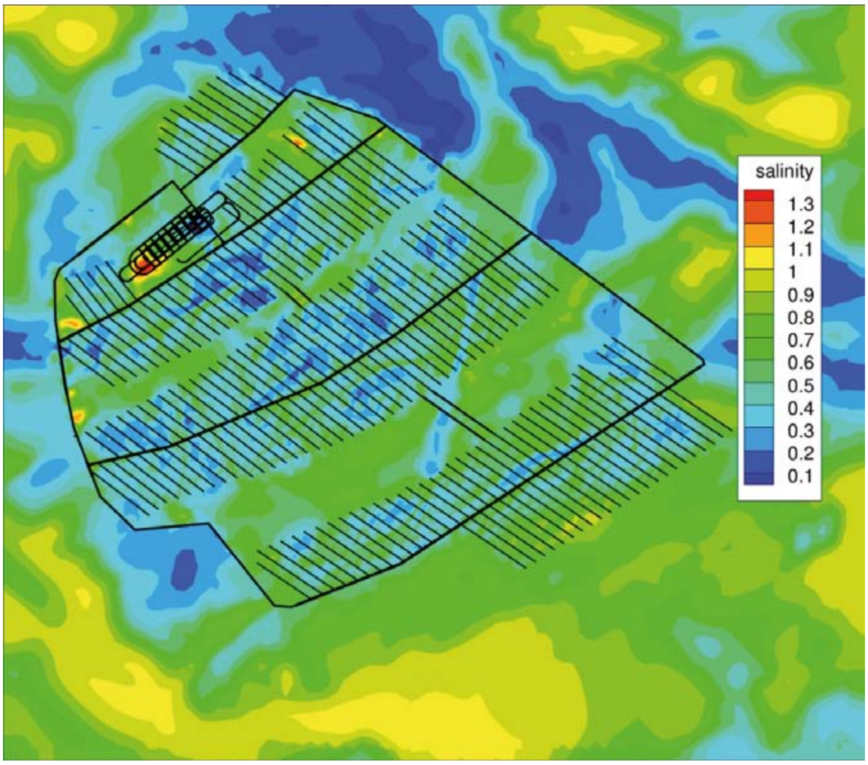

Figure 5-12. *Simulated salinity at –465 m elevation. Top: Pre-repository conditions (cf Figure 5-4). Bottom: Conditions at the end of operation stage C for grouting level II. The values shown in the legend are expressed in percent by weight.*

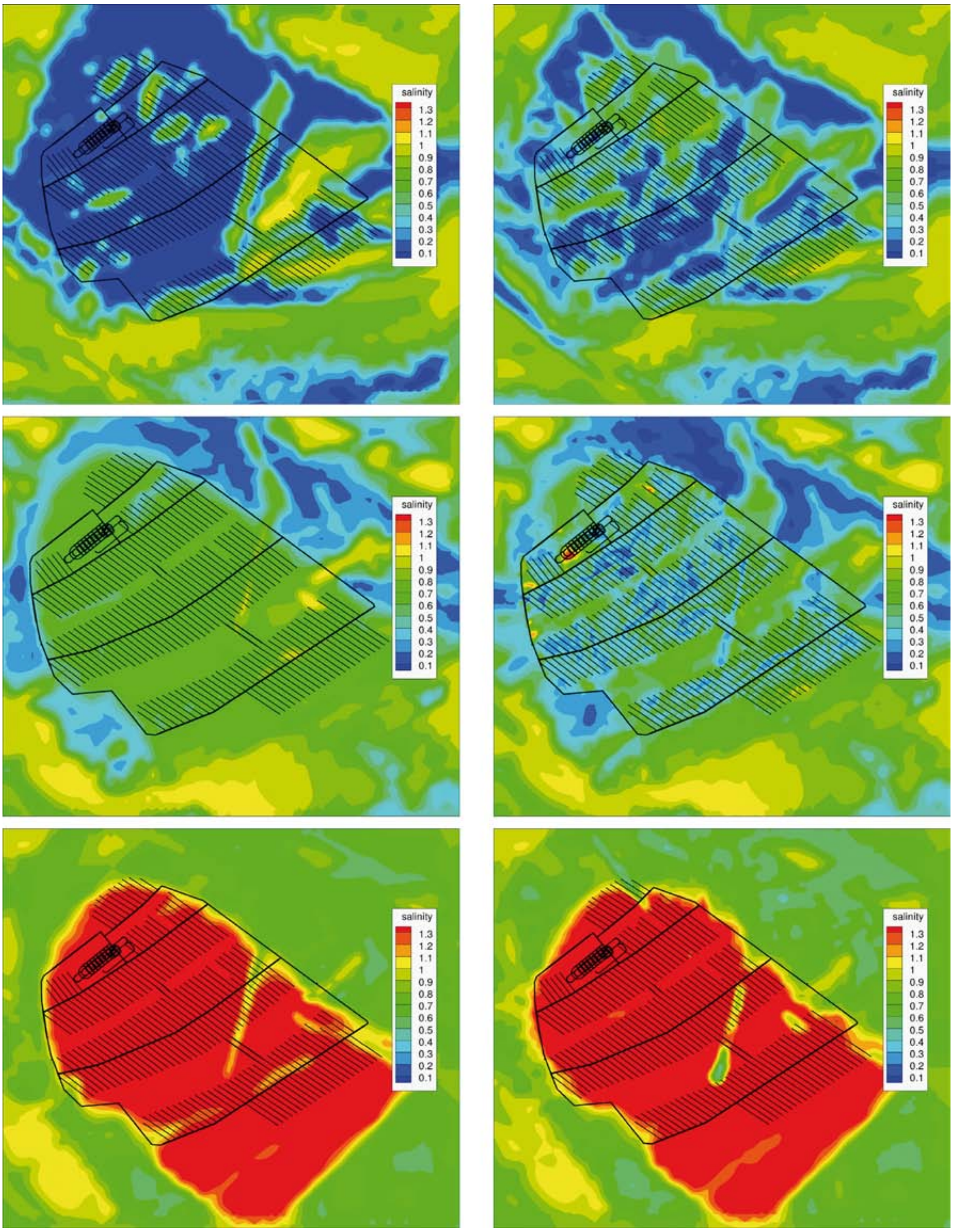

Figure 5-13. *Simulated salinity at −300 m, –465 m and –600 m elevation. Left: Pre-repository conditions. Right: Conditions at the end of operation stage C for grouting level II. The values shown in the legend are expressed in percent by weight.*

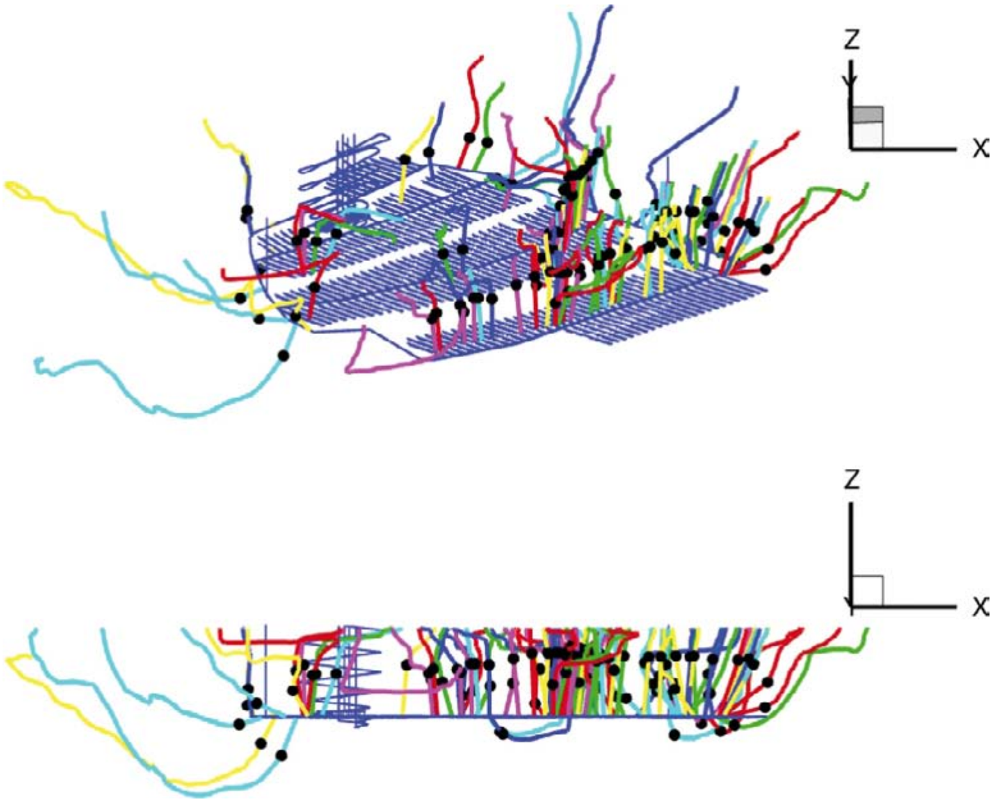

Figure 5-14. *Flow paths of 100 randomly selected particles traced by means of reversed particle tracking. The total simulation time was ten years and the time step is ten days. The black dots indicate the particle positions after one time step, i.e. the transport velocity close the repository is very high. The x-axis points towards East.*

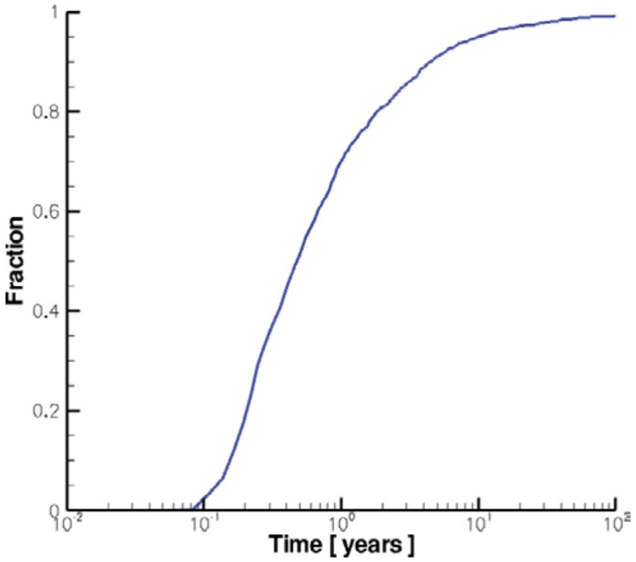

Figure 5-15. *The advective travel times for 2,850 inflow points shown as a cumulative density function curve.*

5.4 Saturation of the backfill

The modelling of the excavation and operational phases handled three successive stages of operation, A–C. When stage B is in operation, the part of the repository layout associated with stage A is assumed to be fully saturated, i.e. closed and with a zero inflow. By the same token, all parts of the repository layout associated with stages A and B are assumed to be fully saturated while stage C is in operation.

The assumption of an instantaneous, full saturation is obviously an approximation as the backfilling of the tunnels defines a starting point of a long transient phase, during which the backfill material will be gradually saturated. Appendix C is an excerpt of /Svensson 2010/. Appendix C briefly presents the hydration process and the approximate method used here to estimate the time scale of the saturation of the backfilling material. In short, the time is estimated by assuming that the hydration process of the unsaturated parts of the backfill can be modelled as a single-phase, saturated groundwater flow system. The specific storage of the unsaturated backfill is assigned a constant value and the specific storage of the saturated backfill another constant value.

The image shown in Figure 5-16 serves an example of the simulation results presented in Appendix C. In Figure 5-16, the boundary condition away from the unsaturated parts of the repository layout equals the hydrostatic pressure at –465 m elevation, i.e. c 5 MPa. The initial pressure in the unsaturated backfill is –40 MPa /Börgesson et al. 2006/. Figure 5-16 suggests that large volumes associated with operation stage A are still at negative pressures after 10 years of hydration, i.e. unsaturated. The main conclusion of the results presented in Appendix C is that the time scale of the saturation process is probably at least 200 years. Due to the approximate method used, where the specific storage of the unsaturated backfill is constant regardless the degree of unsaturation, it is not possible to be more specific.

According to /Enssle and Poppei 2010/, saturation-dependent values of the specific storage enables a dynamic evolution of the hydration process and a method for the implementation in DarcyTools is derived. The implementation is verified numerically by /Enssle and Poppei 2010/ by comparisons with the TOUGH2 code /Pruess et al. 1999/. According to Figure 5-17, the pressure build-up proceeds more rapidly for saturation-dependent values of the specific storage. Figure 5-17 does not explititly say

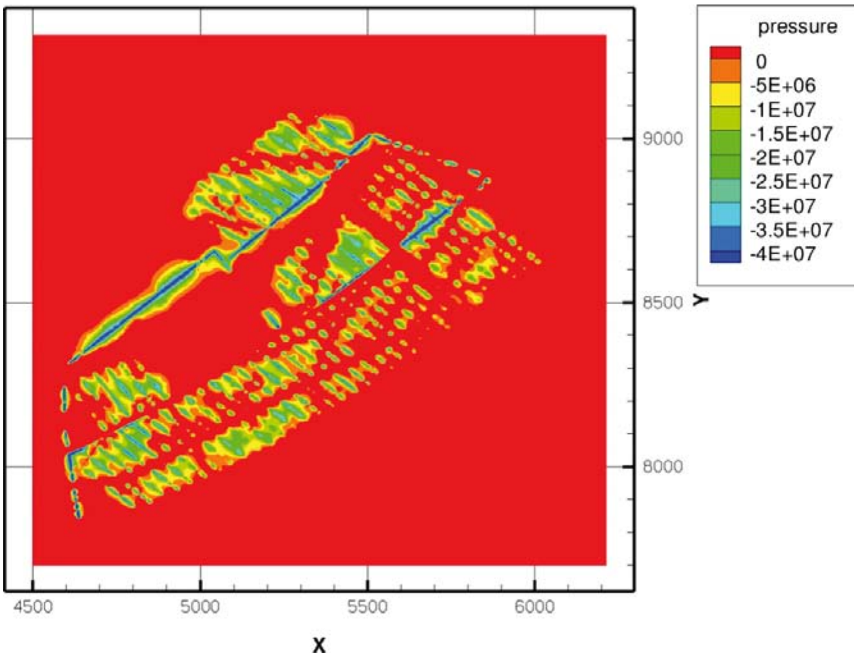

Figure 5-16. Residual pressure distribution (Pa) at –465 m elevation after ten years of saturation of those parts of the repository layout associated with operation stage A (cf Figure 1-2). Here, the initial pressure in the unsaturated backfilled tunnels is set to –40 MPa and the hydrostatic pressure on the boundaries at repository depth to c 5 MPa. The pressure distribution is based on a constant value of the specific storage in the unsaturated parts of the backfill, i.e. regardless of the degree of saturation and another constant value in the saturated parts.

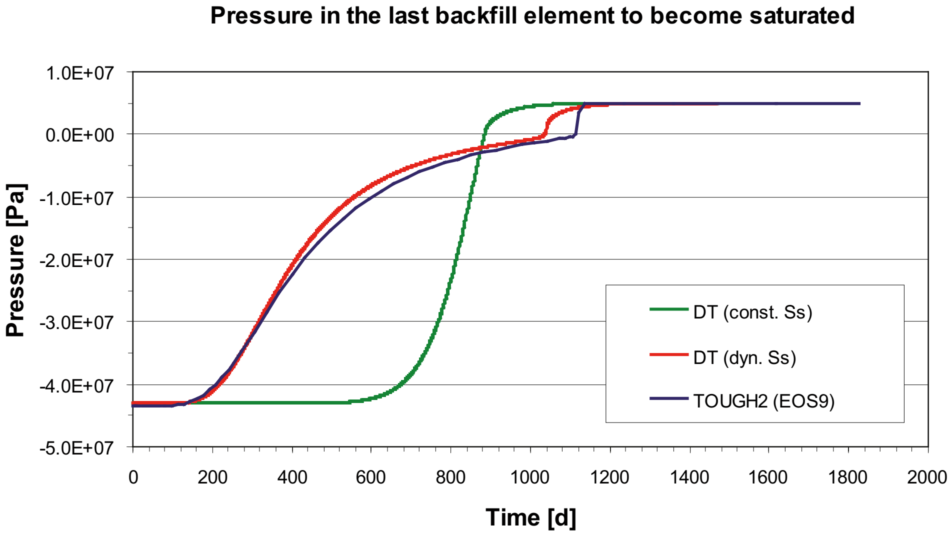

Figure 5-17. *Plot showing results from one of the test cases run by /Enssle and Poppei 2010/. The progress of the pressure build-up in the backfill using a dynamic (red graph) or a constant (green graph) specific storage in DarcyTools differs significantly. A solution obtained with the TOUGH2 code (blue graph) is used to verify the implementation of a dynamic specific storage in DarcyTools. (Source: Figure 3-3 in /Enssle and Poppei 2010/.)*

that the time needed to reach "full saturation" is the same, for the two methods studied, but it indicates the capacity of the approximate method with a constant specific storage. A physical reason for a more rapid saturation is the non-linear capillary suction effects of the backfilling material, which are better described by the dynamic method. Hence, it is suggested that future calculations dealing with saturation are made with the dynamic method. For the sake of objectives of this report, the difference between the two approaches is sufficiently described by /Enssle and Poppei 2010/.

5.5 Sensitivity study

Table 5-2 shows the results of the sensitivity study. A few observations can be made in comparison with inflow rates for the modified base case described in section 4.3. For Case 4, two values are shown due to a change of computational grid. That is, the inflow rates shown in *italic* correspond to the values obtained after a change of the computational grid is made in order to incorporate the layout and pumping at SFR in the flow simulations. The inflow rates shown for Cases 5-7 are calculated for this change of the computational grid hence should be compared with the *italic* values for Case 4.

- Case 1. The exclusion of deposition holes that did not pass the FPC and EFPC criteria rendered a slight decrease in the simulated total inflow rates in the deposition areas, all other parts are unaffected. The small effect found did not motivate any further analysis, for example differentiating between the FPC and EFPC criteria. The total inflow rate for this case was 31.1 L/s vs. 31.2 L/s for the base case.
- Case 2. A single deposition tunnel open rendered a slight increase in the inflow rates to some of the other open parts of the repository layout. This is due to higher pressure gradients to those parts when only one deposition tunnel is present.
- Case 3. Heterogeneous deformation zones in combination with a second realisation of the underlying Hydro-DFN model rendered slightly different inflow rates in some parts of the repository, especially in the deposition areas. However, the total inflow is about the same, 33.4 L/s vs. 31.2 L/s for the base case.

- Case 4. Groundwater salinity appears to have little or no impact on the inflow rates, i.e. the fresh water variant rendered a very minute change in the total inflow rate, 30.9 L/s vs. 31.2 L/s for the base case. (It is recalled that the values shown in italics correspond to the change of computational grid required in order to incorporate a simultaneous pumping at SFR in the flow simulations.)
- Case 5. An extended Hydro-DFN caused a very minute reduction of the total inflow rate; 28.8 L/s vs. 29.8 L/s for the fresh water base case (Case 4). However, this case had a strong effect on the calibration of the inflow rate and total drawdown around SFR, see Appendix D.
- Case 6. This case is based on Case 5 and studies the combined effect of an extended Hydro-DFN and a lower vertical hydraulic conductivity of the off-shore sediments. No additional reduction of the inflow rates was noted for this case. However this variant had a strong effect on the calibration of the inflow rate and total drawdown around SFR, see Appendix D.
- Case 7. This case is based on Case 6 and the setup is explained in Appendix D. The observation made is that a calibrated flow for an extended SFR in operation appears to have little or no impact on the inflow rates to a final repository in the target volume at Forsmark. The flow to a final repository in operation may have a minute effect on the flow field around SFR, see Figure 5-18.

Table 5-2. Simulated inflow rates [L/s] to a final repository at Forsmark for the seven cases handled in the sensitivity study. The simulations are carried out with the entire final repository open and a grouting efficiency corresponding to level II (cf. Table 4-3). CA = central area, DA = deposition area, MT = transport and main tunnels, VS = ventilation shaft. (Inflow rates shown in italics correspond to the values obtained after a change of computational grid is made in order to incorporate the layout of SFR in the flow simulations.)

Part of repository	Base case	1. FPC ∪ EFPC	2. Single tunnel	3. Heterogenity	4. Fresh water	5. Extended Hydro-DFN	6. Sea HSD	7. SFR
CA	2.4	2.4	2.5	2.6	2.3 / *2.0*	*1.5*	*1.5*	*1.5*
DA-A	2.1	2.1	0.02	4.2	2.1 / *2.1*	*2.1*	*2.1*	*2.1*
DA-B	5.2	5.1	–	6.7	5.2 / *5.2*	*5.2*	*5.2*	*5.2*
DA-C	7.4	7.4	–	4.8	7.3 / *7.3*	*7.3*	*7.3*	*7.3*
RAMP	5.2	5.2	5.3	6.0	5.2 / *4.3*	*4.0*	*4.0*	*4.0*
MT-A	2.4	2.4	1.1	3.3	2.3 / *2.4*	*2.3*	*2.3*	*2.3*
MT-B	0.3	0.3	–	0.7	0.3 / *0.3*	*0.3*	*0.3*	*0.3*
MT-C	5.0	5.0	–	4.1	5.0 / *5.0*	*4.9*	*4.9*	*4.9*
VS1	0.5	0.5	–	0.4	0.5 / *0.5*	*0.5*	*0.5*	*0.5*
VS2	0.7	0.7	–	0.6	0.7 / *0.7*	*0.7*	*0.7*	*0.7*
Total	**31.2**	**31.1**	**8.4**	**33.4**	**30.9 / *29.8***	***28.8***	***28.8***	***28.8***

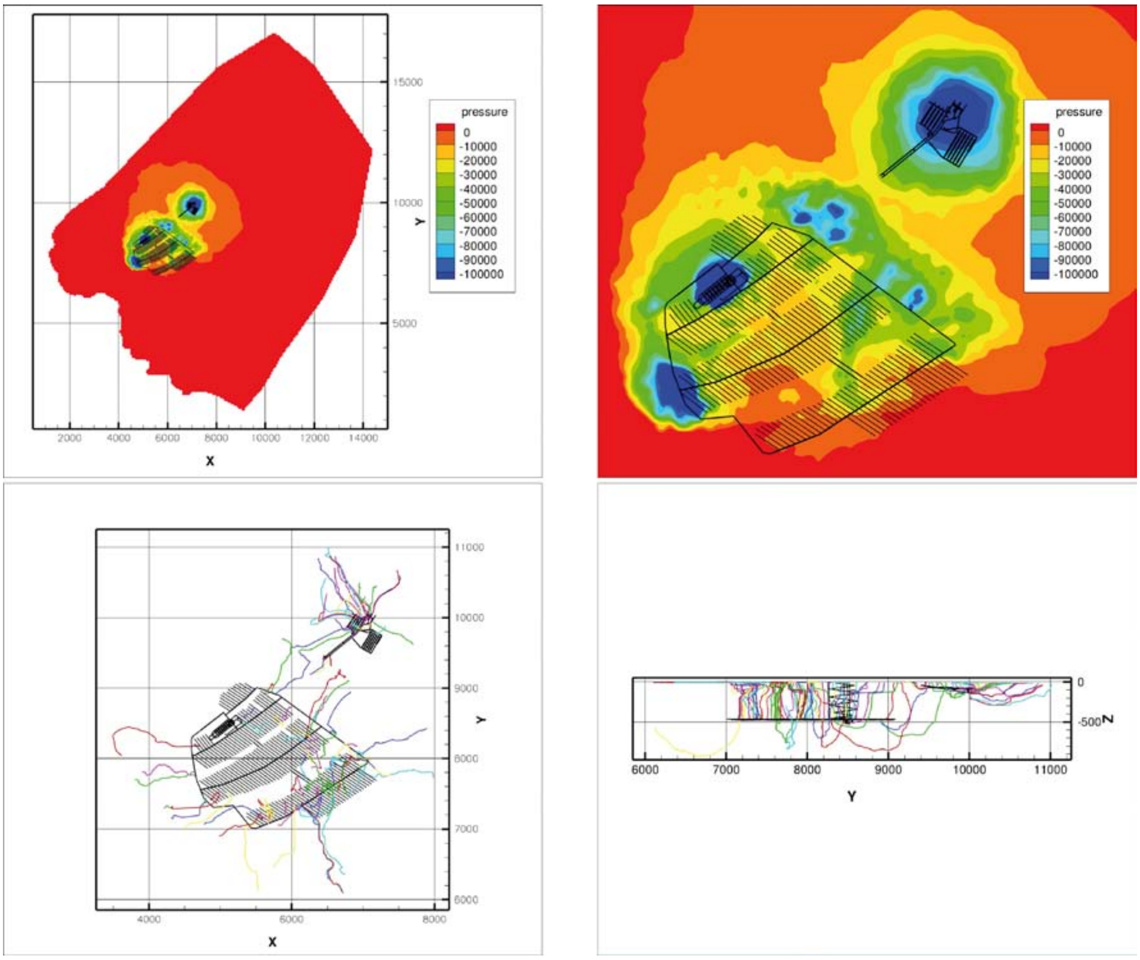

Figure 5-18. Example visualisation showing the pressure interference (Pa) at –150 m elevation for a simultaneous operation of an extended SFR and a final repository. The starting positions of the backward tracking trajectories shown in the lower plots had inflow rates greater than 0.1 L/min.

5.6 Hydraulic rejection criteria

The four criteria presented in section 4.2 are analysed using the modified base case described in section 4.3. The numbers of rejected deposition holes are presented in Table 5-3. The prioritised variants for the scenario analyses carried out in SR-Site are number III and number IV. Variant III looks at the combination of criteria Q1 and Q2 and Variant IV looks at the combination of criteria Q1 and Q2 after all deposition hole positions that fail the combination of criteria FPC and EFPC have been excluded.

Table 5-3. Rejected number of deposition holes for the four variants studied.

Variant	Criterion	Rejected number of deposition holes	Figure
I	{Q1}	157	5-19
II	{Q2}	867	5-20
III	{Q1 ∪ Q2}	874	5-21
IV	{Q1 ∪ Q2} ∣ exclusion of {FPC ∪ EFPC}	814	5-22

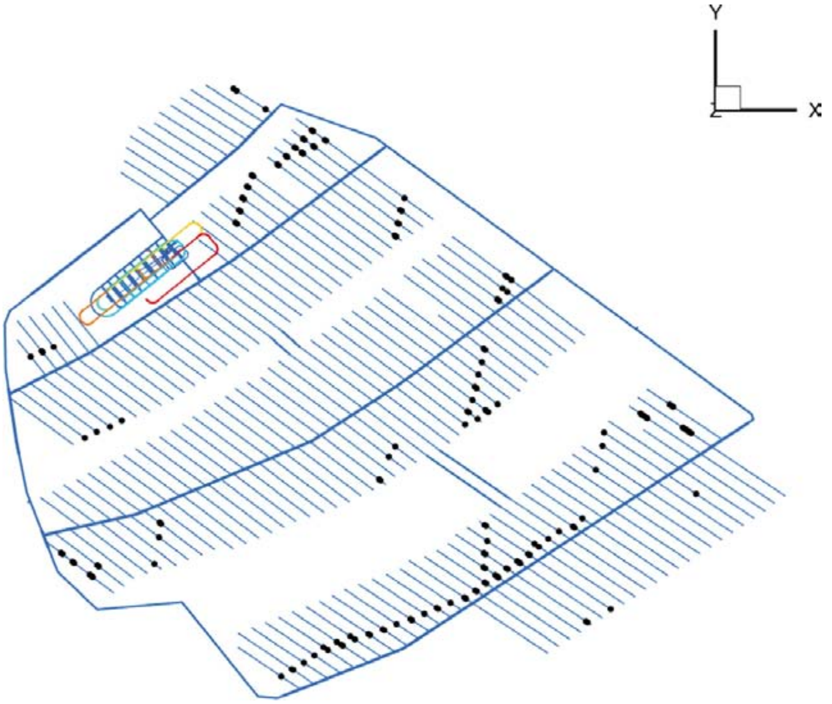

Figure 5-19. Positions of the 157 deposition holes that did not pass the {Q1} criterion (Variant I).

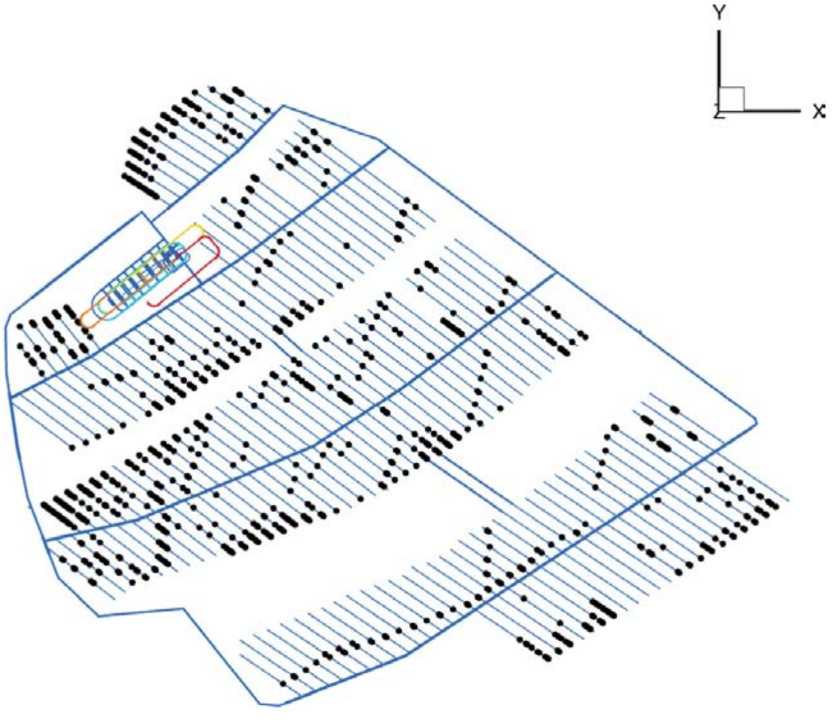

Figure 5-20. Positions of the 867 deposition holes that did not pass the {Q2} criterion (Variant II).

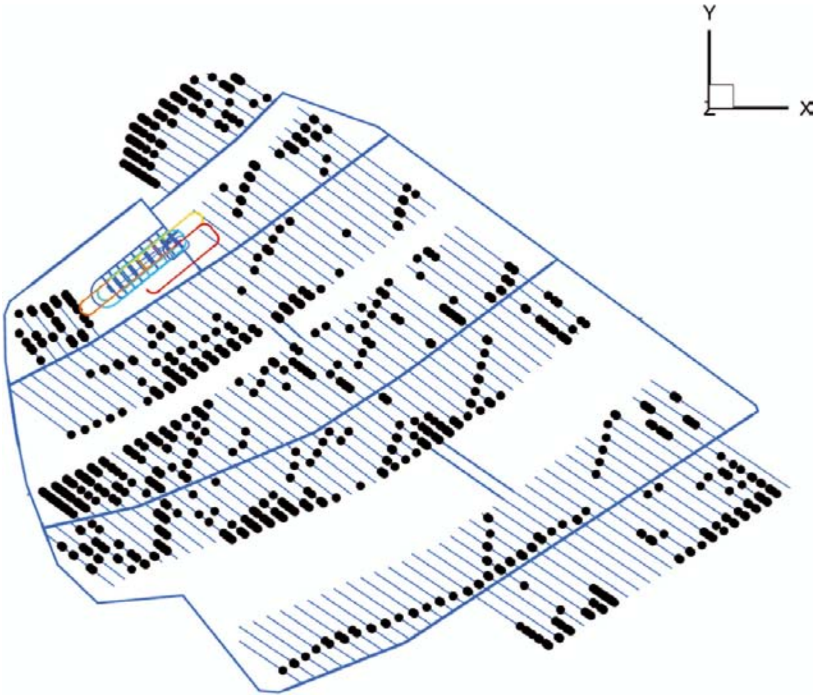

Figure 5-21. Positions of the 874 deposition holes that did not pass the {Q1 ∪ Q2} criterion (Variant III).

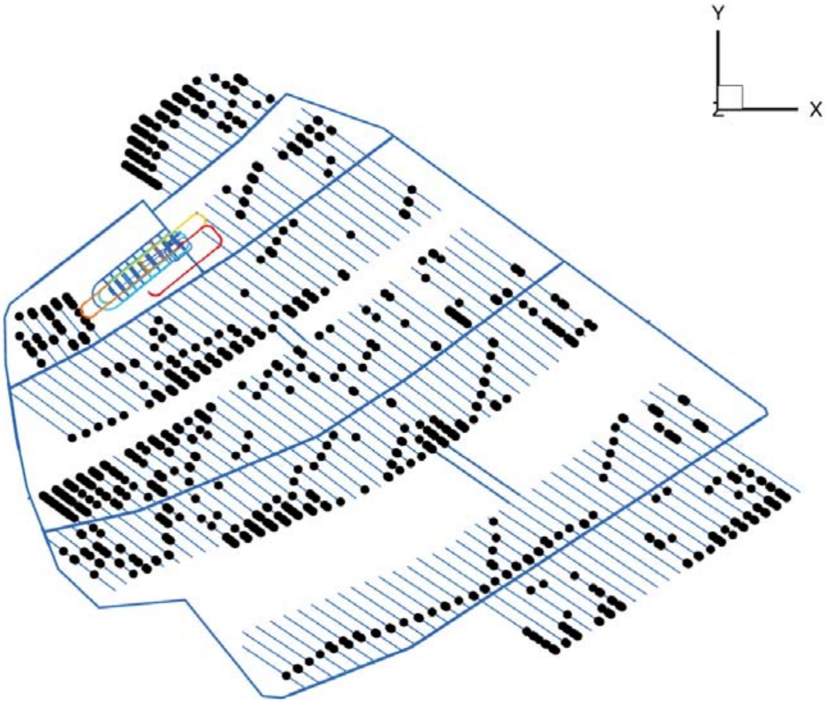

Figure 5-22. Positions of the 814 deposition holes that did not pass the ({Q1 ∪ Q2} | exclusion of {FPC ∪ EFPC}) criterion (Variant IV).

The results presented in Table 5-3 are based on the equivalent continuous porous medium (ECPM) approach. The term “continuous” refers to an unbroken spatial arrangement of porous medium (continuum) type hydraulic properties. In the ECPM approach, grid cells not intersected by flowing fractures are assigned minimum values of the hydraulic conductivity and the kinematic porosity. The values used in this work are shown in Table 4-1.

Appendix E presents a modelling approach where grid cells not intersected by fractures are removed from the computational grid rather than giving them arbitrary low values as in the ECPM approach. In operation, this prohibits advective flow through patches of non-fractured rock as the hydraulic gradients accommodate to the imposed internal noflow boundaries.

Removing grid cells not intersected by fractures significantly reduces the number of grid cells in sparsely fractured rocks, and this relaxation allows for a finer resolution of the remaining computational grid, i.e. more small grid cells where fractures do occur, and hence improved flow solutions. Obviously, the ultimate result of removing and refining the computational grid will result in a discretisation that is conditioned on the discrete fracture network (DFN). To distinguish the elaborated modelling approach from the ECPM approach and the DFN approach, the acronym EDPM is introduced in Appendix E, meaning equivalent discontinuous porous medium.

6 Summary and conclusions

6.1 Scope of work

This report presents inflow rates, drawdown of the groundwater table and upconing of deep saline water for an open final repository for spent fuel at Forsmark. All flow simulations are carried out with the computational code called DarcyTools, which is based on the assumption that flow and transport through sparsely fractured crystalline rocks can be handled as flow and transport through an equivalent continuous porous medium (ECPM). The body of the flow simulations is made for a base case model setup, which was accompanied by a sensitivity study. The latter handled, among other matters, the impact of parameter heterogeneity, different deposition hole rejection criteria, and SFR, the repository for short-lived radioactive waste located c 1 km to the north of the investigated candidate area. Besides informing about possible effects of the excavation and operational phases, the report also presents tentative modelling results for the saturation phase, which starts once the completed parts of the repository are being backfilled.

The setup of the base case has followed the guidelines specified by SKB for the SR Site project. In concrete words, the geometries and hydraulic properties of all modelled discrete features such as individual fractures, deformation zones and repository layout components (shafts, ramp, tunnels and deposition holes) are explicitly imported from a quality assured database managed by SKB, whereas other modelling issues such as initial and boundary conditions, model variants etc followed the prerequisites for modelling outlined in /Selroos and Follin 2010/.

Present-day lakes and wetlands, surface water (stream) runoff rates and groundwater chemistry are loosely used as "calibration targets" for the modelled evolution of the hydrological and hydrochemical conditions during Holocene time (8000 BC to 2000 AD). The simulated conditions at 2000 AD are used as reference for the identification of disturbances caused by the subsequent flow modelling of the excavation and operational phases.

Three scenarios, or operation stages A–C, of the repository development are studied, i.e. not all parts of the repository are open at the same time. As a variant and sensitivity test, the effect of only one deposition tunnel open is also studied.

The impact of grouting on the calculated inflow rates, drawdown of the groundwater table and upconing of deep saline water was studied by altering the hydraulic conductivity of the computational grid cells in contact with the modelled repository. Three levels of grouting efficiency, I–III, are studied for each operation stage A–C.

For the modelling of the saturation process following the closure of the operation phase, a tentative, approximate method is applied. The backfilling material is assumed to have hydraulic properties similar to that of Friedland Clay.

Two inflow rate thresholds are analysed to study the implication of using hydraulic criteria for the rejection of deposition holes. The effect of the hydraulic rejection criteria are analysed alone and in combination with two fracture-geometry-based rejection criteria (Figure 4-10 and Figure 4-11).

6.2 Base case

The simulated total inflow to the modelled repository is found to be in the range 10–50 L/s, depending on the level of the grouting efficiency.

The simulated drawdown was generally quite small (less than 1 m). The largest simulated drawdown is obtained nearby the ramp (about 10 m).

The bedrock below the repository is less permeable than the bedrock above, and, in principle, the groundwater salinity in the vicinity of the repository decreased from 0.8% to 0.3%. This result suggests an infiltration of the less saline groundwater that occur above the repository and very little or no upconing of deep saline groundwater. The largest upconing was noted nearby the ramp (the simulated salinity increased from c 0.8% to 1.3%).

In the present groundwater flow model, the recharge flux of meteoric water is unchanged during the excavation and operational phases. Since the inflow is not accompanied by an increase of the net precipitation, the radius of influence is probably larger than otherwise. Furthermore, since part of the repository area is located below submerged ground conditions, the pressure changes in such areas cause an induced infiltration of sea water. This phenomenon is visible in the salinity plots.

The median of the advective travel times from ground surface to an open repository is of the order of one year. This value is very low and suggests high advective transport velocities close to the repository. It is noted that the advective travel time computations are uncertain since the specified values of the grid cell hydraulic properties are provisional. This uncertainty is particularly true for the applied definition of the grid cell kinematic porosity.

The time needed to achieve a full saturation in the backfilled parts of the repository can be expected to be at least 200 years using a constant specific storage for the hydration of the unsaturated parts of the backfilling material. In reality, the hydration process can be expected to be more rapid, due to, among other things, the capillary suction of the backfilling material. However, it is noted that the time needed to reach complete saturation is about the same for a constant specific storage as for a saturation dependent specific storage. Nevertheless, it is suggested that future calculations with DarcyTools dealing with saturation are made with saturation-dependent values of the specific storage since this enables a dynamic evolution of the hydration process /Enssle and Poppei 2010/.

6.3 Sensitivity study

The exclusion of deposition holes that did not pass the FPC and EFPC criteria rendered a slight decrease in the simulated inflow rates in the deposition areas, all other parts are unaffected. The small effect found did not motivate any further analysis, for example differentiating between the FPC and EFPC criteria.

A single deposition tunnel open rendered a slight increase in the inflow rates to some of the other open parts of the repository layout. This is due to higher pressure gradients to those parts when only one deposition tunnel is present.

Heterogeneous deformation zones in combination with a second realisation of the underlying Hydro-DFN model rendered slightly different inflow rates in some parts of the repository, especially in the deposition areas. However, the total inflow is about the same as for the Reference Case.

Groundwater salinity appears to have little or no impact on the inflow rates. Likewise, neither an extended Hydro-DFN, nor a calibrated flow model for an extended SFR in operation appears to have any significant impact on the inflow rates to a final repository in the target volume at Forsmark. The flow to a final repository in operation may have a minute effect on the flow field around SFR, however.

6.4 Hydraulic rejection criteria

The combination of hydraulic deposition hole rejection criteria and geometry-based deposition hole rejection criteria lead to rejection of about 12% of the possible deposition holes (814 out of a total of 6,916). However, less deposition hole positions fail the different inflow criteria if the sparsely fractures rock is treated as an equivalent discontinuous porous medium (EDPM) instead of as an equivalent continuous porous medium (ECPM), which is the case in the analysis reported in Chapter 5. The EDPM approach is explained in Appendix E.

7 References

SKB's (Svensk Kärnbränslehantering AB) publications can be found at www.skb.se/publications. References to SKB's unpublished documents are listed separately at the end of the reference list. Unpublished documents will be submitted upon request to document@skb.se.

Andersson J-E, Nordqvist R, Nyberg G, Smellie J, Tirén S, 1991. Hydrogeological conditions in the Finnsjön area. Compilation of data and conceptual model. SKB TR-91-24, Svensk Kärnbränslehantering AB.

Axelsson C-L, Follin S, 2000. Grundvattensänkning och dess effekter vid byggnation och drift av ett djupförvar. SKB R-00-21, Svensk Kärnbränslehantering AB.

Bosson E, Gustafsson L-G, Sassner M, 2008. Numerical modelling of surface hydrology and near-surface hydrogeology at Forsmark. Site descriptive modelling SDM-Site Forsmark. SKB R-08-09, Svensk Kärnbränslehantering AB.

Börgesson L, Fälth B, Hernelind J, 2006. Water saturation phase of the buffer and backfill in the KBS-3V concept. Special emphasis given to the influence of the backfill on the wetting of the buffer. SKB TR-06-14, Svensk Kärnbränslehantering AB.

Christiansson R, Bolvede P, 1987. Byggnadsgeologisk uppföljning – Slutrapport. SKB SFR 87-03, Svensk Kärnbränslehantering AB.

Dershowitz W, Winberg A, Hermanson J, Byegård J, Tullborg E-L, Andersson P, Mazurek M, 2003. Äspö Task Force on modelling of groundwater flow and transport of solutes. Task 6c. A semi synthetic model of block scale conductive structures at the Äspö HRL. Äspö Hard Rock Laboratory, International Progress Report IPR-03-13, Svensk Kärnbränslehantering AB.

El Tani M, 2003. Circular tunnel in a semi-infinite aquifer. Tunneling and Underground Space Technology, 18, 49-55.

Enssle C P, Poppei J, 2010. Implementation and testing of an improved methodology to simultate resaturation processes with DarcyTools. SKB R-09-54, Svensk Kärnbränslehantering AB.

Fetter C W, 1994. Applied Hydrogeology. Prentice-Hall Inc.

Follin S, 1992. Numerical calculations on heterogeneity of groundwater flow. SKB TR-92-14, Svensk Kärnbränslehantering AB.

Follin S, 2008. Bedrock hydrogeology Forsmark. Site descriptive modelling. SDM-Site Forsmark. SKB R-08-95, Svensk Kärnbränslehantering AB.

Follin S, Stigsson M, Svensson U, 2005. Regional hydrogeological simulations for Forsmark – numerical modelling using DarcyTools. Preliminary site description Forsmark area – version 1.2. SKB R-05-60, Svensk Kärnbränslehantering AB.

Follin S, Levén J, Hartley L, Jackson P, Joyce S, Roberts D, Swift B, 2007a. Hydrogeological characterisation and modelling of deformation zones and fracture domains. Forsmark modelling stage 2.2. SKB R-07-48, Svensk Kärnbränslehantering AB.

Follin S, Johansson P-O, Hartley L, Jackson P, Roberts D, Marsic N, 2007b. Hydrological conceptual model development and numerical modelling using CONNECTFLOW, Forsmark modelling stage 2.2. SKB R-07-49, Svensk Kärnbränslehantering AB.

Follin S, Hartley L, Jackson P, Roberts D, Marsic N, 2008. Hydrological conceptual model development and numerical modelling using CONNECTFLOW, Forsmark modelling stage 2.3. SKB R-08-23, Svensk Kärnbränslehantering AB.

Gustafson G, Fransson Å, Funehag J, Axelsson M, 2004. Ett nytt angreppssätt för bergbeskrivning och analysprocess för injektering. Väg- och vattenbyggaren (4) 2004, 10–15.

Haggerty R, Gorelick S M, 1995. Multi-rate mass transfer for modelling diffusion and surface reactions i media with pore-scale heterogeneity. Water Resources Research, 31(10), 2383–2400.

Hedenström A, Sohlenius G, Strömgren M, Brydsten L, Nyman H, 2008. Depth and stratigraphy of regolith at Forsmark. Site desprictive modelling SDM-Site Forsmark. SKB R-08-07, Svensk Kärnbränslehantering AB.

Holmén J G, Stigsson M, 2001. Modelling of future hydrogeological conditions at SFR. SKB R-01-02, Svensk Kärnbränslehantering AB.

Johansson P-O, 2008. Description of surface hydrology and near-surface hydrogeology at Forsmark. Site descriptive modelling SDM-Site Forsmark. SKB R-08-08, Svensk Kärnbränslehantering AB.

Joyce S, Applegate D, Hartley L, Hoek J, Simpson T, Swan D, Marsic N, Follin S, 2010. Groundwater flow modelling of periods with temperate climate conditions – SR-Site Forsmark. SKB R-09-20, Svensk Kärnbränslehantering AB.

Munier R, 2006. Using observations in deposition tunnels to avoid intersections with critical fractures in deposition holes. SKB R-06-54, Svensk Kärnbränslehantering AB.

Olofsson I, Simeonov A, Stephens M, Follin S, Nilsson A-C, Röshoff K, Lindberg U, Lanaro F, Fredriksson A, Persson L, 2007. Site descriptive modelling Forsmark, stage 2.2. A fracture domain concept as a basis for the statistical modelling of fractures and minor deformation zones, and inter-disciplinary coordination. SKB R-07-15, Svensk Kärnbränslehantering AB.

Patankar S V, 1980. Numerical heat transfer and fluid flow. Hemisphere Publishing Company, McGraw-Hill Book Company.

Pruess K, Oldenburg C, Moridis G, 1999. TOUGH2 User's Guide, Version 2.0. Earth Sciences Division, Ernest Orlando Lawrence Berkely national Laboratory, California.

Rhén I, Follin S, Hermanson J, 2003. Hydrological site descriptive model – a strategy for its development during site investigations. SKB R-03-08, Svensk Kärnbränslehantering AB.

Rouhiainen P, Sokolnicki M, 2005. Difference flow logging in borehole KFM06A. SKB P-05-15. Svensk Kärnbränslehantering AB.

Selroos J-O, Follin S, 2010. SR-Site groundwater flow modelling methodology, setup and results. SKB R-09-22. Svensk Kärnbränslehantering AB.

SKB, 2005a. Preliminary site description. Forsmark area – version 1.2. Updated 2005-11-09. SKB R-05-18, Svensk Kärnbränslehantering AB.

SKB, 2005b. Programme for further investigations of geosphere and biosphere. Forsmark site investigation. SKB R-05-14, Svensk Kärnbränslehantering AB.

SKB, 2008a. Site decription of Forsmark at completion of the site investigation phase. SDM-Site Forsmark. SKB TR-08-05, Svensk Kärnbränslehantering AB.

SKB, 2008b. Underground Design Forsmark, Layout D. SKB R-08-116, Svensk Kärnbränslehantering AB.

SKB, 2009. Design premises for a KBS-3V repository based on the results from the safety assessment SR-Can and some subsequent analyses. SKB TR-09-22, Svensk Kärnbränslehantering AB.

Stephens M B, Fox A, La Pointe P R, Simeonov A, Isaksson H, Hermanson J, Öhman J, 2007. Geology Forsmark. Site descriptive modelling Forsmark stage 2.2. SKB R-07-45, Svensk Kärnbränslehantering AB.

Svensson U, 2010. Evaluation of a new method to estimate the hydration time of the tunnel backfill. SKB R-10-06, Svensk Kärnbränslehantering AB.

Svensson U, Ferry M, Kuylenstierna H-O, 2010. DarcyTools, Version 3.4. Concepts, methods and equations. SKB R-07-38, Svensk Kärnbränslehantering AB.

Thiem G, 1906. Hydrologische methoden. Gebhatdt. Leipzig.

Vidstrand P, Follin S, Zugec N, 2010. Groundwater flow modelling of periods with periglacial and glacial climate conditions – SR-Site Forsmark. SKB R-09-21, Svensk Kärnbränslehantering AB.

Vilks P, 2007. Rock matrix permeability measurements on core samples from borehole KFM01D. SKB P-07-162, Svensk Kärnbränslehantering AB.

Öhman J, Follin S, 2010. Site investigation SFR. Hydrogeological modelling of SFR. Model version 0.2. SKB R-10-03, Svensk Kärnbränslehantering AB.

Unpublished documents

SKBdoc id, version	Title	Issuer, year
12000954 ver 1.0	SFR Kontrollprogram Bergkontroll. Bergkontrollgruppens årsrapport 2008.	Vattenfall Hydropower, 2008

Appendix A

A Free surface algorithm

A.1 Introduction

The elevation of the groundwater table may affect the pressure field in the bedrock depending on the hydraulic contact between the Quaternary deposits and the bedrock. Unfortunately it is not straight forward to calculate the position of the groundwater table. From the literature two methods are available:

- The unsaturated-saturated approach, which means that the unsaturated zone is included in the flow simulation and that the so called Richard's equation is solved.
- Free surface approach. The main assumption of the method is that the conditions in the unsaturated zone do not significantly affect the position of the groundwater table.

DarcyTools applies a method to determine the groundwater table that is somewhat in between the two approaches listed above. The basic idea is as follows.

The flow situation shown in Figure A-1 assumes saturated flow through porous medium and results in a particular pressure distribution results where points on a surface with atmospheric pressure (gauge pressure = 0) can be identified. This surface is not the groundwater table, however, because horizontal flow is calculated above this surface. The key feature of the free surface algorithm in DarcyTools is to prevent horizontal flow above the surface of atmospheric pressure by simply reducing the horizontal hydraulic conductivity above this surface. This is done in an iterative manner: 1) the flow problem is solved and the position of the atmospheric pressure is identified, 2) the horizontal conductivities are revised according to the position of the surface of atmospheric pressure, and 3) the flow problem is recalculated, etc. Note that if a rising surface is recalculated, the horizontal conductivities below the new surface of atmospheric pressure should be restored to the fully saturated values.

A.2 Objectives

The objective of this appendix case is to verify that the free surface algorithm in DarcyTools predicts a groundwater table that is in agreement with an analytical solution to the flow situation shown in Figure A-2.

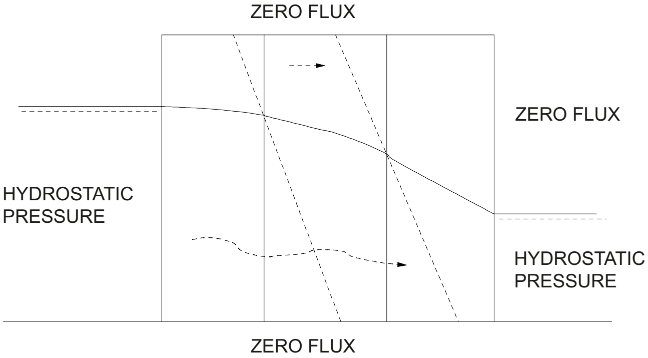

Figure A-1. *Illustration of a flow solution where saturated flow is assumed. This assumption results in an incorrect position of the groundwater table.*

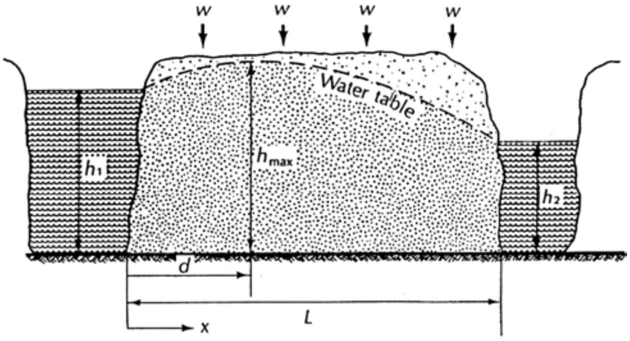

Figure A-2. Illustration of the studied situation and the notation used in Equation (A-1). The symbols are explained in the text. (Figure 5-19 in /Fetter 1994/.)

A.3 Analytical solution

If Dupuit's assumption is invoked, which imply vertical equipotentials, the hydraulic head, h, between $h(x = 0) = h_1$ and $h(x = L) = h_2$, at a distance, x, between the two head boundaries, may be written as /Fetter 1994/:

$$h(x) = \sqrt{h_1^2 - \frac{\left(h_1^2 - h_2^2\right)x}{L} + \frac{w}{K}\left(L - x\right)x} \qquad \text{(A-1)}$$

where K [LT^{-1}] is the hydraulic conductivity in the direction of flow and w [LT^{-1}] is the recharge.

One way to simulate Dupuit's assumptions in DarcyTools is to introduce a higher conductivity in the vertical direction (as compared to the horizontal ones). This will make the vertical pressure distribution close to the hydrostatic one, i.e. vertical equipotentials.

A.3 Numerical simulation

The hydraulic properties used for the flow simulation in DarcyTools are shown in Table A-1.

A.4 Summary and conclusions

The comparison with the analytical solution is shown in Figure A-3. Figure A-4 shows the flow pattern. The steady state groundwater table, as predicted by DarcyTools, is in good agreement with the corresponding analytical solution.

Table A-1. Simulation parameters.

Domain size	100 m (horizontal), 50 m (vertical)
Grid (cell) size	$\Delta x = \Delta z = 1$ m
Hydraulic conductivity	10^{-8} m/s (horizontal), 10^{-6} m/s (vertical)
Boundary conditions	Bottom: no flow Top: prescribed flux (P–E); 100 mm/y or 20 mm/y Left: hydrostatic pressure, $h_1 = 30$ m Right: hydrostatic pressure, $h_2 = 20$ m

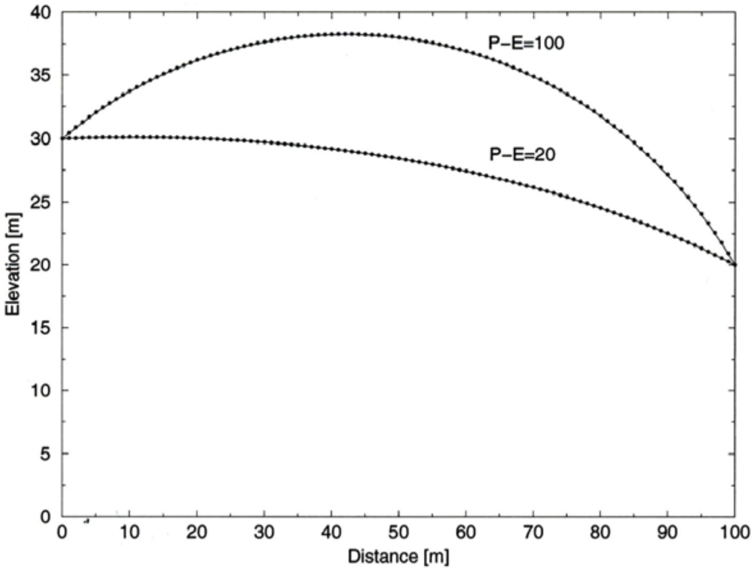

Figure A-3. *Comparison between analytically (line) and numerically (dots) calculated hydraulic heads for two (P-E) values, 20 mm/y and 100 mm/y.*

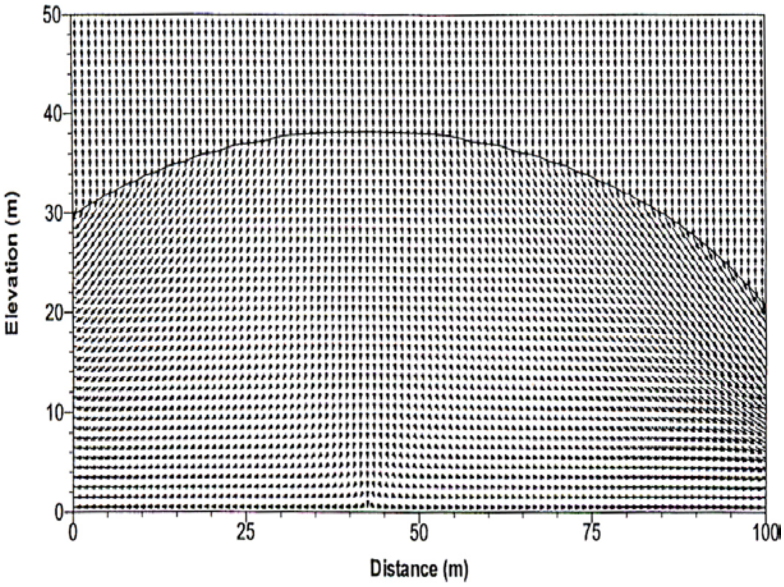

Figure A-4. *Predicted flow and groundwater table for (P-E) = 100 mm/y.*

B Tunnel routine

B.1 Introduction

A routine is implemented in DarcyTools to simulate the inflow of groundwater to tunnels and other underground objects that are subjected to atmospheric pressure. The routine assumes that the resolution of the computational grid is of the same size as the underground objects handled.

Figure B-1 shows the basic idea. The large circle indicates the cross-section of an underground object (construction). All cells that are in contact with the border of the object are marked up by red rectangles and the associated cell walls are indicated by blue circles. The marked up cells are assigned an atmospheric pressure ($p = 0$) at their centres and the hydraulic conductivities of the cell walls (K_{cw}) are matched against a predefined hydraulic conductivity threshold (K_t) representing a specified level of grouting efficiency. The routine applies the following criterion:

$$K_{cw,new} = \min(K_{cw,old}, K_t) \qquad \text{(B-1)}$$

This adjustment of the cell wall hydraulic conductivity is used to simulate the effect of grouting in the work reported here.

B.2 Objectives

The objective of this appendix is to evaluate the accuracy of the tunnel routine for conditions (grid cell size and tunnel geometries) relevant for a final repository.

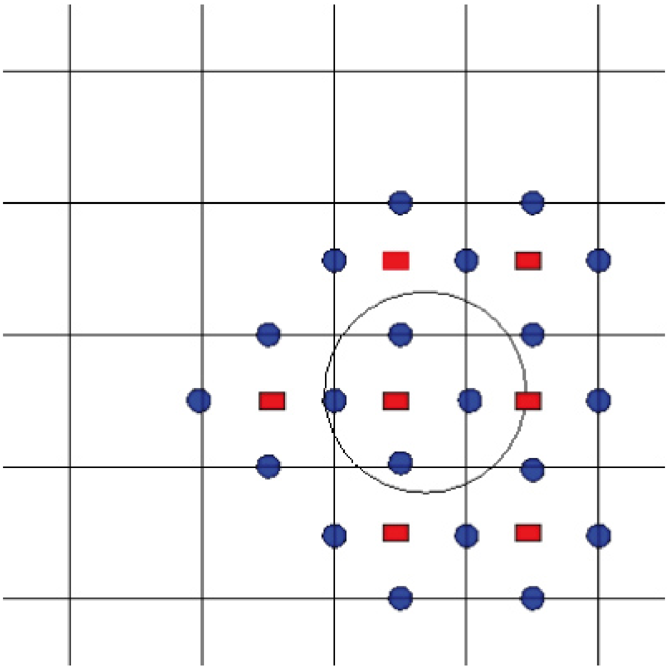

Figure B-1. *Cartoon showing the structural components of the tunnel routine in DarcyTools. The thin line is the perimeter of a tunnel. Red rectangles indicate the centres of the cells in contact with the tunnel. Blue circles indicate the cell walls of these cells.*

B.3 Comparison with an analytical solution

For steady-state flow towards a circular tunnel in a semi-infinite isotropic and homogeneous aquifer the inflow rate per unit length of the tunnel, q [m^3/s], may be derived from well function provided by /Thiem 1906/:

$$q = 2\pi\ K\ d\left[\ln\left(\frac{2d}{r}\right)\right]^{-1} \tag{B-2}$$

where K is the hydraulic conductivity of the porous medium, r is the radius of the tunnel and d is the depth below a constant-head boundary, e.g. a fixed groundwater table. Equation (B-2) is valid for $\frac{d}{r} >> 1$. If $\frac{d}{r} \approx 10$, the error in q is of the order of 1%.

An outline of the flow model setup in DarcyTools is shown in Figure B-2. The hydraulic properties used for the flow simulation are shown in Table B-1.

The comparison with the analytical solution is shown in Figure B-3. /El Tani 2003/ provides means to calculate correction factors for finite values of *r/d*. For the present setup variants of *r/d*, it is found that the calculated correction factors are insignificant. Moreover, a sensitivity study with focus on the discretisation of the computational grid in proximity to the tunnel showed that grid independent solutions are achieved when the cell size is of the same size as the tunnel radius or smaller, see Table A-2.

It is found, however, that the horizontal size of the domain needed to be quite large (4,000 m) to achieve correct solutions. A smaller size (2,000 m) affected the inflow rates with several percent.

Table B-1. Parameters values for simulations of inflow to an open tunnel.

Domain size	4,000 m (horizontal), 2,000 m (vertical)
Grid (cell) size	Tunnel: Max(Δx, Δz) = 0.1 m Near field: Max(Δx, Δz) = 0.5 m Far field: Max(Δx, Δz) = 8 m
Hydraulic conductivity	10^{-8} m/s
Boundary conditions	Bottom: no flow Vertical: no flow Top: atmospheric pressure Tunnel: atmospheric pressure
Tunnel data	Depth: 500 m Radius: 1 m, 2 m and 4 m

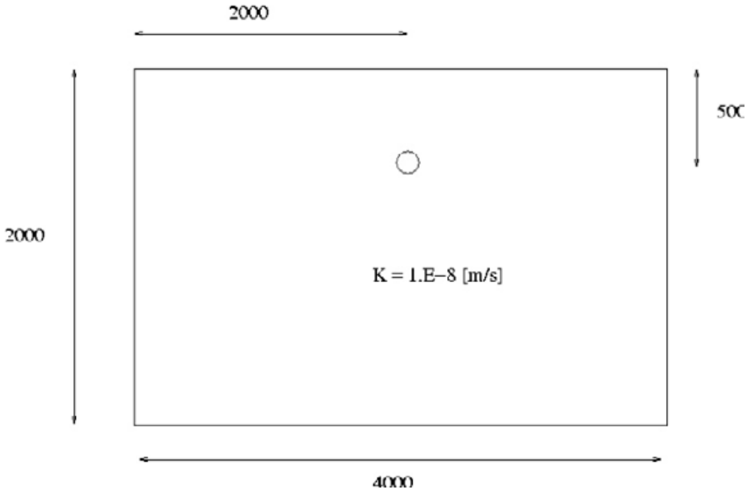

Figure B-2. Illustration of the studied situation.

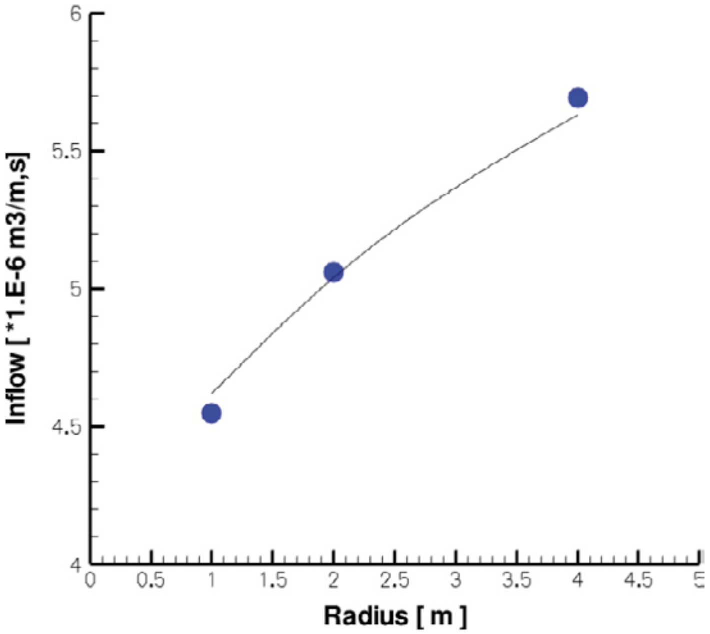

Figure B-3. Comparison between analytically (line) and numerically (dots) calculated inflow rates for different tunnel radii.

Table B-2. Comparison between analytical and numerical solutions of the inflow rate, q, to the tunnel shown in Figure B-2 and Table B-1. Inflow rates (q = N·10^{-6} m^3/s/m) are shown for three radii and three cell sizes.

Solution	Tunnel radius (m) 1	 2	 4
Analytical	4.55	5.06	5.69
Numerical, cell size (Δx, Δz) = 0.5 m	4.62	5.04	5.63
Numerical, cell size (Δx, Δz) = 1 m	4.80	5.14	5.67
Numerical, cell size (Δx, Δz) = 2 m	4.80	5.37	5.79

B.4 Coarse computational grids vis-à-vis the tunnel radius

Figure B-4 shows three different cases of tunnels where the tunnel diameter is less than the cell size of the computational grid (4 m). In case A, four cells will be marked as tunnel cells, in case B two cells and in case C one cell. The numerical flow simulations are carried out for a tunnel radius of 1 m and the analytical solutions are made for two values of the tunnel radius, 1 m and 2 m. The numerical and analytical solutions are shown in Table B-3. (It is noted that the analytical solution is sensitive to the tunnel radius, whereas the tunnel radius is unimportant for the numerical solution if the radius is less than the cell size (discretisation).)

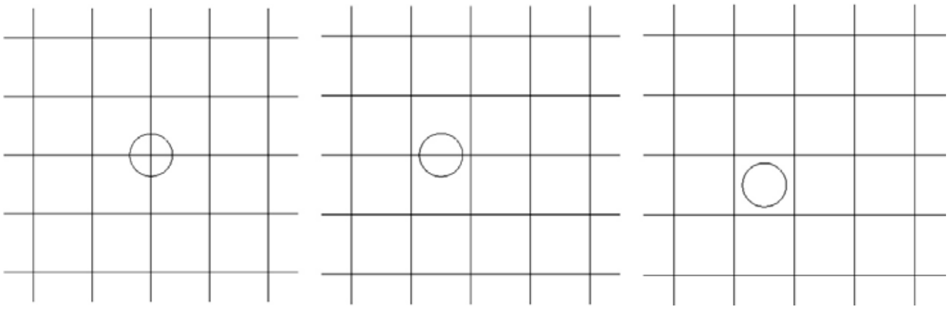

Figure B-4. Illustration showing three tunnel positions, A–C, with regard to the cell size of a coarse computational grid.

Table B-3. The inflow rates ($q = N \cdot 10^{-6}$ m^3/s/m) shown in the upper row are calculated using the tunnel routine for three different positions of the tunnel, A–C, see Figure B-3. The values shown in the lowermost two rows represent inflow rate ratios for two different tunnel radii, 1 m and 2 m. The average of the six ratios is 1.01.

	Case		
Solution	**A**	**B**	**C**
Numerical q (tunnel routine with r = 1)	5.28	4.87	4.36
(Numerical q)/(Analytical q with r = 1 m)	1.16	1.07	0.96
(Numerical q)/(Analytical q with r = 2 m)	1.04	0.96	0.86

B.5 Grouting

The analytical equation shown in Equation (B-2) does not account for the effect of grouting. If the thickness, *t*, of the grouted zone around an open tunnel and the hydraulic conductivity of the grouted bedrock, K_t (cf Equation (B-1), are known, the inflow rate to the tunnel may be written as /Gustafson et al. 2004/:

$$q = 2\pi \; K \; d\left[\ln\left(\frac{2d}{r}\right) + (K/K_t - 1)\,\ln(1+t/r)\right]^{-1} \tag{B-3}$$

The application of the tunnel routine to the studied repository layout at Forsmark uses a cell size of the computational grid of 4 m close to the deposition tunnels. This resolution compares well with the dimensions of the deposition tunnels, which have a height 4.8 m and a width 4.2 m. Hence, the equivalent diameter of the tunnel is c 5 m, which is somewhat greater than the cell size of the computational grid. From Figure B-1, it is concluded that the "penetration depth" associated with Equation (B-1) for a uniform computational grid is approximately of the same size as the cell size, i.e. in this case c 4 m.

Table B-4 shows the parameter values used in DarcyTools to evaluate the accuracy of the tunnel routine as applied in the work reported here. The calculated inflow rates are compared with the analytical solution shown in Equation (B-3). The background hydraulic conductivity of the bedrock is set to 10−7 m/s and three different levels of the grouting efficiency are tested: 10^{-9} m/s, 10^{-8} m/s and 10−7 m/s. The thickness of the grouted zone was set to 4 m. The calculations are made for the three tunnel positions shown in Figure B-3. The results are summarised in Table B-5.

Table B-4. Parameters values for simulations of inflow to an open tunnel in a grouted bedrock.

Domain size	4,000 m (horizontal), 2,000 m (vertical)
Grid (cell) size	(Δx, Δz) = 4 m
Hydraulic conductivity	K = 10^{-7} m/s
	$K_t = 10^{-9}$ m/s, 10^{-8} m/s, 10^{-7} m/s
Boundary conditions	Bottom: no flow
	Vertical: no flow
	Top: atmospheric pressure
	Tunnel: atmospheric pressure
Tunnel data	Depth: 500 m
	Radius: 1 m
	t = 4 m

Table B-5. Comparison between numerical and analytical solutions of the inflow rate, q, for the parameter values specified in Table B-4. Inflow rates ($q = N \cdot 10^{-5}$ m³/s/m) are shown for three tunnel positions, A–C, and three levels of grouting efficiency (K_t).

	K_t (m/s)		
Tunnel position	**10^{-9}**	**10^{-8}**	**10^{-7}**
A	0.38	2.41	5.28
B	0.29	1.98	4.87
C	0.19	1.48	4.36
Numerical q (Average)	0.29	1.96	4.84
Analytical q with r = 1 m	0.19	1.47	4.55
(Numerical q)/(Analytical q with r = 1 m)	1.52	1.33	1.06

B.6 Summary and conclusions

The comparison with the analytical solutions in Equation (B-2) and Equation (B-3) are shown in Table B-3 and Table B-5, respectively.

The results of the flow simulations using the tunnel routine for a non grouted bedrock are summarised in Table B-3. It is found that the tunnel routine give inflow rates that are close to rates of the analytical solution shown in Equation (B-2).

For a grouting efficiency of $K_t = 10^{-7}$ m/s, the values shown in Table B-5 represent the effect of the position of the tunnel in the grid only as no modification of the hydraulic conductivity of the bedrock near the tunnel is applied, i.e. for this case Equation (B-3) becomes identical to Equation (B-1). The average deviation from the analytical solution for $K_t = 10^{-7}$ m/s is c 6%, thus suggesting that the tunnel routine works quite well also when the cell size is comparable to the tunnel diameter.

When the level of the grouting efficiency increases, i.e. when the value of K_t decreases, the calculated inflow rates decreases significantly. For $K_t = 10^{-8}$ m/s, the average deviation from the analytical solution is found to be c 33%, and for $K_t = 10^{-9}$ m/s, the average deviation from the analytical solution is found to be c 52%.

The values shown in Table B-5 assume that the cell size of the computational grid is of the same order as the tunnel diameter. The sensitivity of the results to the cell size is looked at by using a systematic grid refinement of the resolution of the computational grid near the tunnel from 4 m to 0.25 m. This change rendered an average deviation from the analytical solution for the higher resolution of c 10% for $K_t = 10^{-9}$ m/s.

Appendix C

C Saturation of backfill

C.1 Background

When the deposition tunnels are backfilled, large parts of the pore space in the backfill are filled with air. The unsaturated pore space will eventually be filled with water, but the time scale for this hydration process is not known in detail. /Börgesson et al. 2006/ studied the problem using advanced two-phase models. Such models provide solutions based on fundamental physical laws and well tested empirical relations. /Börgesson et al. 2006/ concluded that both the properties of the backfill and those of the surrounding rock affect the time scale of the hydration process.

C.2 Objectives

A problem of using two-phase models is that it is presently hard to include an adequate description of the structural-hydraulic properties of a discrete fracture network. For this reason, a simplistic approach to the complex hydration process of the backfill has been suggested using DarcyTools /Svensson 2010/. The suggested approach has the advantage of being applicable to the geometry of the final repository modelled in SR-Site, which is embedded in sparsely fractured bedrock with water carrying fractures. The objective of this appendix is to describe the essence of the simplistic approach suggested by /Svensson 2010/ and to provide a demonstration of its application to a final repository at Forsmark.

C.3 Brief description of the saturation process

Unsaturated flow conditions occur during the different stages of a final repository for spent nuclear fuel (construction, operation and post-closure). Different processes and properties such as capillary suction and relative permeability act upon the hydraulic behaviour of the system and may affect the duration of the saturation of the initially unsaturated parts. Figure C-1 shows an illustration of some of the processes involved. The illustration does not claim to be complete, but it is clear that we are dealing with three phases (solid, air and water) with an air phase that is subject to compression and dissolution in the water phase.

- The groundwater flow in the discrete fracture network in the bedrock provides the groundwater up to the tunnel face.
- The saturation front is defined by the zero pressure line, i.e. where the gauge pressure equals the atmospheric pressure. Towards the tunnel, the gauge pressure decreases and towards the bedrock it increases.
- In the unsaturated part, groundwater is transported by capillary suction and may also be transported as vapor diffusion.
- The air initially present in the backfill may disappear by several processes: dissolution in the water, gravitational rise and by diffusion and advection when dissolved in the water. A significant compression of the air can also be expected when the pore pressure rises.
- Temperature and salinity gradients may affect most processes.

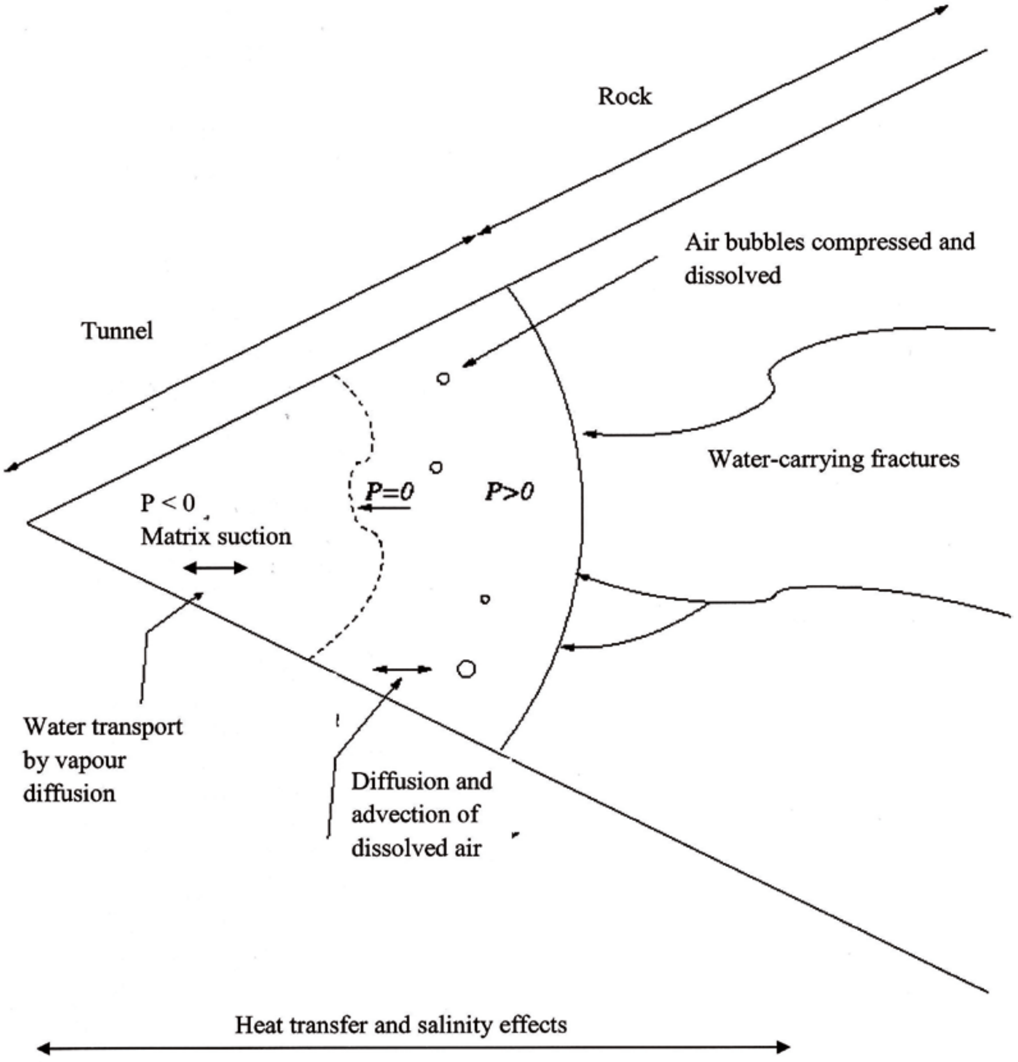

At the wetting front

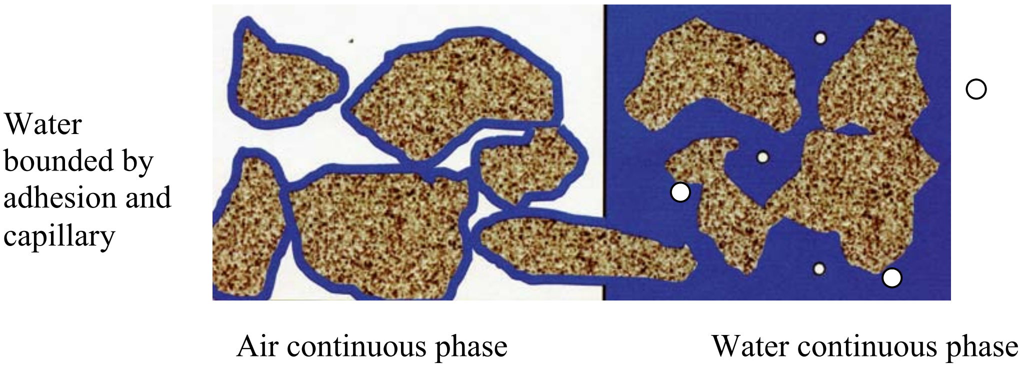

***Figure C-1.** Schematic illustration of relevant physical processes during the saturation of the unsaturated tunnel backfill. In the figure, P denotes gauge pressure.*

C.4 Attempted simplification

If all, or most, of the processes discussed above are considered in a numerical model, the solution has to be based on fundamental physical laws and well tested empirical relations, see /Börgesson et al. 2006/. The simplistic approach suggested by /Svensson 2010/ is used in the work reported here. The approach is based on two main assumptions.

- It is assumed that the hydration process of the unsaturated parts of the backfill can be modelled as single-phase, saturated groundwater flow system, where the inflow of groundwater to the repository is mainly governed by the pressure gradients and the resistance in the rock, the saturated part of backfill and the position of the wetting front.
- The specific storativity, S_s , is given an untraditional role, as it used to simulate the removal of the volume occupied by air in the backfill. That is, it is regarded as the ratio of the change of the initially air filled porosity in the backfill , $\Delta[\phi(1-S_w)]$, and the associated head change, $\Delta P / \rho g$:

$$S_s = \frac{\Delta[\phi(1-S_w)]\,\rho g}{\Delta P} \qquad \text{(C-1)}$$

where
ϕ = porosity of the backfill [–]
S_w = saturation [–]
ρ = fluid density [kg/m^3]
g = acceleration of gravity [m/s^2]
P = dynamic pressure [Pa]

With reference to Figure C-1 it is obvious that the problem is drastically simplified, but Equation (C-1) seems reasonable from a physical point of view since air bubbles may be present in the backfill after saturation. These bubbles will be compressed due to the pressure rise and cause a storage effect.

Following /Börgesson et al. 2006/, the hydraulic conductivity of the unsaturated backfill was related to the degree of saturation and the saturation is related to the retention curve. Following /Svensson 2010/, the specific storage of the unsaturated backfill was assumed to have a constant value and the specific storage of the saturated backfill another constant value. Moreover, the backfill is considered saturated as soon as the pressure turned positive. At that instant, the value of the specific storage was switched from an unsaturated value to a saturated. It is noted that with this definition of the specific storage, non-linear capillary suction effects of the unsaturated material are not taken into account.

C.5 Application to a final repository at Forsmark

For the sake of the work reported here, the attempted simplification is applied to a final repository at Forsmark. For the simulations, a number of assumptions are made.

- The layout of the repository is simplified (no central area, ramps, ventilation shafts or deposition holes), see Figure C-2.
- The simulation of the saturation process is adapted to the three stages of operation, A–C, see Figure C-2. For each stage, the computational grid is set up to form a box around the corresponding part of the repository. That is, it is assumed that the saturation of the three stages does not interfere.
- A constant fluid density is assumed (freshwater) and hydrostatic pressure is fixed at all boundaries. The domain boundaries are at least 100 m away from the repository.
- The cell size inside the tunnels is set to 1 m. In total, the computational grid consisted of about 2.5 million cells.
- The volume inside the tunnels varied somewhat between the three stages, but is on the average c $3 \cdot 10^5$ m^3.
- The properties of the backfilling material is assumed to be similar to those of Friedland Clay /Börgesson et al. 2006/.

Based on the above assumptions, the unsaturated pore volume at the start of the saturation process is estimated to 4-4.1 m^3/m of tunnel.

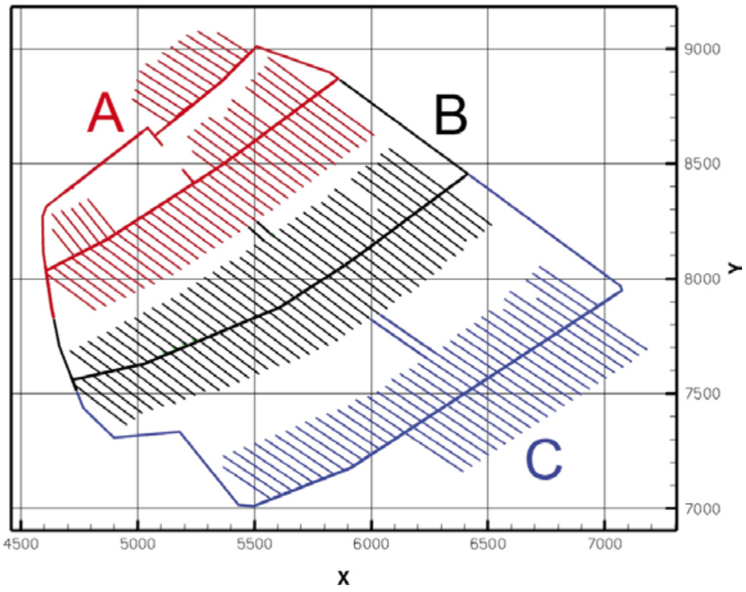

Figure C-2. *A simplified layout is used (no central area, ramp, ventilation shafts or deposition holes). The simulation of the saturation process is adapted to the three stages of operation, A–C. For each stage, the computational grid is set up to form a box around the corresponding part of the repository. The y-axis points towards north.*

C.6 Results

The simulated pressure build-up following the closure of the deposition tunnels for the three stages, A–C, is shown in Figure C-3, Figure C-4 and Figure C-5. The plots shown in these figures display the pressure at two time slices, 100 days and 10 years.

The impression from Figure C-3, Figure C-4 and Figure C-5 is that the backfill is saturated fairly quickly where a fracture crosses the tunnel, while other parts are still unaffected after 10 years.

The simulation time for stage A is extended to 100 years and a more detailed analysis is carried out. The inflow and accumulated inflow is shown in Figure C-6. It is found that the total inflow rate is around 0.01 L/s for a long period and the tunnel is not fully saturated after 100 years. Figure C-7 shows the fraction of the tunnel volume that was saturated as a function of time. The pressure distribution after 100 years of saturation is also shown in Figure C-7.

Pressure and flow vectors as mapped on the tunnel walls are shown in Figure C-8. The flow vectors show that water flows from the saturated parts towards the saturation front. It is hence an axial saturation of the tunnels.

Figure C-7 suggests that there is a spatial variability in the saturation rate after 100 years. Figure C-9 shows a close up of the view in Figure C-3 that shows the saturation after 100 days. In Figure C-9, three areas are identified with different saturation rates; slow, intermediate and fast. Although the method used in this work to model the saturation process is approximate, it is decided to model the saturation of the three subareas in greater detail using a local model domain around each subarea. The simulation had to use a very small time step and is stopped after about 170 years. The plot in Figure C-10 suggests that all subareas are more or less completely saturated after about 200 years.

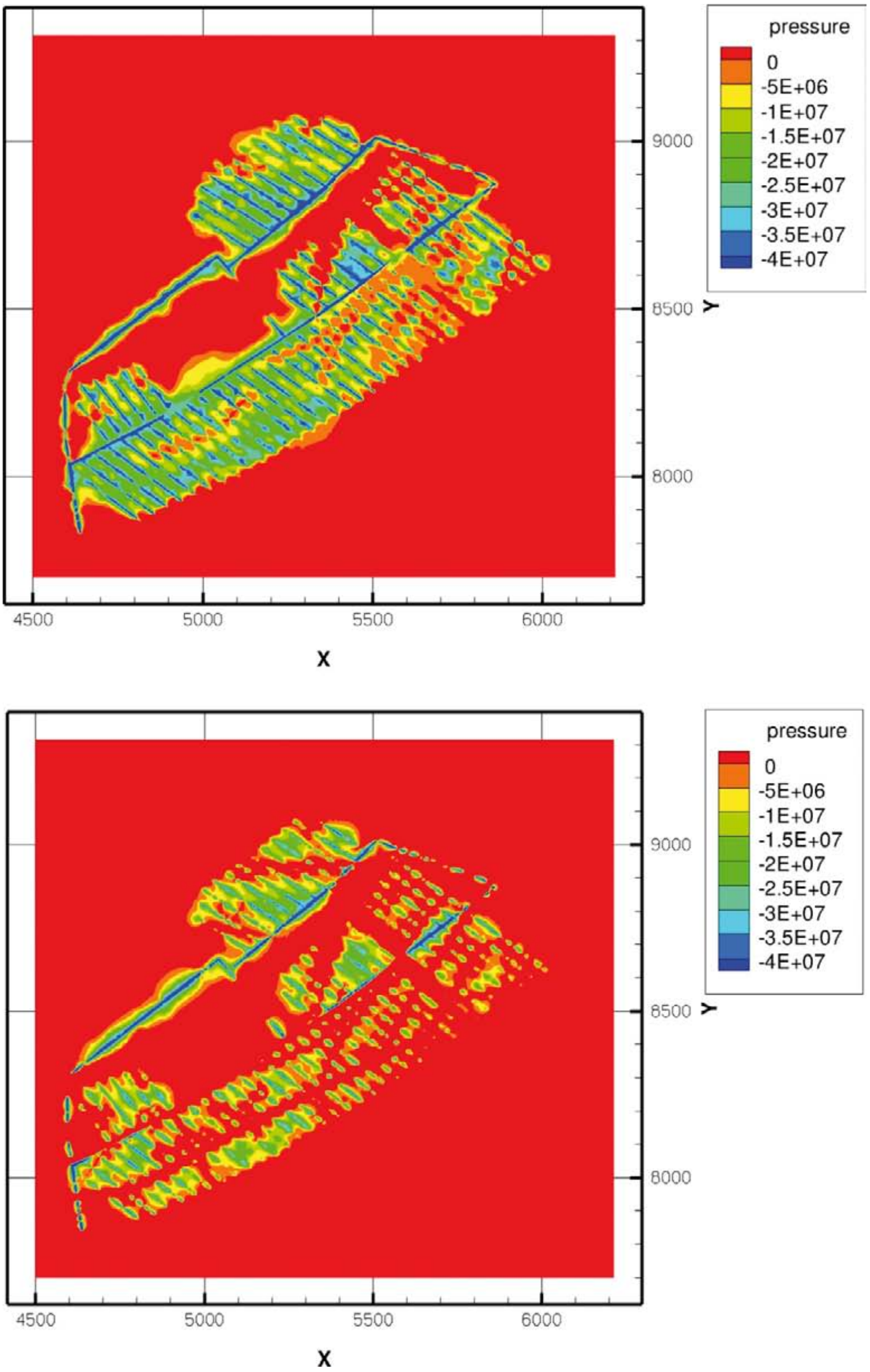

Figure C-3. *Gauge pressure distribution (in Pa) after closure of stage A; 100 days (top) and 10 years. A red colour means full saturation. The y-axis points towards north.*

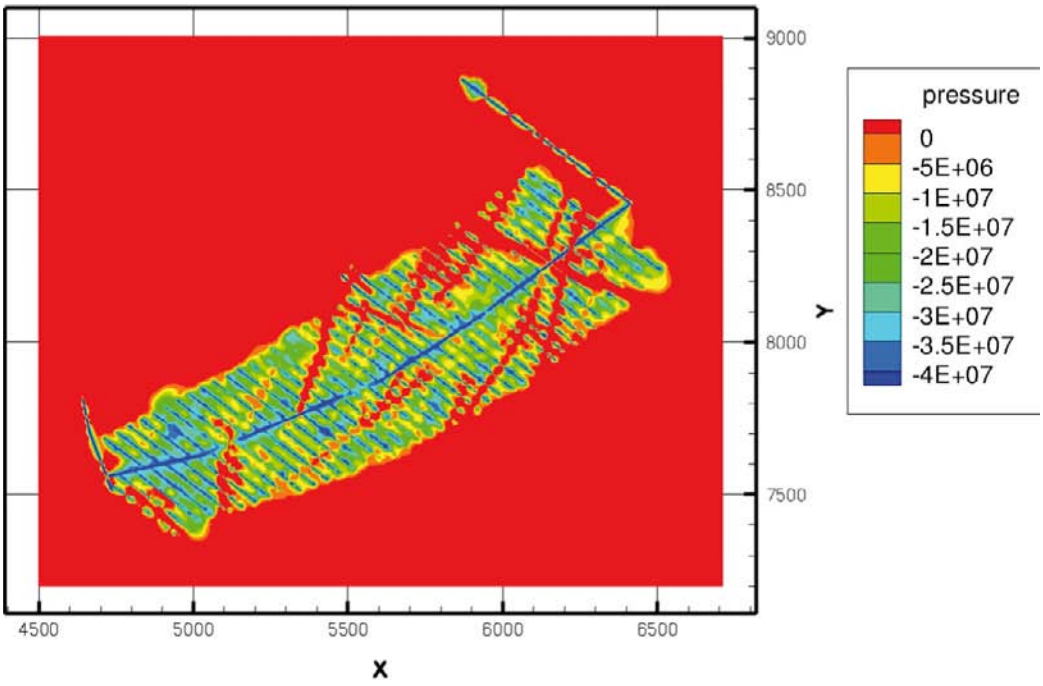

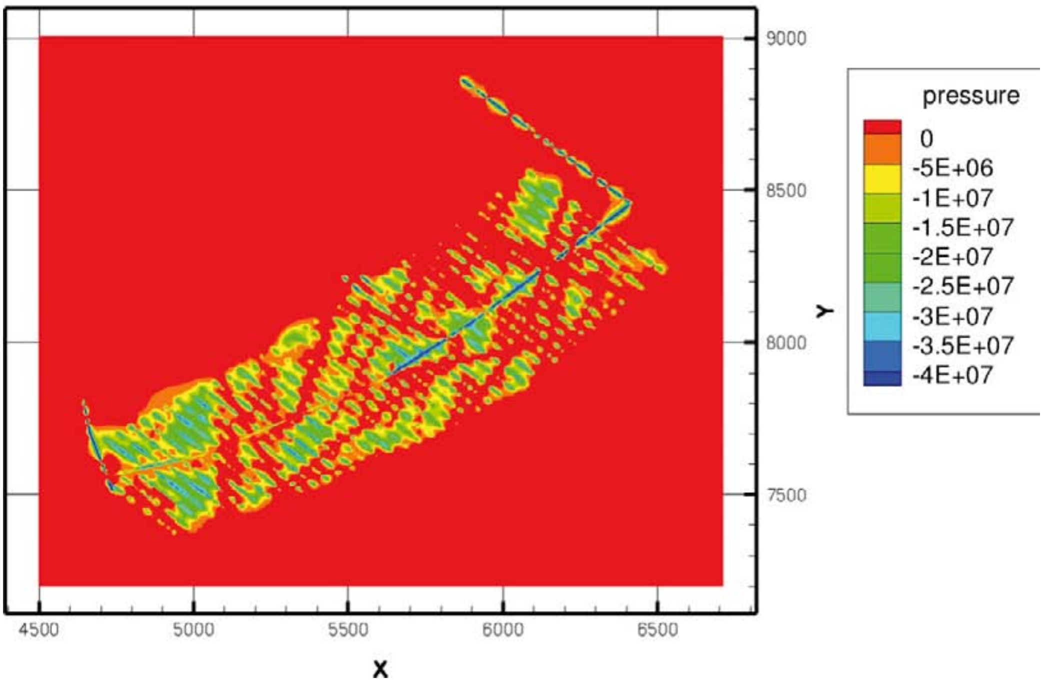

Figure C-4. *Gauge pressure distribution (in Pa) after closure of stage B; 100 days (top) and 10 years. A red colour means full saturation. The y-axis points towards north.*

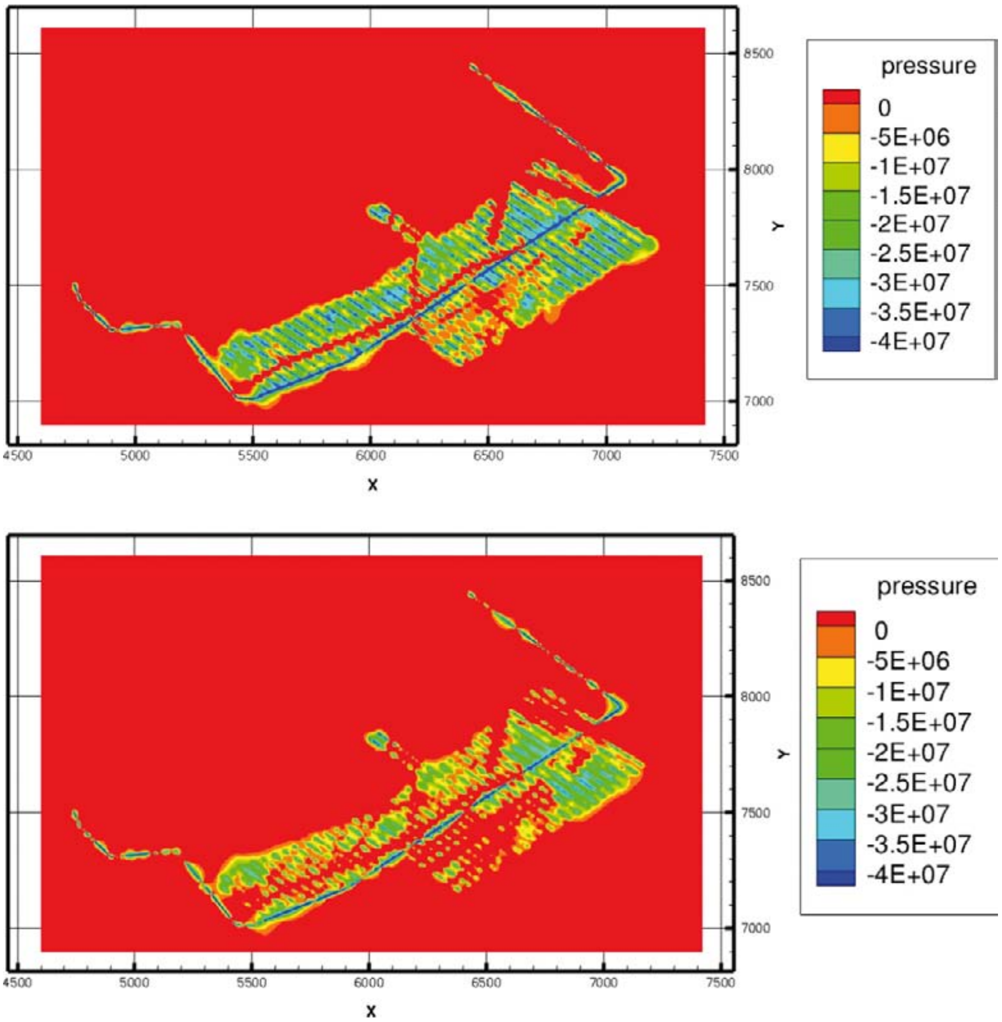

Figure C-5. *Gauge pressure distribution (in Pa) after closure of stage C; 100 days (top) and 10 years. A red colour means full saturation. The y-axis points towards north.*

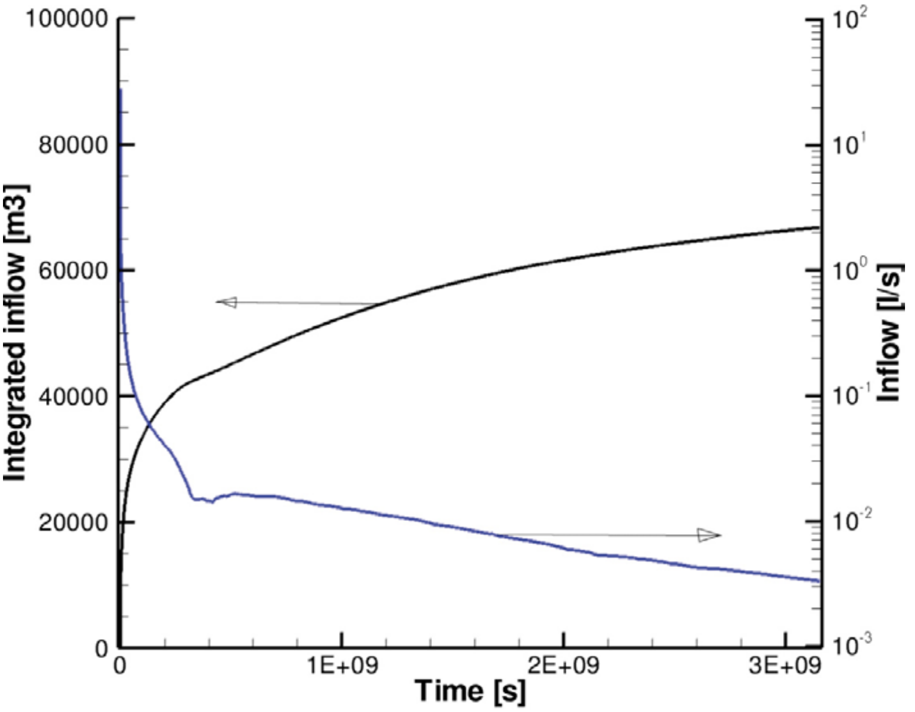

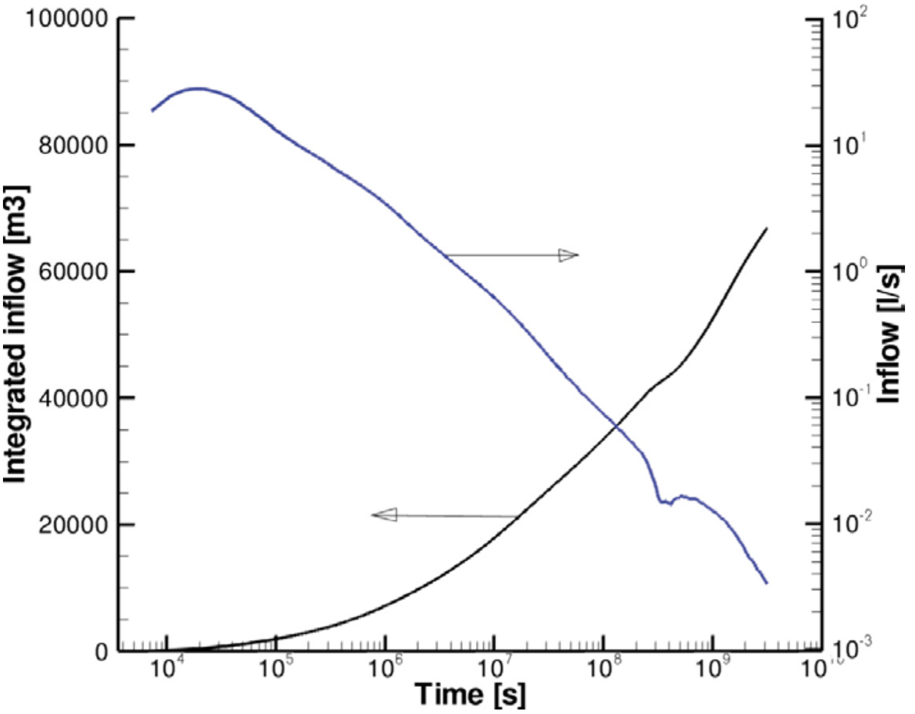

Figure C-6. *Inflow rate [L/s] and cumulate inflow [m^3] for stage A with a linear (top) and logarithmic time scale. The pertubation seen in the blue graph occurs at about 10–15 years after closure and is a model effect caused by the change in specific storage when the unsaturated backfill becomes saturated. One year is about 31.5·10^6 s.*

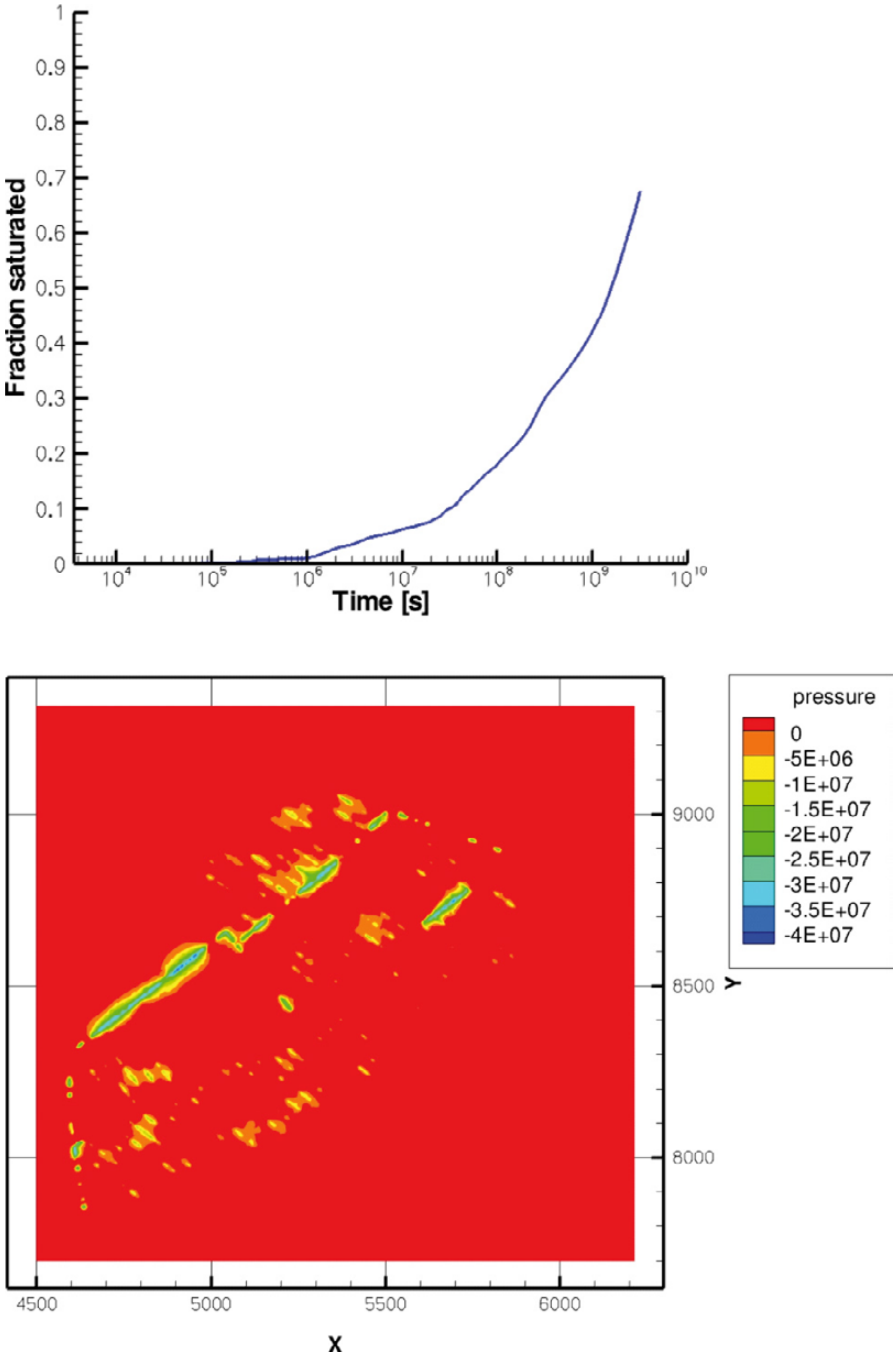

Figure C-7. The fraction of the tunnel volume that is saturated as a function of time (top) and the gauge pressure distribution for stage A after 100 years of saturation. The y-axis points towards north.

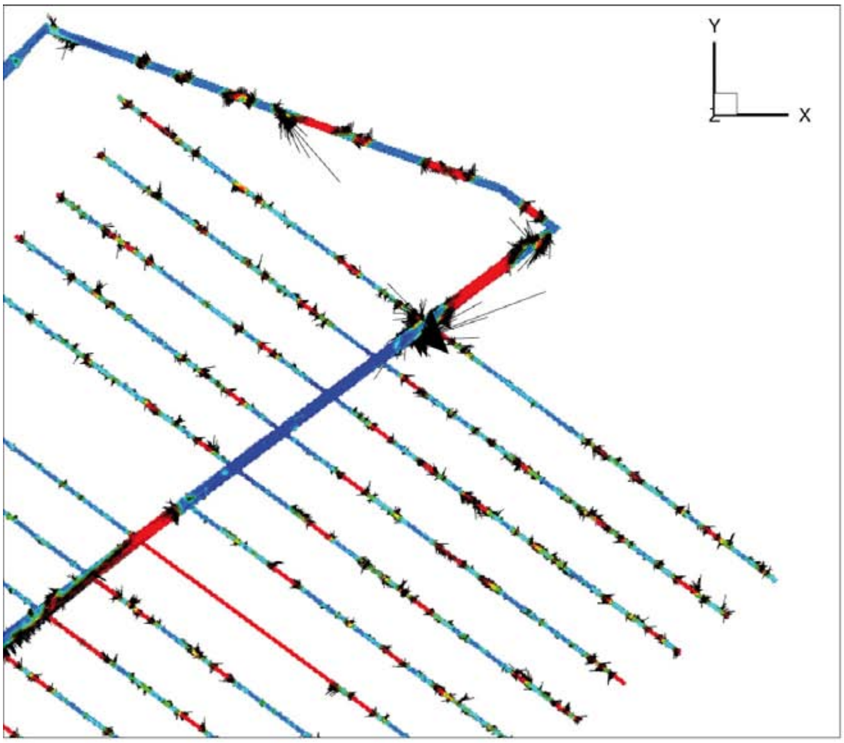

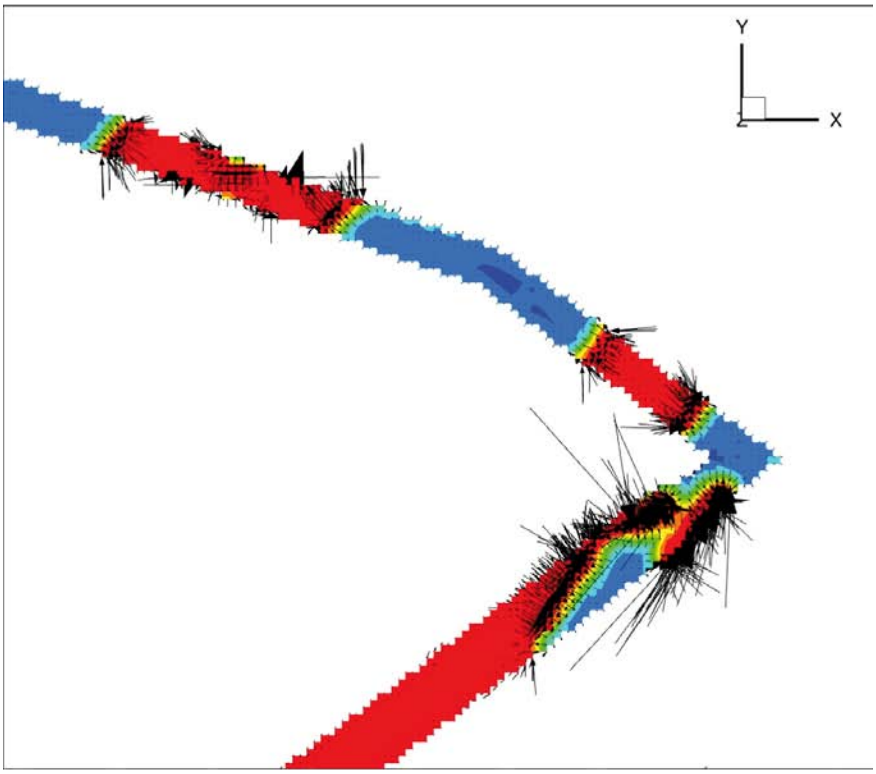

Figure C-8. *Pressure (colours) and flow vectors mapped on the tunnel walls. Red colour indicates saturated conditions, while blue parts are unsaturated. The upper plot shows the eastern part of the area associated with stage A. The lower plot is a close-up. The y-axis points towards north.*

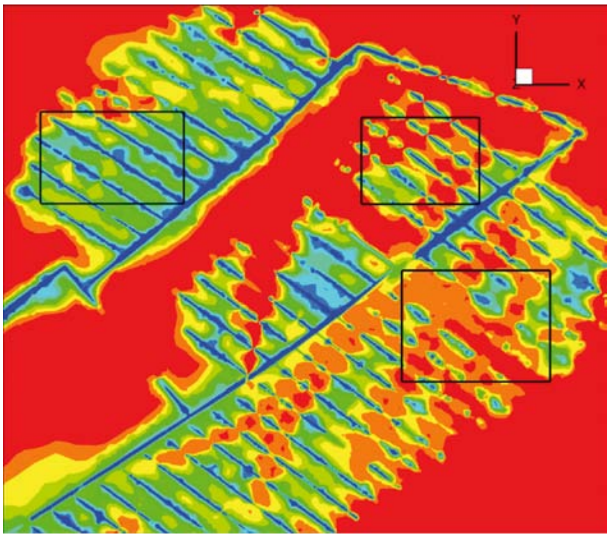

Figure C-9. *Close up view of the gauge pressure distribution (in Pa) after closure of stage A; 100 days. A red colour means full saturation. Three areas with different saturation rates are marked ups; upper left rectangle: slow saturation rate, upper right rectangle: intermediate saturation rate, and lower right rectangle: fast saturation rate.*

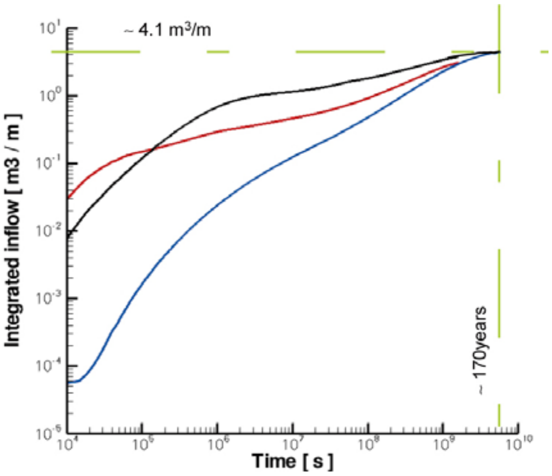

Figure C-10. *Cumulative inflow in m*^{3} *per metre of tunnel as a function of time after closure for the three areas shown in Figure C-9. Blue curve = area with a slower saturation rate, Red curve = area with an intermediate saturation rate, and Black curve = area with a faster saturation rate.*

C.7 Discussion and conclusions

A few observations can be made from the simulations carried out in this appendix.

- The approximate method for modelling the hydration process of an unsaturated backfill in a fractured medium suggested by /Svensson 2010/ works well computationally.
- The simulations reported here indicate that the backfill is saturated fairly quickly at those locations where a fracture crosses the tunnel (radial saturation). Where there are no fracture intersections, the saturation process progresses along the tunnel (axial saturation). No account was made for a crown space, excavated damage zone or other hydraulic imperfections. If such features are included, the saturation process most likely progresses more rapidly.
- The total time scale for the hydration process is probably at least 200 years. It is presently not possible to be more specific about the time scale.

It should be noted that the simplifications invoked by the approximate method call for further systematic studies before any firm conclusions about the hydration time can be drawn. For example, it is presently not clear how various processes and parameter values may influence the results. Capillary suction is one example of a physical process that is simplistically treated in the work reported here. Another example is the effect of the minimum value used for the hydraulic conductivity of the intact bedrock. In most groundwater flow simulations that use a continuum model, the minimum hydraulic conductivity of the intact (non-fractured) bedrock is set to c 10^{-10} m/s. For the present simulation, however, it was found that this value has to be reduced to 10^{-13} m/s, otherwise it controls the saturation time.

D SFR

D.1 Introduction

A simultaneous operation of a final repository for spent nuclear fuel at Forsmark and SFR is considered a likely scenario for a short period of time. SFR is located c 1 km north of the investigated candidate area for a final repository, see Figure 1-5. Figure D-1 shows a visualisation of the two repositories and the HCD model at Forsmark handled in the base case setup (cf Figure 4-4). In the work reported here, we considered the present-day layout of SFR as well as a planned extension of SFR, see Figure D-2. It should be noted that the final layout of the extension of SFR is undecided at the time of the work reported here and that the layout used is a working hypothesis. The final layout is expected to be the same in terms of design (facilities and volumes) but may differ a little in terms of its positioning (coordinates).

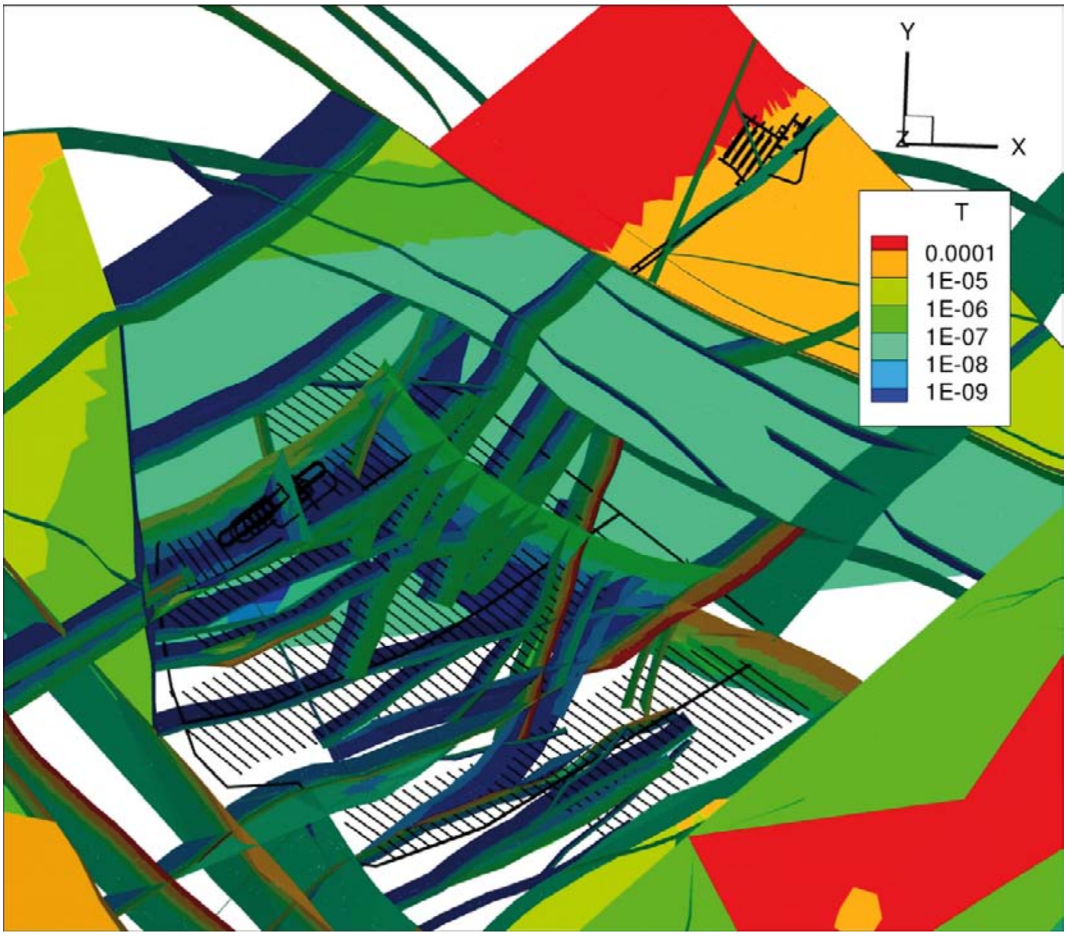

Figure D-1. *View showing a final repository for spent nuclear fuel at Forsmark and SFR, the existing repository for short-lived radioactive waste nearby. The shortest distance between the two repositories is less than 1 km if the start of the ramp to SFR is taken into account. The y-axis points towards north. (The hydraulic properties of the deformation zones have homogeneous hydraulic properties with depth dependency according to Equation (2-1). (Some zones are deleted in this visualisation for the sake of visibility.)*

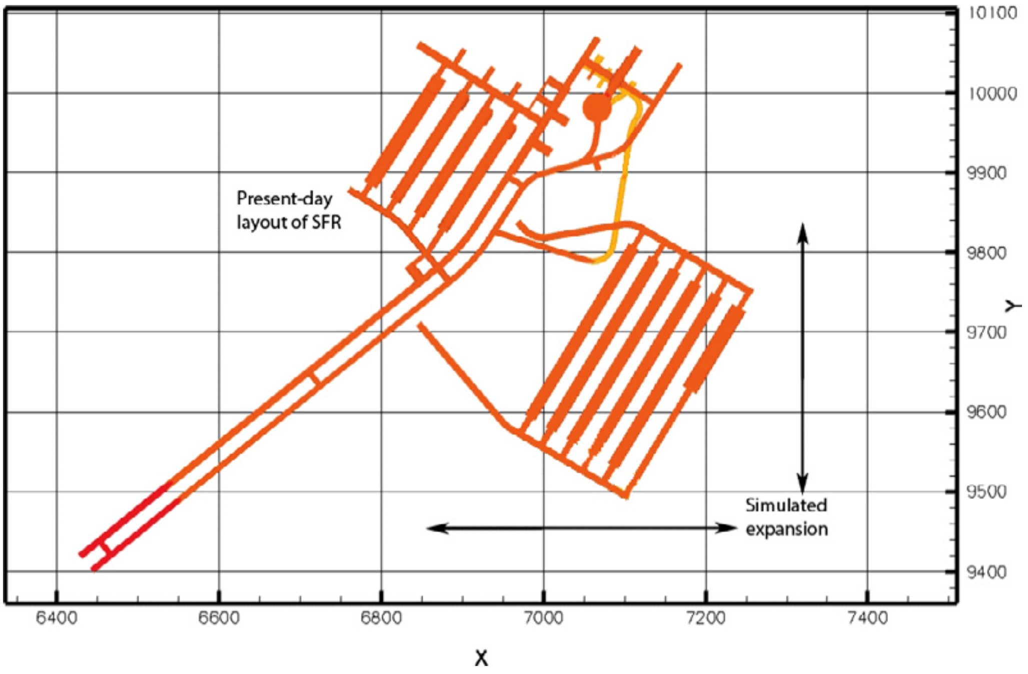

Figure D-2. *A view showing the simulated present-day layout of SFR together with the simulated tentative extension. The y-axis points towards north.*

D.2 Data for flow model calibration

The calibration of the flow model around SFR utilised three sorts of data.

- Measurements of the total inflow rate. The total inflow rate varies with time, but is in the range 4.8–6.0 L/s (not including the amount of water withdrawn through ventilation, which is unknown) /Follin et al. 2008, SKBdoc 1200954.
- Groundwater levels measured in boreholes at eleven different locations, see Figure D-3 and Table D-1.
- Available data of the performed grouting /Christiansson and Bolvede 1987/.

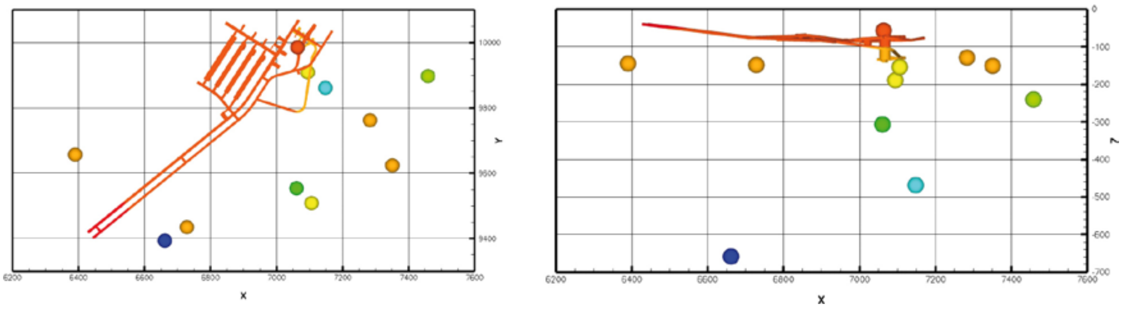

Figure D-3. *Two views showing the locations of the eleven measurement “points” around the present-day layout of SFR. The “points” are coloured by their elevation for the sake of simpler identification, see Table D-1. The y-axis points towards north.*

Table D-1. Compilation of groundwater levels measured in boreholes at eleven different locations. The sum of the "heads" at the measurement "points" is c 120 m. (Data archived in Sicada/HMS.)

Measurement	Northing	Easting	Elevation	Head (m)	x-model	y-model
HFR35:1	6701657.89	1632389.53	–143.88	–5.3	6389.53	9657.89
KFM11A:1	6701394.38	1632660.78	–657.90	–3.5	6660.78	9394.38
HFR105:1	6701435.83	1632727.35	–147.74	–10.9	6727.35	9435.83
KFR104:1	6701554.93	1633059.05	–306.17	–13.8	7059.05	9554.93
KFR105:1	6701509.54	1633104.58	–153.32	–1.3	7104.58	9509.54
KFR13:1	6701910.29	1633092.89	–188.52	–38.0	7092.89	9910.29
KFR19:1	6701986.76	1633062.20	–56.30	–39.0	7062.20	9986.76
KFR101:1	6701898.34	1633456.83	–239.90	–1.6	7456.83	9898.34
KFR102A:1	6701862.28	1633146.48	–468.03	–4.9	7146.48	9862.28
KFR102A:7	6701763.18	1633281.52	–128.26	–1.2	7281.52	9763.18

D.3 Sensitivity study

The simulated total inflow rate to SFR and the drawdown around SFR are compared with the measured data discussed in section D.2. Concerning grouting, an efficiency corresponding to level II is assumed (cf Table 4-3). Inflow rates and groundwater levels are studied for four main cases, A–B. For one these, four minor cases were looked at, B:1-B:4.

A. Before SFR, i.e. undisturbed groundwater levels before SFR is constructed.

B. Present-day SFR
   B:1. No grouting of SFR (i.e. what if there is no grouting carried out) using the hydrogeological model derived for SDM-Site, which assumed a homogeneous porous medium (CPM) for the HRD outside the investigated candidate area.
   B:2. Grouting of the largest inflows to SFR (cf. /Holmén and Stigsson 2001/) using the hydrogeological model derived for SDM-Site, which assumed a homogeneous porous medium (CPM) for the HRD outside the investigated candidate area.
   B:3. Same as in B:2 but with an extended Hydro-DFN model suggested by /Öhman and Follin 2010/ for the HRD outside the investigated candidate area. (see Case 5 in Section 4.3 and Section 5.6).
   B:4. Same as in B:3 but with a lower vertical hydraulic conductivity of the HSD below the Baltic Sea (see Case 6 in section 4.3 and Section 5.6).

C. Future 1: An open final repository and an extended SFR in operation.

D. Future 2: An open final repository and a closed extended SFR.

The simulation results are compiled in Table D-2. From these values it is concluded that grouting primarily affects the total inflow rate, whereas an improved modelling of the corresponding groundwater levels required that the flow model is based on an extended Hydro-DFN model and had a lower vertical hydraulic conductivity of the HSD below the Baltic Sea.

D.4 Discussion

Case A simulates the situation before SFR is constructed. The result suggests groundwater levels in the bedrock where SFR is located today that are slightly higher than the seal level before SFR is constructed. This observation is in agreement with field data and suggests that the area where SFR is located once was a discharge area /Holmén and Stigsson 2001/.

/Follin et al. 2007b/ discussed the possibility for a hydraulic influence of the present-day pumping at SFR on the groundwater levels in the northern part of the candidate area. The simulation results shown in Figure D-4 through Figure D-7 do not reject this hypothesis. However, the drawdown of the studied extension does not seem to be significantly different compared to that of the present-day SFR discussed in /Follin et al. 2008/.

Table D-2. Compilation of measured and simulated inflow rates and groundwater levels. It is recognised that the sum of the groundwater values is a very coarse quantity to evaluate the match since detailed differences are easily filtered. For the sake of the work reported here, which is focussed on finding important mechanisms, the lumped value is considered a sufficient quantity.

ID	Simulation	Grouting	CPM/ECPM	Sea HCD	Q-SFR	KFR 13:1	KFR 19.1	KFR 101:1	KFR 102A:1	KFR 102A:7	KFR 103:1	HFM 35:1	KFM 11A:1	HFR 105:1	KFR 104:1	KFR 105:1	Sum
	Present-day SFR				4.8-6.0	–38.0	–39.0	–1.6	–4.9	–1.2	–0.6	–5.3	–3.5	–10.9	–13.8	–1.2	–120.0
A	Before SFR	No	CPM	No/1E-6	–	+0.03	+0.03	+0.03	+0.04	+0.03	+0.03	+0.02	+0.08	+0.04	+0.04	+0.03	+0.40
B	Present-day SFR																
B-1	A non-grouted SFR	No	CPM	No/1E-6	86.5	–84	–56	–22	–35	–28	–13	–6	–11	–17	–29	–17	–318.0
B-2	A grouted SFR	Yes/1E-8	CPM	No/1E-6	6.0	–5.2	–8.6	–1.4	–2.2	–1.8	–0.9	–0.5	–0.8	–1.6	–2.3	–1.3	–26.6
B-3	B-2 + Ext. Hydro-DFN	Yes/1E-8	ECPM	No/1E-6	7.6	–7.0	–41.0	–3.0	–3.5	–4.9	–3.3	–0.8	–1.1	–2.3	–3.2	–3.0	–73.1
B-4	B-3 + Sea HSD	Yes/1E-8	ECPM	Yes/1E-8	6.9	–11.9	–43.0	–6.2	–7.2	–8.8	–6.4	–2.9	–2.3	–4.7	–6.0	–5.6	–105.0
C	An open final repository and an open extended SFR	Yes/1E-8	ECPM	Yes/1E-8	7.3	–12.5	–43.2	–6.9	–9.4	–10.5	–7.6	–3.2	–16.2	–5.3	–8.2	–6.9	–129.9
D	An open final repository and an a closed extended SFR	Yes/1E-8	ECPM	Yes/1E-8	0.0	–0.2	–0.1	–0.2	–1.9	–0.2	–0.3	–0.3	–13.9	–0.5	–1.8	–0.4	–19.8

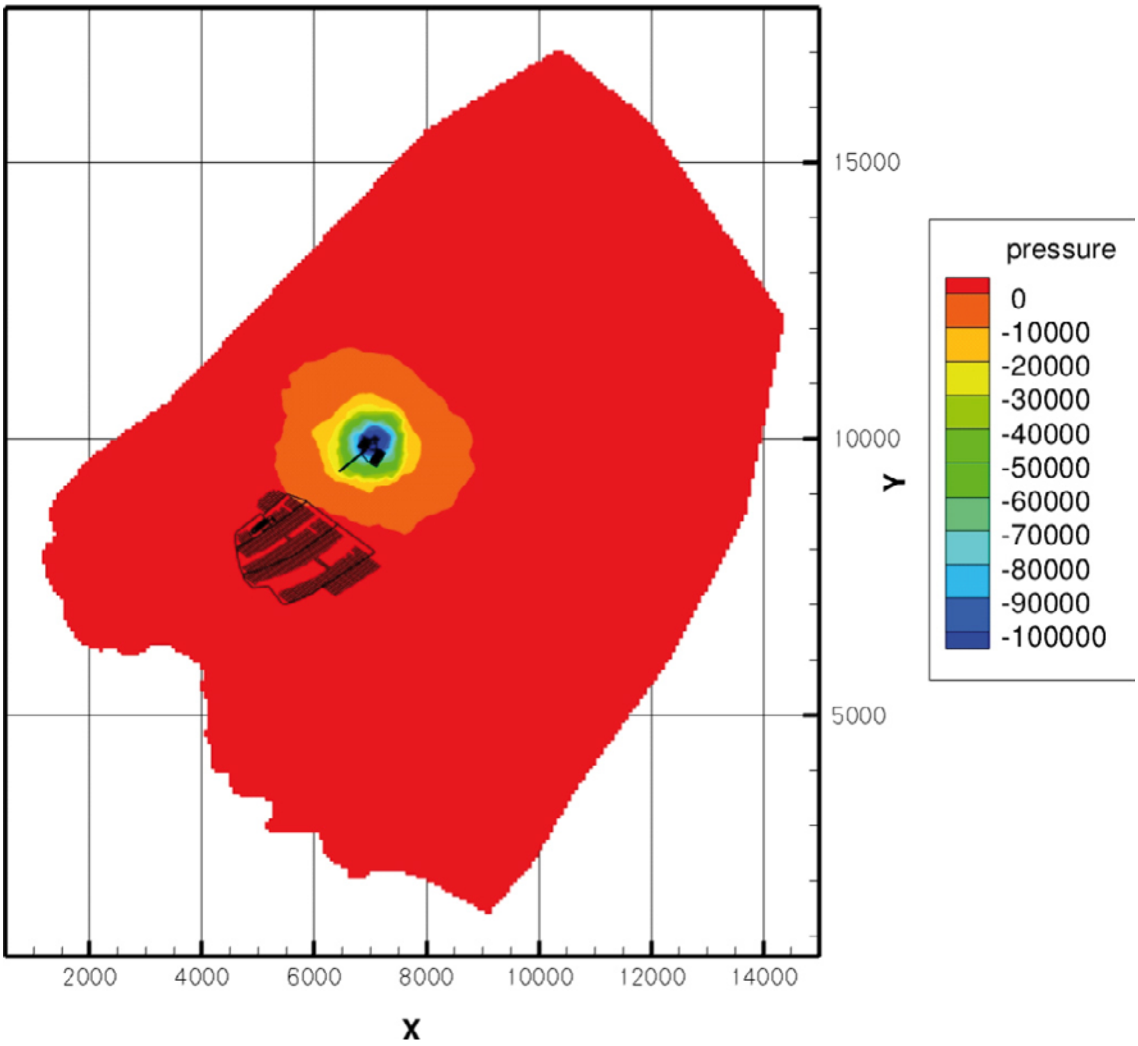

Figure D-4. *Example visualisation showing the radius of influence at –150 m elevation for an extended SFR in operation. The chosen starting positions of the backward tracking trajectories have inflow rates greater than 0.1 L/min. The y-axis points towards north.*

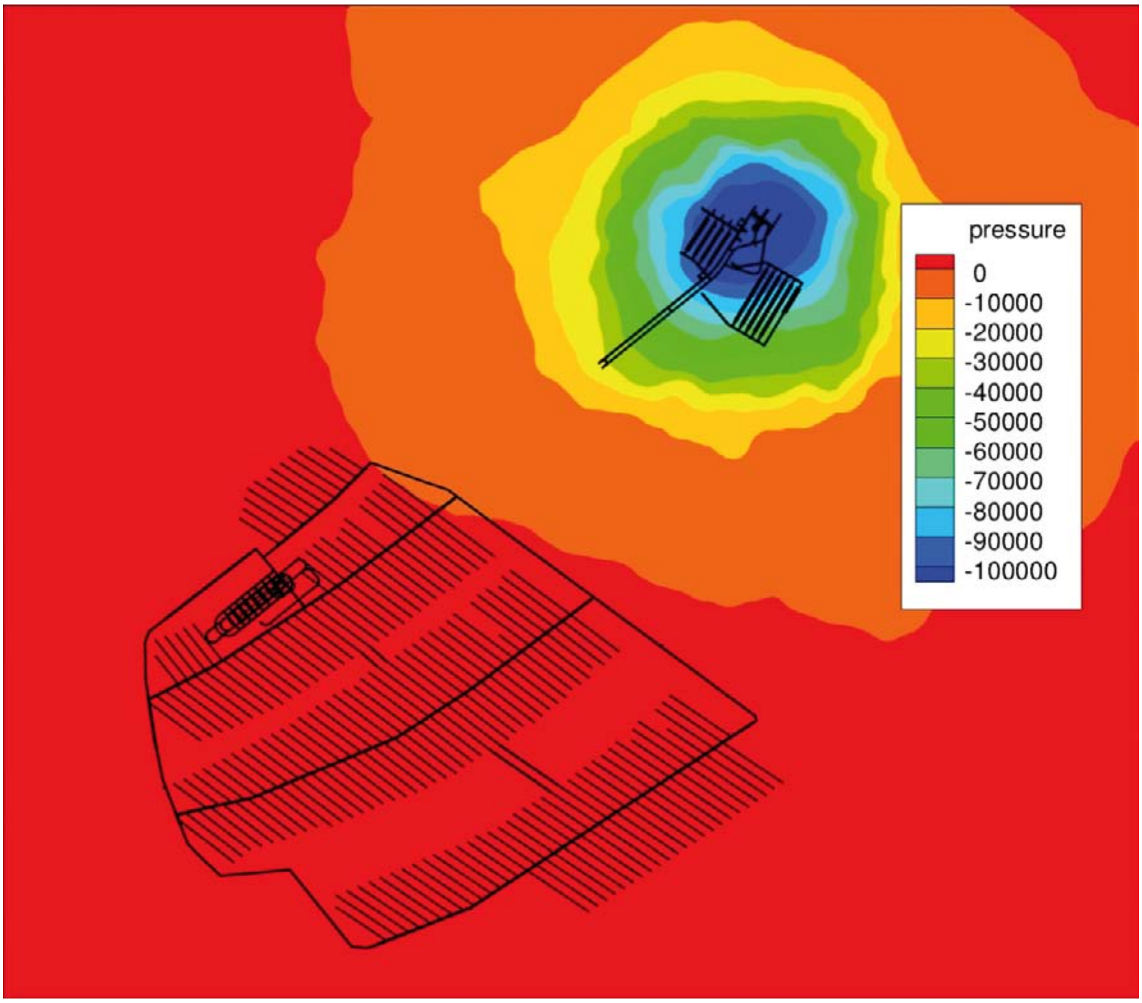

Figure D-5. *Example visualisation showing the radius of influence at –150 m elevation for an extended SFR in operation. Close-up of the plot shown in Figure D-4.*

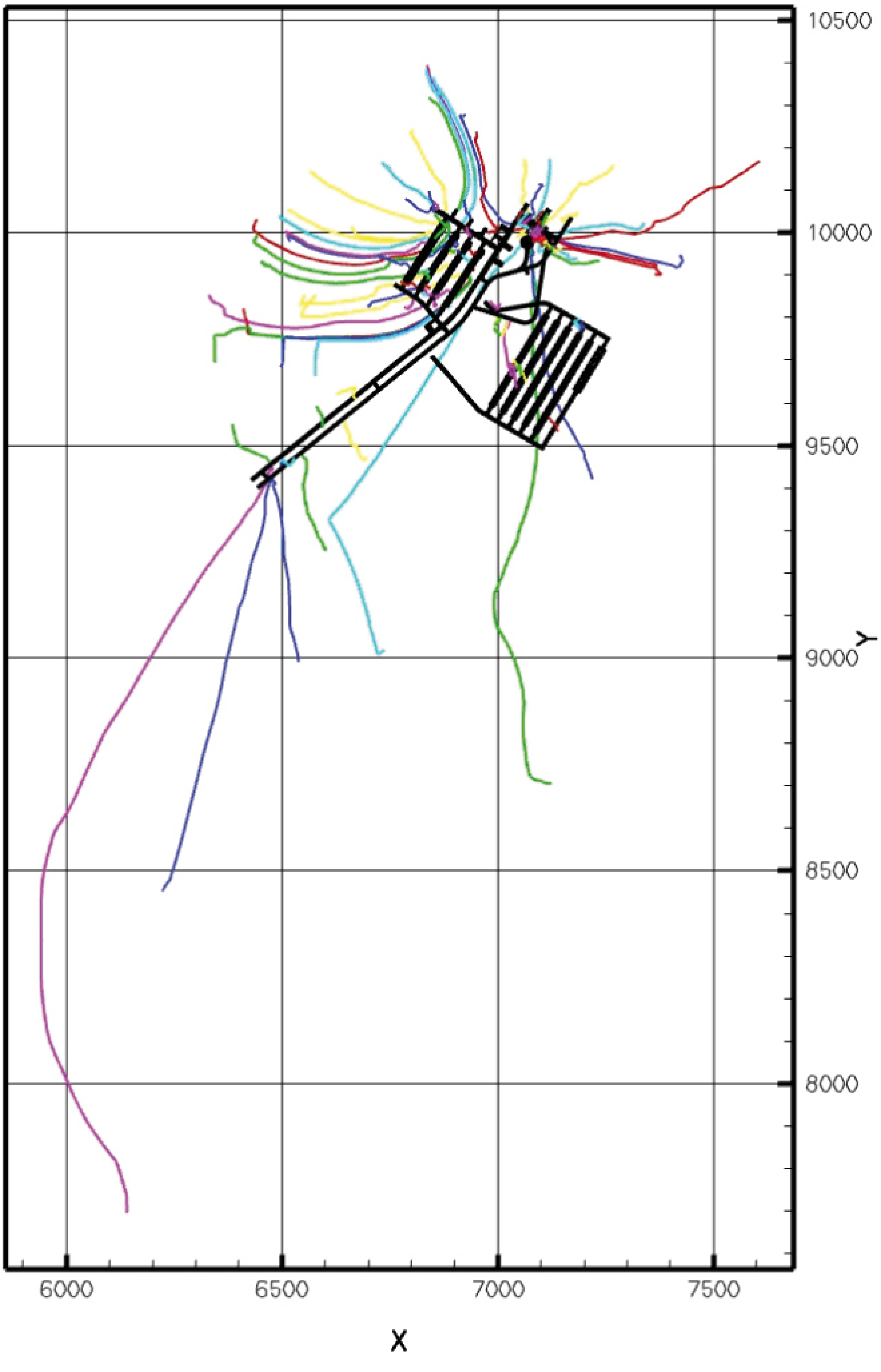

Figure D-6. *Example visualisation showing particle trajectories in a horizontal plane. The chosen starting positions of the backward tracking trajectories had inflow rates greater than 0.1 L/min. The y-axis points towards north.*

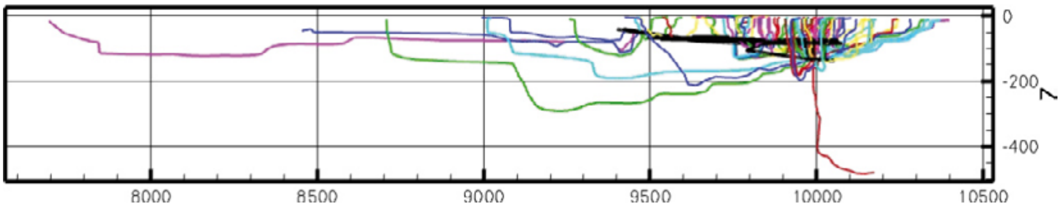

Figure D-7. *Example visualisation showing particle trajectories in a vertical cross-section. The chosen starting positions of the backward tracking trajectories had inflow rates greater than 0.1 L/min. The y-axis points towards north.*

Appendix E

Equivalent discontinuous porous medium

E.1 Introduction

The results reported in Chapter 5 are based on the equivalent continuous porous medium (ECPM) approach. The term “continuous” refers to an unbroken spatial arrangement of porous medium (continuum) type hydraulic properties. In the ECPM approach, grid cells not intersected by flowing fractures are assigned minimum values of the hydraulic conductivity and the kinematic porosity. The values used in this work are shown in Table 4-1.

If at all possible, grid cell without fractures should represent intact rock, i.e. a crystalline matrix without fractures. Hydraulic tests on presumably intact rock cores from Forsmark reveal hydraulic conductivities that are about three orders of magnitude lower than the minimum value shown in Table 4-1 /Vilks 2007, Follin et al. 2007a/. Such low values of the matrix permeability are not possible to use in the numerical flow model without computational constraints.

This appendix presents a modelling approach where grid cells not intersected by fractures are removed from the computational grid rather than giving them arbitrary low values as in the ECPM approach. In operation, this prohibits advective flow through patches of non-fractured rock as the hydraulic gradients accommodate to the imposed internal no-flow boundaries. The approach to remove grid cells of low permeability is not new, e.g. /Follin 1992/ applied the approach while studying groundwater flow and particle tracking in heterogeneous fracture planes.

Removing grid cells not intersected by fractures significantly reduces the number of grid cells in sparsely fractured rocks, and this relaxation allows for a finer resolution of the remaining computational grid, i.e. more small grid cells where fractures do occur, and hence improved flow solutions. Obviously, the ultimate optimisation of removing and refining the computational grid will result in a discretisation that is conditioned on the discrete fracture network (DFN). To distinguish the elaborated modelling approach from the ECPM approach and the DFN approach, the acronym EDPM is used in the work reported here, meaning equivalent discontinuous porous medium.

Figure E-1 shows the computational grid around the repository as used in the ECPM flow simulations reported in Chapter 5. The smallest grid size in this model is 4 m. In comparison, Figure E-2 shows the computational grid around the repository as used in the EDPM flow simulations reported in this appendix. White areas represent regions where the initial grid cells are not intersected by fractures. The smallest grid size in this model is 0.5 m.

E.2 Detailed visualisation of the EDPM approach

The image in Figure E-3 shows an example view with a deposition tunnel and a few deposition holes. The intersecting fractures belong to a network of connected open fractures, i.e. flowing fractures. The work reported here studies the flow rates to the tunnel and the deposition hole during excavation and operation. In comparison, /Joyce et al. 2010/ study the flow (Darcy fluxes) and transport properties (flow-related transport resistances) under saturated temperate climate conditions.

The image in Figure E-4 shows the computational grid cells that is the result of the EDPM approach when the Q1 criterion is applied (see Section 4.2 for the definitions of the Q1 criterion). Computational grid exists only where there are fractures. As it appears in the image, there are also grid cells that are not in contact with the fractures. However, this is not correct as the thickness of the fractures is not displayed in the image. In the work reported here, each fracture is assigned an arbitrary thickness of one metre.

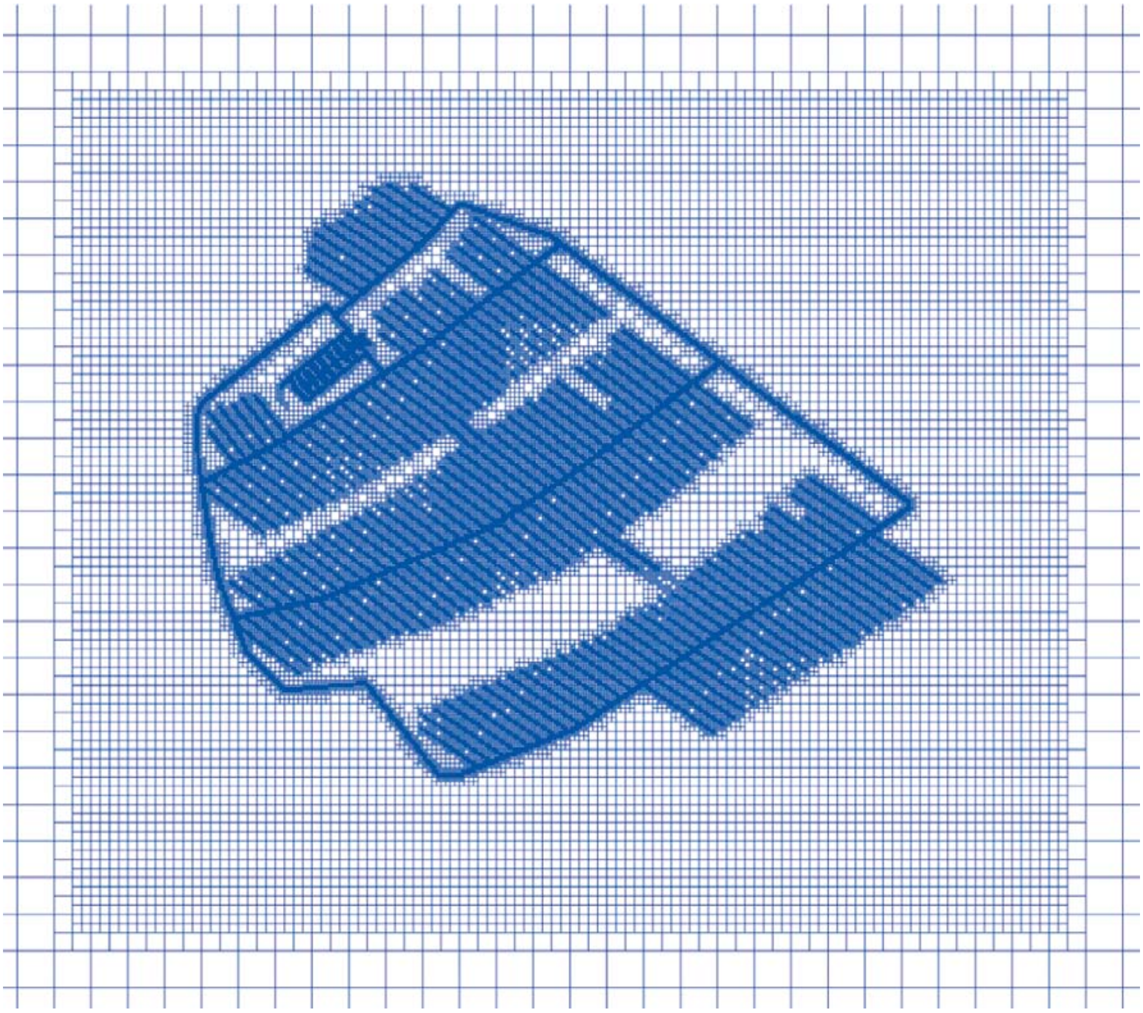

Figure E-1. *Plane view of the computational grid in proximity of the repository at –465 m elevation using the ECPM approach. The discretisation around the repository is refined using an unstructured grid. The smallest grid size in this model is 4 m.*

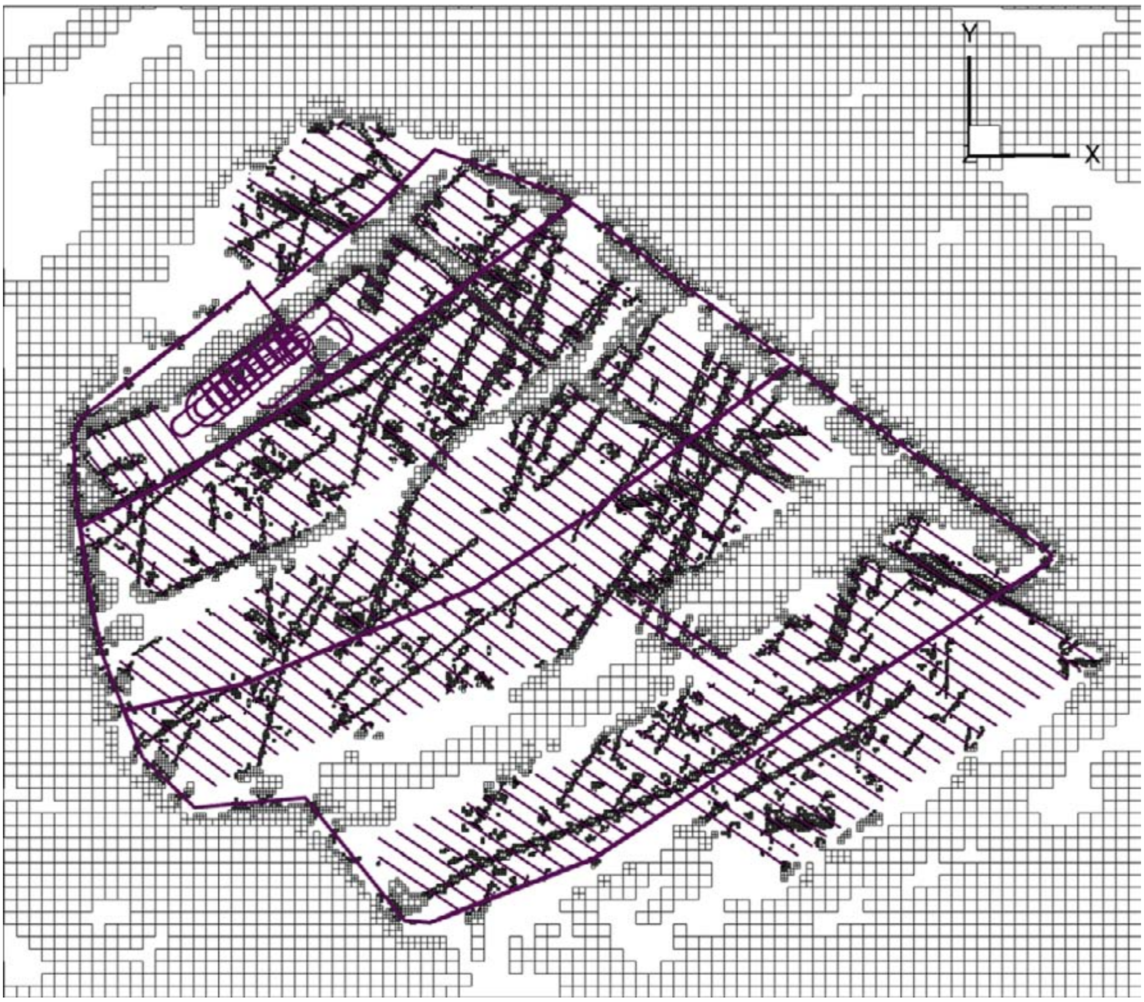

Figure E-2. *Plane view of the computational grid in proximity of the repository at –472 m elevation using the EDPM approach. The discretisation around the repository is refined using an unstructured grid. The smallest grid size in this model is 0.5 m.*

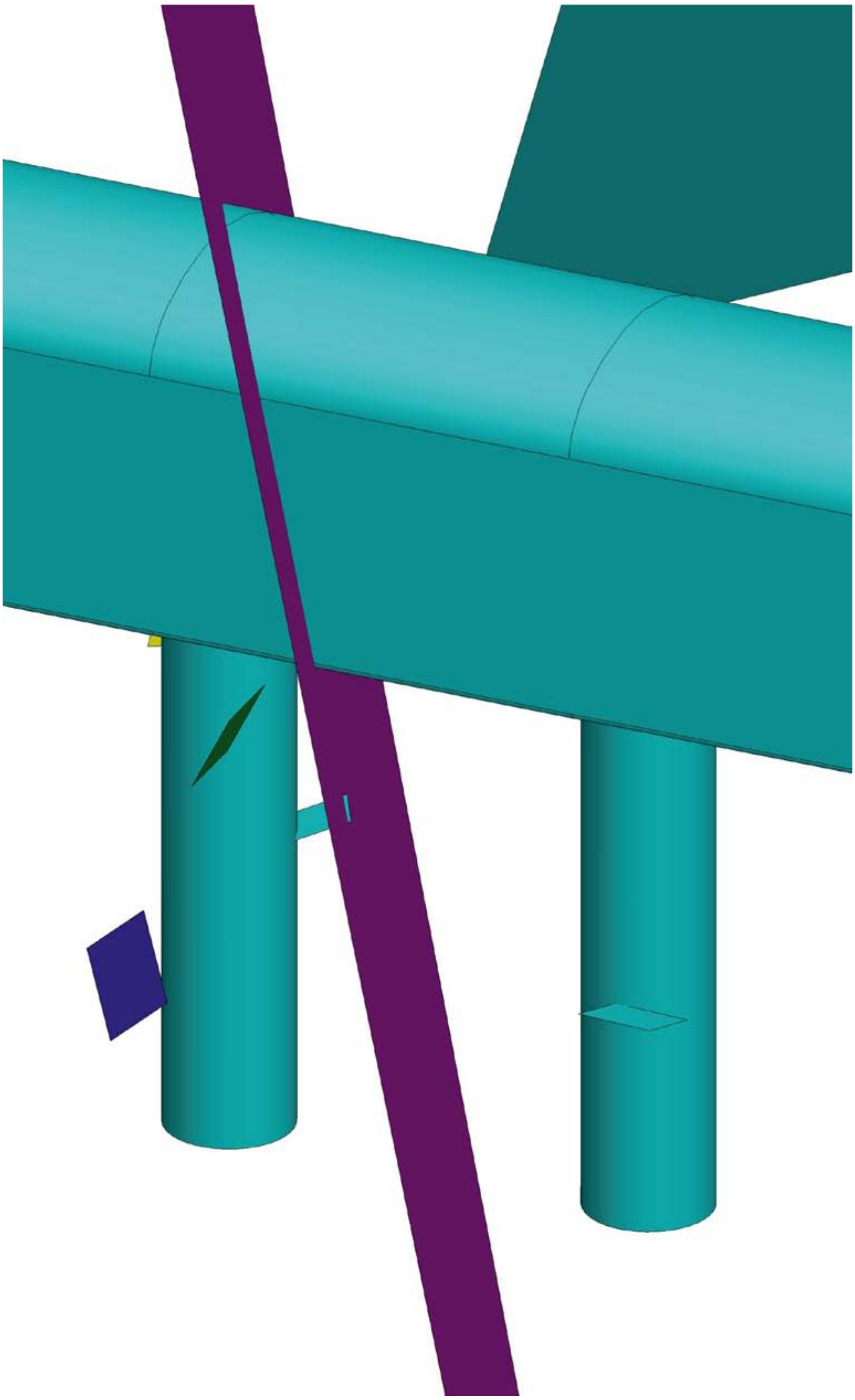

Figure E-3. Example view with a deposition tunnel and a two deposition holes. The intersecting fractures belong to a network of connected open fractures, i.e. flowing fractures.

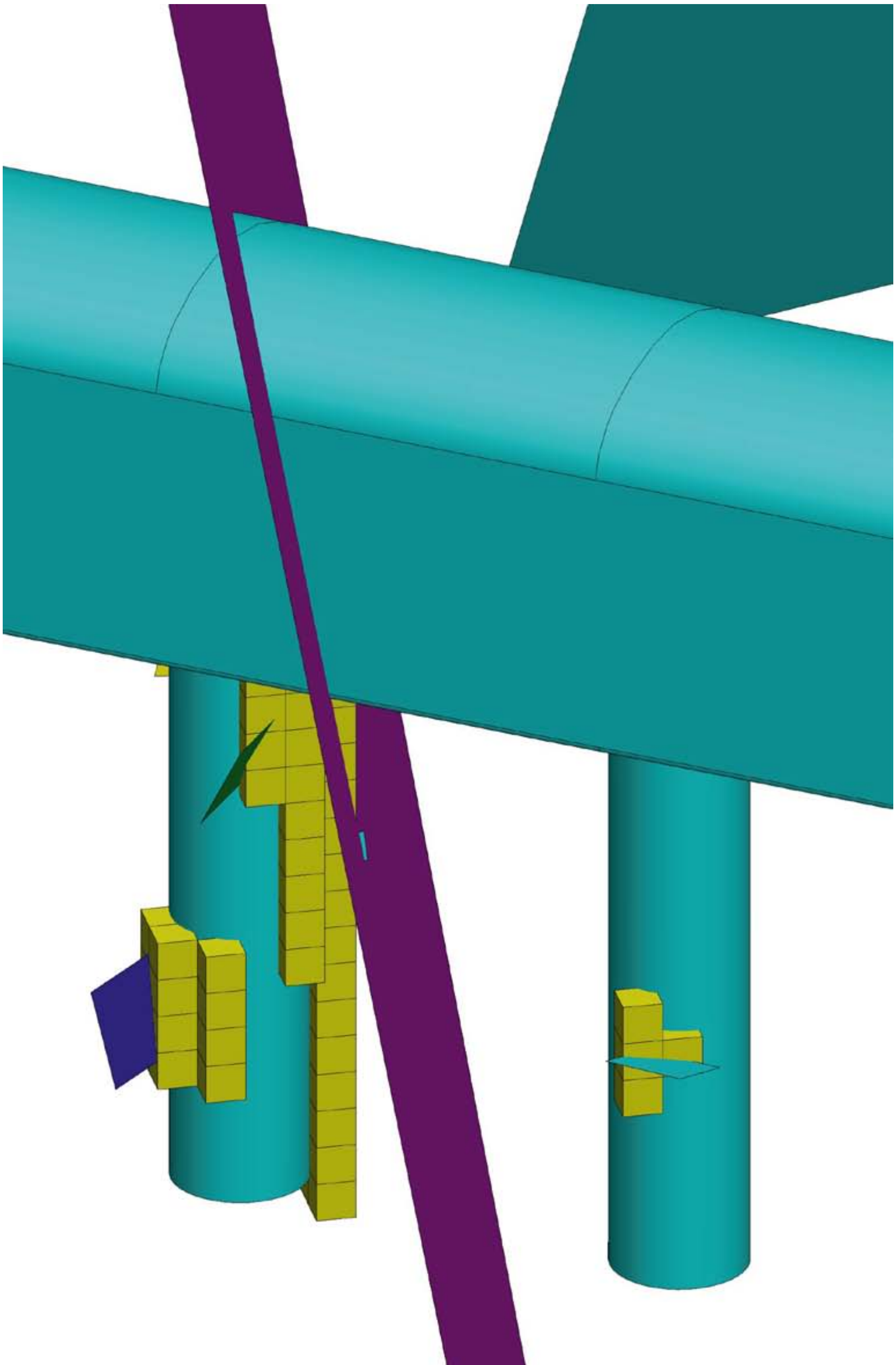

***Figure E-4.** The same image as in Figure E-3 combined with the computation grid cells that is the result of the EDPM approach when the Q1 criterion is applied (see Section 4.2 for the definitions of the Q1 criterion).*

E.3 Comparison of the ECPM and EDPM approaches

According to the design premises /SKB 2009/, the total volume of water flowing into a deposition hole, for the time between when the buffer is exposed to inflowing water and saturation, should be limited to ensure that no more than 100 kg of the initially deposited buffer material is lost due to piping/erosion. This implies, according to the present knowledge, that this total volume of water flowing into an accepted deposition hole must be less than 150 m^3. It is judged that this design premise is met provided that the specified inflow criteria, Q1, Q2 and "Q1 or Q2", are me (see section 4.2 for the definitions of the inflow criteria).

Below, the inflow rejection criteria are studied for the base case realisation using two types of equivalent porous media models, the traditional ECPM approach and the elaborated EDPM approach.

As shown in Chapter 5, the modelling with the ECPM approach suggest that 157 deposition holes fail the Q1 criterion, 867 fail the Q2 criterion, and 874 deposition holes fail the combined criterion "Q1 or Q2". Thus, the Q2 criterion is responsible for the majority of the failing deposition hole positions using the ECPM approach. Further,it is shown that that 121 deposition holes fail both the combined "Q1 or Q2" criterion and the "FPC or EFPC" criteria /Munier 2006/).

The corresponding results for the EDPM approach are : 88 fail the Q1 criterion, 368 fail the Q2 criterion and 372 fail the combined criterion "Q1 or Q2". Also, it is shown that 141 deposition holes fail both the combined "Q1 or Q2" criterion and the "FPC or EFPC" criterion. Since one would expect the deposition holes failing the "Q1 or Q2" criterion to be correlated to the holes failing also the "FPC or EFPC" criterion, it is observed that there is a greater overlap between these groups for the EDPM approach (372 vs. 141) than for the ECPM approach (874 vs. 121). The ECPM approach simply identifies too many inflows according to the Q2 criterion.

In conclusion, less deposition hole positions fail the different inflow criteria if the sparsely fractures rock is treated as an equivalent discontinuous porous medium. Figure E-5 shows the 157 and 88 deposition hole positions (out of a total of 6,916) that fail inflow criterion Q1 using the two approaches for the base case realisation. It is noted that there appears to be substantial variability between realisations when number and location of deposition holes rejected by inflow criteria are considered. For instance, in the second realisation, 211 failing deposition hole positions are obtained (as compared to 157 in the first realisation) using the ECPM approach, and 144 failing deposition hole positions (as compared to 88 in the first realisation) using the EDPM approach. However, this variability between realisations is reasonable given the low geometric mean of the conductive fracture frequency and the strong impact of large random features.

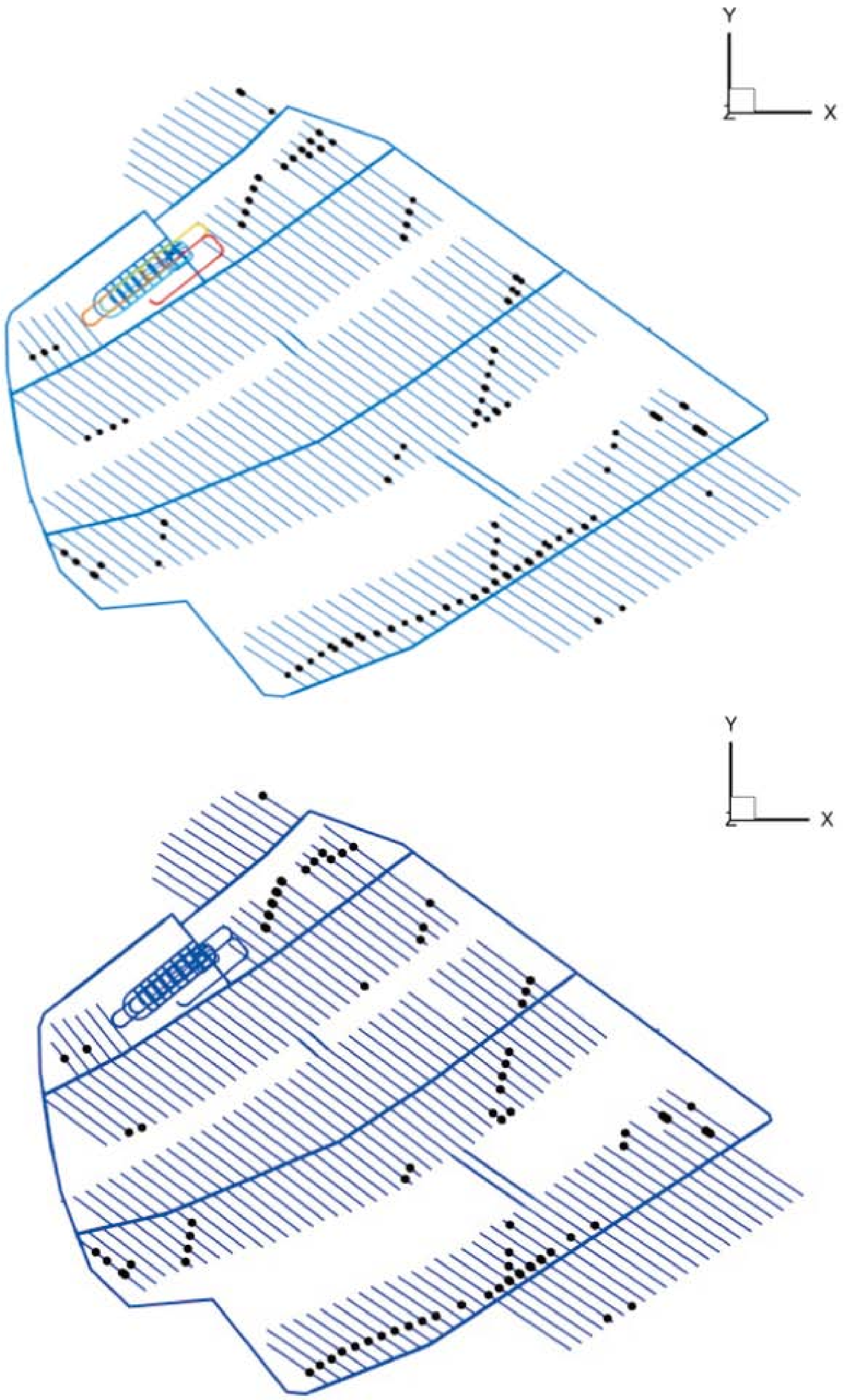

Figure E-5. *Top: Illustration of the 157 deposition hole positions that fail inflow criterion Q1 using the ECPM approach. Bottom: Illustration of the 88 deposition hole positions that fail inflow criterion Q1 using the EDPM approach. The plots look alike at a quick glance, but in the ECPM approach many positions that fail lie next to each other.*

Appendix F

Compilation of input files

Name of file in DarcyTools	Date	Name of file at delivery
HCD		
HCD	2008-10-08	081006_DZ_PFM_v22_SJ.zip
HCDcage	2008-10-08	081006_sheet_joints_v5.zip
HCDr2	2009-03-08	090220_DZ_PFM_REG_v22_SJ_r2._dt.zip
HRD		
set1to15.dat	2008-12-16	SRS-FFM01-6_v4.alterFinal_r1_sets1–15.asc.gz
set16to24.dat	2008-12-16	SRS-FFM01-6_v4.alterFinal_r1_sets16–24.asc.gz
set25to34.dat	2008-12-16	SRS-FFM01-6_v4.alterFinal_r1_sets25–34.asc.gz
set35to50.dat	2008-12-16	SRS-FFM01-6_v4.alterFinal_r1_sets35–50.asc.gz
set1to15r2.dat	2009-02-26	SRS-FFM01-6_v4.alterFinal_r2_sets1–15.asc.gz
set16to24r2.dat	2009-02-26	SRS-FFM01-6_v4.alterFinal_r2_sets16–24.asc.gz
set25to34r2.dat	2009-02-26	SRS-FFM01-6_v4.alterFinal_r2_sets25–34.asc.gz
set35to50r2.dat	2009-02-26	SRS-FFM01-6_v4.alterFinal_r2_sets35–50.asc.gz
DEM		
topxyz.dat	2007-08-17	PFM_F2.2.dem_medsjobatymetri_subarea_sorted.xyz (ASCII version of: SDEADM.UMEU_FM_4529, which is archived in SKB's GIS database as a GRID (raster) file with id C142.
riverlines.dat	2007-09-18	Floder_20m.dat
REPOSITORY LAYOUT		
26 stl files for layout geometry	2008-10-15	See the documentation by Tyréns
3 stl files for backfill saturation:		
scenario_1.stl	2008-12-19	senario_1.stl
scenario_2.stl	2008-12-23	senario_2.stl
scenario_3.stl	2008-12-27	senario_3.stl
OTHER GEOMETRIES		
WD.dat (Water Divide)	2007-09-03	hydrolinje2.stl
10 FFMxx.dat	2007-09-24	FFM*.stl
REJECTION CRITERIA		
RejCrit 20090223.dat	2009-02-20	090220_fs_Q1_2000_fpc.csv
13_scen1_4_DH.txt	2009-02-26	13_scenario1_DH.txt
		13_scenario2_DH_A.txt
		13_scenario2_DH_B.txt
		13_scenario3_DH.txt
		13_scenario4_DH.txt
13_scen1_4_DT.txt	2009-02-26	13_scenario1_DT.txt
		13_scenario2_DT_A.txt
		13_scenario2_DT_B.txt
		13_scenario3_DT.txt
		13_scenario4_DT.txt
		13_scenario4_DT.txt
SFR REPOSITORY LAYOUT		
layout091126.stl	2009-12-23	layout d0 mycket grovt inplacerad.stl
EXTENDED HYDRO-DFN		
SFR-Hydro-DFN-091210.cif	2009-12-23	SF091127_SFR_Preliminary_Hydro-DFN_parameterisation_2009-11-27_(QA).xls
DATA FOR CALIBRATION		
BH-koordinater.doc	2009-12-23	head_SFR.xlsx

A list of all input files above, including storage location, is for traceability documented in the SKB data base SKBdoc under id nr 1271531.